High Harmonic Generation in Strongly Correlated Systems

Markus Lysne

Thesis for the degree of Master of Science (MSc)

Department of Physics and Technology
University of Bergen

June 2018

Acknowledgements

I would like to thank my supervisors Professor Morten Førre and Dr. Hicham Agueny for excellent supervision throughout the thesis project. The rest of the Optics and Atomic Physics group, particularly my fellow master students Andreas, Ingunn and Morten, have provided a great atmosphere in the course of the last couple of years. I would also like to extend my gratitude towards Professor Emeritus Ladislav Kocbach for his valuable insights into the matters I have been studying and for providing me with the necessary tech-support!

Abstract

In recent years, the study of phenomena pertaining to non-linear properties of materials has seen a major upswing - especially in the context of High Harmonic Generation (HHG). In this thesis, an account of the current state of research in this area will be given. In addition, we seek to combine two seemingly disparate areas of research, both of which have been the subject of numerous years of intense research - namely those of HHG in solid state materials, and the optical response of strongly correlated quantum systems. To this end we will rely on solving the Fermi-Hubbard model coupled to an electromagnetic field under time propagation. With the aid of both numerical work and simple energy level analyses, we are able to explain most of the characteristics of our calculated spectra. High field strength will induce a Mott insulator to metal phase transition whose imprints will be established through time resolved high harmonic emission and doublon and spin correlation functions. The various HHG spectra, together with said correlation functions will be studied through an Exact diagonalization algorithm in conjunction with an Arnoldi-Lanczos time propagator. The parameter space considered is comprised of the electron-electron repulsion energy, U, and peak electric field strength. Additionally, the study is not restricted to half-filling, and results for doped materials will be presented. We find that the high U-induced energy gap in the Fermi-Hubbard model plays the same role as the valence-conduction bandgap in models like for instance the Semiconductor Bloch Equations when it comes to generating high harmonic radiation through multiphoton processes. The central part of this thesis aims at providing insight to and making further contributions to an article published in Nature Photonics in March 2018. [1]

Contents

Chapter 1

Introduction

In this introductory chapter, we will provide a brief introduction to the crux of the thesis, starting from an elementary level. At the end, an outline of the main contents of the thesis will be given.

1.1 High harmonic generation

Quantum theory dates back to Bohr's model of the hydrogen atom in the 1910s. [2] Although the model proved to be inadequate for more complex atoms, it still persists as a good introduction to the basic quantum physics of matter interacting with light. One can get a glimpse of some of the physics in a hydrogen atom by drawing a simple two level figure. When a photon is incident upon an atom, an electron can be excited to a state of higher energy, which is shown to the left in figure 1.1. Now, the already excited electron might subsequently emit radiation by another photon mediating the emission process. This process is referred to as *stimulated emission* and is shown to the right in figure 1.1. Now, in a scenario in which the energy of the incident photon is off-resonant with the energy gap, an electron might reach a higher energy state through a succession of *virtual states* as illustrated in figure 1.2. Once the high energy state is reached, the electron will ultimately relax to the ground state via either the stimulated emission process or through spontaneous emission. Either way, a photon of higher energy than the incident photons has been generated. The fact that we have one outgoing photon per five incident photons is merely a consequence of energy conservation. This process is called a *multiphoton process*. We emphasize the fact that the number emitted photons in a multiphoton process is always less than the number of photons required to reach $|1\rangle$.

It is natural to inquire why one might be interested in multiphoton processes, especially considering that the emitted photons are far and in between. The answer lies in the concept of *ultrafast measurements* [3] - an exciting avenue of research that has arisen due to the advent of new technology making it possible to study physics on the time scale of one billionth of a billionth of a second (10^{-18} s). [4] This endeaveour is motivated by the mere fact that many quantum processes in atoms happen on this time scale. Going back to the Bohr model of hydrogen, the time taken for an electron to orbit once around the atom is about 10^{-16} seconds.

Even though atoms are considered the archetypal quantum entities, interesting quantum behaviour is also present in solid state materials. Moreover, to explain some

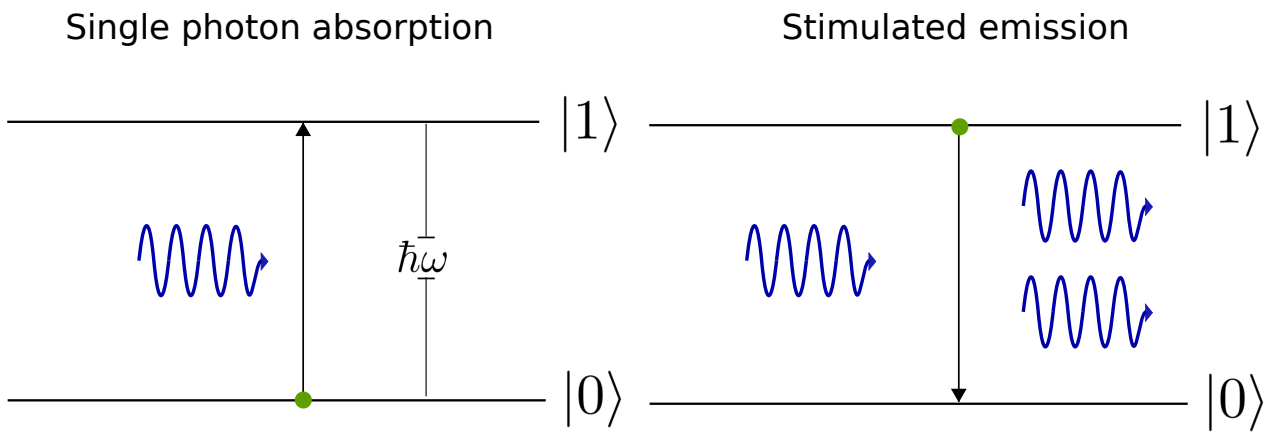

Figure 1.1: The leftmost figure shows the excitation of an electron from a state, $|0\rangle$, to an excited state, $|1\rangle$, through a resonant excitation. In the rightmost figure, the relaxation to the lowest lying energy state is displayed through the process dubbed stimulated emission.

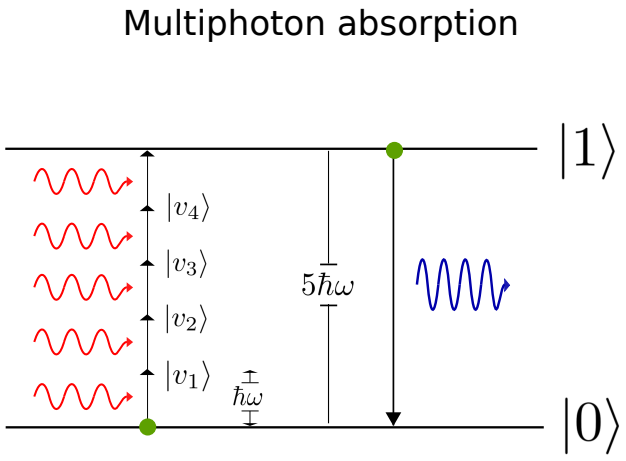

Figure 1.2: This figure illustrates the physical scenario when the electromagnetic field is comprised of photons that are off-resonant with the energy gap. A succession of virtual states are reached prior to reaching the state $|1\rangle$. After excitation has taken place, the electron might relax through spontaneous emission or stimulated emission.

properties of said systems, a quantum description is in fact necessary. The focus herein will be geared at multiphoton processes and subsequently the generation of high harmonics in such systems - photons generated in ways similar to the process displayed in figure 1.2.

High harmonic generation (HHG) can be concisely described as the generation of overtones arising from a material's response to a driving laser pulse. Depending on the type of system, the harmonics may arise from a multiphoton process, or may even arise when the photons in the laser pulse are resonant with the energy gap. [5] Hence, figure 1.2 provides a first glimpse at a HHG-process. A peculiar signature of HHG is the

appearance of only odd order harmonics, i.e. harmonics in which the angular frequency is an odd integer multiple of that of the driving field. [6]

1.2 HHG in atomic systems

Since HHG had its conception in atomic physics [7], and that subsequent research in large part has relied heavily upon the intuitions gained from those systems, it would be wrong not to at least give a brief disposition of its phenomenology. In the co called three-step model, HHG in atoms is explained by the following steps:

1. A bound electron is tunnel-ionized from the atom due to the nature of the tilted potential generated by the light-matter coupling. When the amount of tilt is such that the electron escapes even though it is classically forbidden, it is referred to as *tunneling*. [1] [8] See the leftmost panels in figure 1.3.

2. After ionization, the electron is accelerated in the continuum. See the middle panels in figure 1.3.

3. The electron recombines with the nucleus, and emits the energy corresponding to the difference between its energy as a bound electron, and that of the field accelerated "free" electron. This energy discrepancy is manifested in emitted photons having frequencies in integer multiples of the fundamental frequency. See the rightmost panels in figure 1.3.

The upper panels in figure 1.3 indicate the times of the laser pulse corresponding to each of the steps described above. The radiation yield as a function of frequency can often be said to reside in one of three regimes, shown in figure 1.4. The perturbative regime describes the multiphoton processes in figure 1.2. Experiments conducted on rare gases showed that the dramatic decrease in the perturbative regime was followed by a plateau region, i.e., a region of the spectrum in figure 1.4 in which the yield was nearly constant over several harmonic orders, until a sudden drop in the yield after a particular harmonic order following the plateau. That is, the HHG spectra can be said to display a *cut-off*, which is the rightmost region of figure 1.4. This means that there will be one or more frequencies after which the intensity of the harmonics is drastically reduced - see figure 1.4. In an attempt to make this cut-off behavior quantitative, an empirical relation between ionization energy, I_p, and cut-off energy, I_c, can be devised as follows

$$I_c = I_p + 3.17 \cdot U_p \tag{1.1}$$

where U_p the ponderomotive energy, the energy of the field-accelerated electron. We merely remark the following qualitative behavior

$$U_p \propto E_0^2 \propto I \tag{1.2}$$

where I is the intensity of the electromagnetic field, and E_0 the peak electric field strength.

[1] Furthermore, the ionization step does not necessitate the quantum mechanical concept of tunneling ionization. An ionization process which is allowed classically is referred to as above barrier ionization. [8]

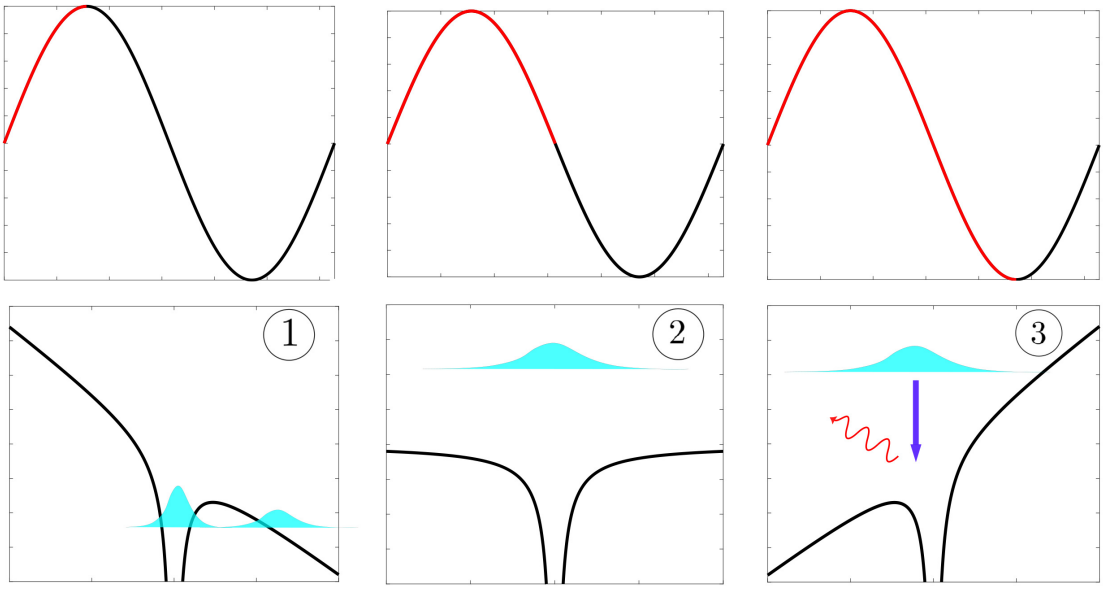

Figure 1.3: The upper panels show different times during half a cycle of a laser pulse. To each upper panel, the corresponding picture for the electron in a central potential is sketched beneath it. In process 1, it is seen that the effect of the laser pulse is to modify the potential to a tilted one, which expedites the tunneling process. Process 2 displays a dispersed wave packet with only a small influence of the central potential. In process 3, the electron recombines and emits (high harmonic) radiation.

HHG is a research area for which much work has been done in the context of atomic and molecular systems. [9] We have here presented one of the hallmark articles in the field of HHG in atomic systems - the proposal of a three-step model for HHG. [7] Even though a condensed matter system and an atomic system display differences with respect to electronic structure, in that there is no apt continuum description in the former, a three step model has been sought to explain HHG in solids. [10] The inherent difficulties in modeling HHG in condensed matter systems will be addressed in the following.

1.3 Condensed matter systems

The early success in priming and establishing the new field of HHG in condensed matter systems as a fertile research area can in large part be credited to Koch *et al.* [5] and Vampa *et al.* [11] From the initial rise in popularity, up until this day, a central purpose has been to ground the physics in an understanding paralleling that of the three-step model [7] in its simplicity.

To get a glimpse of the physics governing light-matter interactions in solids, it is instructive to begin by remarking the differences in the energies an electron can attain in such systems. The complexity is somewhat increased in relation to the two level system described above, in that a new dimension, or variable, is introduced; *crystal momentum*. Accepting the notion that an electron behaves as a wave in the crystal, and is in some systems even delocalized throughout the crystal, the crystal momentum can loosely be

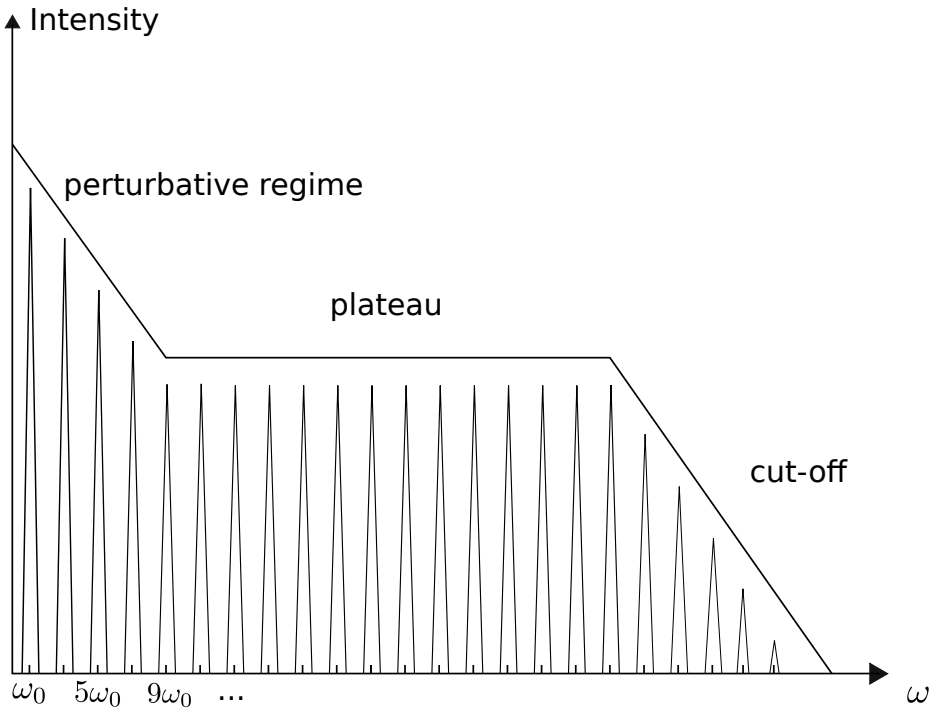

Figure 1.4: The yield of high harmonic radiation as a function of frequency of the emitted radiation is shown. When the yield is presented on a logarithmic scale, the spectrum often admits the demonstrated three-fold structure.

thought of as the momentum of the electron wave in the crystal. Earlier, we saw how the photon energy was absorbed in the system in the form of level excitations. However, by adding the crystal momentum dimension, not only does the system exhibit the level transitions in figures 1.1, 1.2, but it can do so at various crystal momenta. Additionally, light can accelerate the electron to higher momentum values within a band of energy levels - see figure 1.5. In figure 1.5, a few excitation routes are illustrated. The figure puts emphasis on the process of acceleration within the conduction band, although such an acceleration may also be undergone by an electron in the valence band. [2] The reason for the distinction crystal momentum, as opposed to momentum is the peculiar property of the momentum of an electron in a crystal. When attaining a momentum higher than a certain value, the wave function of the electron will effectively fold back to some smaller set of momenta. This reduced set of momenta is referred to as the first *Brillouin Zone*, or usually just the Brillouin Zone - the region of momentum space sketched in 1.5. Usually, the electron is obstructed on its path to high crystal momentum values - which is due to interactions with lattice vibrations, electron-electron scattering and more. [12] The phenomenon of an electron traversing the entire Brillouin Zone was originally proposed by Felix Bloch for electrons in static fields [13], but has recently been experimentally realized in AC-fields. [14] The particular example of time dependent external fields is referred to as *Dynamical Bloch Oscillations*. [15]

As already mentioned, atoms and solids exhibit different electronic structure. Moreover, seeing as light-emission is a mere reflection of the underlying electronic structure

[2]Usually, these types of problems are formulated in the language of electrons and holes, wherein physical quantities like the current are calculated in by essentially counting up vacant single particle states - holes. [12]

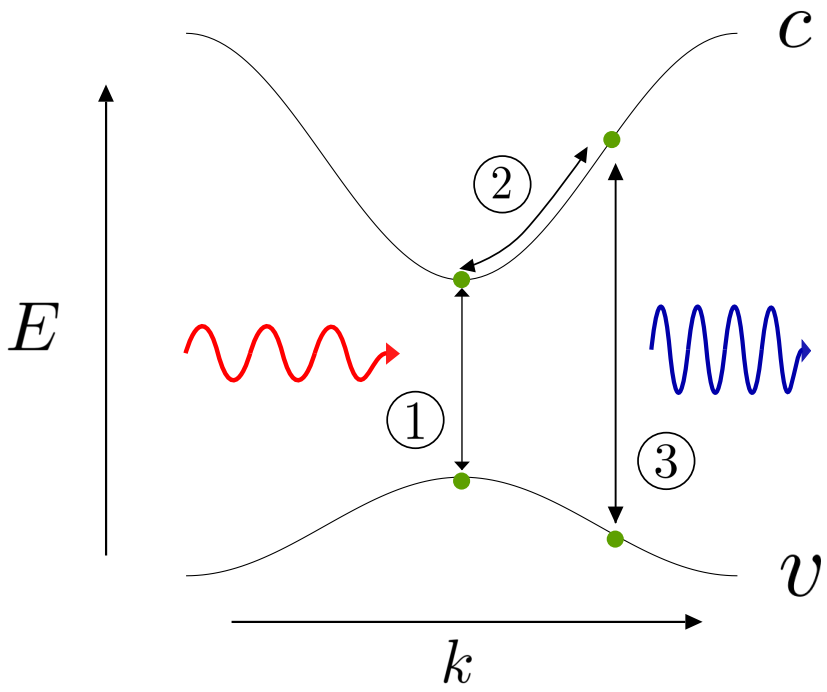

Figure 1.5: The motion of only one electron is sketched, although the valence band usually holds a full band of electrons. The initial transition marked 1 can be parallelled to the one in figure 1.1. Process 2 displays the additional degree of freedom along the axis of crystal momentum. Only a few out of many possible transitions are illustrated.

- the condensed matter counterpart displays richer dynamics. That is, since an additional degree of freedom is introduced - the crystal momentum - an electron can be excited via several pathways. In concrete terms, an interplay between intraband and interband [5] processes is the underlying processes governing HHG. Interband excitation refers to processes 1 and 3 in figure 1.5, while the intraband processes correspond to process 2. In solids, particularly in the system studied herein, the electron is often modeled as residing deep inside the crystal. There is thus no apt continuum description of HHG, unlike in atomic systems. This is a fact that complicates the matter of trajectory analyses in the style of HHG in atomic physics. Nevertheless, it should be noted that successful attempts have also been made for solid state materials in this regard. [16]

To give a rationale for the newly established field, one can argue along the lines of the importance of fundamental research pertaining to light-matter interactions. However, HHG can be more broadly characterized as belonging to the field of ultrafast physics. Said field provides promising outlooks on fast switching elements for next-generation electronics that can potentially be more energy efficient and faster than present-day transistors. In this regard, the prospect of ultrafast switching in a strongly correlated material has very recently been revived as a result of this. [1] Another appealing feature is the promise of elevating todays standards of table top sources of high frequency laser pulses. [17]

Experimentally, ultrafast processes can to date be monitored on sub-femtosecond time scales. An example is the time frequency resolution of high harmonic radiation. [1] Thus, many aspects of ultrafast imaging are within reach experimentally. On the

theoretical side, even single active electron theories, DFT-based studies [18], and most notably the regime of light-matter interaction in strongly correlated systems, lack the computational ease which at this point can be attributed to its atomic physics counterpart.

With the prospect of imaging in mind, research has recently been directed towards studying the ultrafast behavior of strongly correlated materials. A concept exclusive to the regime of strongly correlated electron systems is the concept of *photoinduced phase transitions*. [19] [20] The process is quantum mechanical in its origin. A correlation function, meaning some function which we can track throughout the phase transition, contains the signature of a transition from one phase to another. At this point, suffice it to say that their abrupt change are indicators of a phase transition taking place. Although seemingly unrelated to the concept of HHG, this concept unites with ultrafast physics due to the time scale associated with the phase transition and the prospect of monitoring the process with sub-cycle resolution with respect to an exciting laser pulse. [1]

The study of strongly correlated electron systems on pico- and femto-second time scales is an avenue for which many recent experiments have been performed. [19] [20] In order to not only excite the system in an apt way for femtosecond dynamics, but also resolve the sub cycle processes in time, novel pump probe techniques are prerequisites. The insulator to metal transition is a phase transition in a material in which characteristic fluctuations in spin correlation and doublon-hole correlation functions reach a metastable state. [1]

A convenient tool of analysis in these systems is provided through the so called Schwinger limit, defined by a threshold electric field strength, E_{th}. It is given by

$$E_{th} = \frac{\Delta}{2e\xi} \tag{1.3}$$

where Δ is the optical gap, e is the unit charge and ξ the correlation length - which is the typical spatial extent of a doublon-hole pair. [21] A doublon-hole pair is understood as a pair of an anion and a cation in the crystal. Specifically, the threshold field strength is the field strength required to initiate the described phase transition. E_{th} will depend on material parameters, as for example the energy of onsite interaction, U.

These systems also admit a useful characterization borrowed from atomic physics in strong fields - namely, the Keldysh adiabaticity parameter. [1] [8]

$$\gamma = \frac{\hbar\omega_0}{\xi E_0} \tag{1.4}$$

where ω_0 is the carrier frequency of the laser and E_0 its peak electric field strength. This formula holds true in AC fields. The range of values of the parameter quantitatively describes whether the system undergoes a multiphoton process or a tunneling process. It is chiefly in the regime $\gamma << 1$ that equation 1.3 holds. It is worthwhile remarking the following behavior of the threshold field strength considered in the article of R.E.F. Silva *et al.*

$$F_{th} \propto U \tag{1.5}$$

[1] This threshold behavior can also be viewed as a function of time, since the maximum field strength will increase during the pulse, until somewhere before the middle of the pulse the threshold is reached. The last equation is valid for relatively large electron repulsion, U. The latter statement and the relations above will be corroborated by

numerical simulations later on. For the present, we merely present the recent results of R.E.F. Silva et. al. [1] in figure 1.6. Figure 1.6 illustrates the behavior of correlation functions as a function of time, and when the field attains its threshold field strength for different system parameters. The pulse is plotted alongside the two figures.

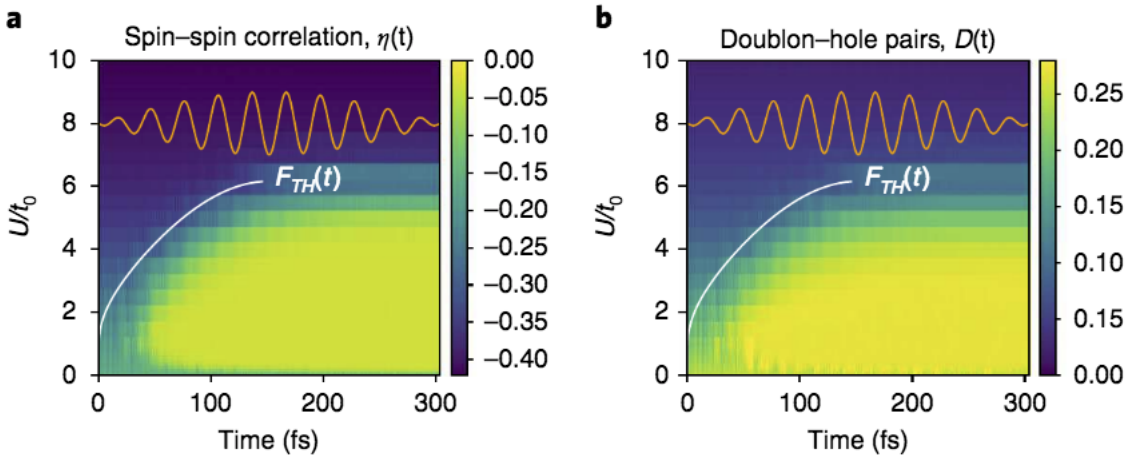

Figure 1.6: Two correlation functions are shown as a function of time for different instances of the electron-electron repulsion, U. Roughly speaking, the left panel displays the degree to which the spins are aligned antiparallel over time, and the right panel shows the number of doubly occupied sites, normalized over the system size, as a function of time. Courtesy of Nature photonics. [1]

Given the basic premises of HHG, it is not surprising that it bears promise in the context of imaging. The few aspects of HHG outlined here only give the merest indication as to the current state of research on the topic. Notable recent achievements include an all optical reconstruction of the band structure in ZnO and the investigation of multi band quantum interference effects. [22] [23] The latter has been used to investigate suppression of odd order harmonics in semiconductors. In addition, we are witnessing the the advent of the a field of study pertaining to strong electron correlation in conjunction with ultrafast physics. [1].

In light of recent progress, there is a lot indicating the technological role as well as the flourishing of formerly unexplored fundamental research areas. Particularly, the final words on the matter of HHG and strong electron correlation has not been said, and it is the authour's ambition to at least expand a little on the underlying microscopic theory of the newly published results. [1]

1.4 Outline of the thesis

The contents of the thesis can be summarized as follows:

- In chapter 2, a primer on time dependent quantum mechanics in condensed matter systems will be given. Most notably, the formalism of second quantization will be laid out. This is done in order to formulate the Hubbard model.
- In chapter 3, the Hubbard model is derived. Furthermore, basic theory regarding light matter coupling is applied to the Hubbard model.
- Although all numerical efforts are directed towards HHG-spectra in strongly correlated systems, we seek to theoretically describe our system analytically to the largest extent possible in chapter 4 until we resort to numerical methods.
- In chapter 5, we will provide a numerical framework capable of solving for the various observables in the Hubbard model under time propagation. In addition, we will elaborate on the practical aspects of the numerical methods, highlighting critical procedures along with algorithms and examples.
- The preceding chapters will comprise most of the machinery needed to describe the one dimensional Hubbard model with light matter coupling. However, some theoretical considerations are positioned among the results in chapter 6, which is done for the purpose a coherent disposition.

Throughout this thesis, atomic units will be employed unless stated otherwise. In these units, the values of $\hbar$, e, $\frac{1}{4\pi\epsilon_0}$ and m_e are all set to 1 [a.u.]. $\hbar$ is the reduced planck's constant, e is the elementary charge, ϵ_0 is the permittivity of free space and m_e is the electron mass. Quantities expressed in these units will be written with [a.u.] not to be confused with arbitrary units which we will denote by [arb.u].

Chapter 2

Fundamental concepts

In this chapter, we seek to build a foundation starting from basic theory both with regards to time independent methods in condensed matter physics and the theory of light matter coupling.

2.1 The time dependent Schrödinger equation

The quantum mechanical time evolution of a system of N electrons is given by the time dependent Schrödinger equation

$$i\frac{\partial}{\partial t}\Psi(\boldsymbol{r}_1, \boldsymbol{r}_2, ..., \boldsymbol{r}_N, t) = \hat{H}\Psi(\boldsymbol{r}_1, \boldsymbol{r}_2, ..., \boldsymbol{r}_N, t) \tag{2.1}$$

where $\Psi(\boldsymbol{r}_1, \boldsymbol{r}_2, ..., \boldsymbol{r}_N, t)$ is the wave function of the system and $\hat{H}$ its Hamiltonian. The wave function,$\Psi(\boldsymbol{r}_1, \boldsymbol{r}_2, ..., \boldsymbol{r}_N, t)$, also called the state of the system, is a vector in Hilbert space. It is of paramount importance as it contains all the information about the system. Specifically, in the Born interpretation, the quantity $|\Psi(\boldsymbol{r}_1, \boldsymbol{r}_2, ..., \boldsymbol{r}_N, t)|^2 d^3\boldsymbol{r}_1 d^3\boldsymbol{r}_2 ... d^3\boldsymbol{r}_N$ gives the probability of finding the electrons with coordinates $\boldsymbol{r}_1, \boldsymbol{r}_2, ..., \boldsymbol{r}_N$ in their respective volume elements $d^3\boldsymbol{r}_1, d^3\boldsymbol{r}_2, ..., d^3\boldsymbol{r}_N$ at time t. The Schrödinger equation can be formally integrated as follows

$$\Psi(\boldsymbol{r}_1, \boldsymbol{r}_2, ..., \boldsymbol{r}_N, t) = \hat{T}e^{-i\int_0^t \hat{H}(t')dt'}\Psi(\boldsymbol{r}_1, \boldsymbol{r}_2, ..., \boldsymbol{r}_N, 0) \tag{2.2}$$

where $\hat{T}$ is the time ordering operator, defined as

$$\hat{T}(\hat{A}(t)\hat{B}(t')) = \begin{cases} \hat{A}(t)\hat{B}(t') & \text{if t'<t} \\ -\hat{B}(t')\hat{A}(t) & \text{if t<t'} \end{cases} \tag{2.3}$$

whence the state of the system at any time t is obtained. Physical quantities like position, momentum etc. of a particle are related to *observables*. In quantum theory, observables correspond to operators over a Hilbert space. To each observable, $\hat{A}$, there is an associated notion of an expectation value. This is defined as

$$\left\langle \hat{A} \right\rangle (t) = \int_\Omega d\Omega \Psi^*(\boldsymbol{r}_1, \boldsymbol{r}_2, ..., \boldsymbol{r}_N, t)\hat{A}(t)\Psi(\boldsymbol{r}_1, \boldsymbol{r}_2, ..., \boldsymbol{r}_N, t) \tag{2.4}$$

where $d\Omega = d^3\boldsymbol{r}_1 d^3\boldsymbol{r}_2 ... d^3\boldsymbol{r}_N$. The expectation value does not describe the outcome of a single measurement of the property pertaining to observable A. Rather, it is the mean value obtained after doing a sufficient number of repeated measurements of the system prepared in state $\Psi(\boldsymbol{r}_1, \boldsymbol{r}_2, ..., \boldsymbol{r}_N, t)$. [24] Observables are required to be linear hermitian operators over a Hilbert space. This assures that their expectation values are real, whence $\left\langle \hat{A} \right\rangle (t)$ in equation 2.4 is real.

If the wave function is separable in space and time, i.e.,

$$\Psi(\boldsymbol{r}_1, \boldsymbol{r}_2, ..., \boldsymbol{r}_N, t) = \phi(\boldsymbol{r}_1, \boldsymbol{r}_2, ..., \boldsymbol{r}_N) f(t) \tag{2.5}$$

along with the fact that $\hat{H}$ is time independent, the following result follows from equation 2.1,

$$i \frac{1}{f(t)} \frac{\partial f(t)}{\partial t} = \frac{1}{\phi(\boldsymbol{r}_1, \boldsymbol{r}_2, ..., \boldsymbol{r}_N)} \hat{H} \phi(\boldsymbol{r}_1, \boldsymbol{r}_2, ..., \boldsymbol{r}_N) \tag{2.6}$$

Now, since the two sides of the equations depend on different variables, both sides of the equation are constant. Labeling this constant as E, it is readily seen that

$$\hat{H} \phi(\boldsymbol{r}_1, \boldsymbol{r}_2, ..., \boldsymbol{r}_N) = E \phi(\boldsymbol{r}_1, \boldsymbol{r}_2, ..., \boldsymbol{r}_N) \tag{2.7}$$

Moreover, the state's time dependence is governed by

$$i \frac{\partial f(t)}{\partial t} = E f(t) \tag{2.8}$$

which has solution

$$f(t) = f(t = t_0) \cdot e^{-iE(t - t_0)} \tag{2.9}$$

Clearly, for any Ψ satisfying $\hat{H}\Psi = E\Psi$,

$$\frac{d}{dt} \left\langle \hat{A} \right\rangle = \frac{d}{dt} \int_\Omega d\Omega \Psi(\boldsymbol{r}_1, \boldsymbol{r}_2, ..., \boldsymbol{r}_N, t)^* \hat{A} \Psi(\boldsymbol{r}_1, \boldsymbol{r}_2, ..., \boldsymbol{r}_N, t) = 0 \tag{2.10}$$

provided $\hat{A}$ is not a function of time. For a system in an eigenstate of a given observable, $\hat{A}$, the matter of calculating expectation values is much simpler. In that case, the problem amounts to the following eigenvalue equation

$$\hat{A} \psi_n = a_n \psi_n \tag{2.11}$$

Just like for equation 2.4, it follows that a_n is real provided $\hat{A}$ is hermitian, or self-adjoint. Moreover, for ψ_n and ψ_m satisfying 2.11 with $a_n \neq a_m$, ψ_n and ψ_m are orthogonal. That is,

$$\int_\Omega d\Omega \psi_n^* \psi_m = \delta_{n,m} \tag{2.12}$$

given that $\{\psi_n | \hat{A}\psi_n = o_n \psi_n\}$ are normalized. $\delta_{n,m}$ is the Kronecker delta, defined as

$$\delta_{m,n} = \begin{cases} 1 & \text{if m=n} \\ 0 & \text{if m} \neq n \end{cases} \tag{2.13}$$

To make the formulation more specific, for an interacting system of N particles, the Hamiltonian assumes the form

$$\begin{aligned}\hat{H} &= \sum_{i=1}^{N} \hat{h}_1(\boldsymbol{r}_i, t) + \frac{1}{2}\sum_{i,j=1}^{N} U_C(\boldsymbol{r}_i, \boldsymbol{r}_j, t) \\ &:= \hat{T} + U_C\end{aligned} \tag{2.14}$$

where $\hat{H}$ is partitioned into a sum of single particle operators, $h_1(\hat{\boldsymbol{r}}_i, t)$, and the mutual interaction between electrons in the system, $\frac{1}{2}\sum_{i,j} U_C(\boldsymbol{r}_i, \boldsymbol{r}_j, t)$ where $i \neq j$. The former may include the effect of an electrostatic potential and the coupling to an electromagnetic field and the latter is typically the electrostatic interaction between electrons. [1] It will be the purpose of the next section to lay out the essential theory regarding electromagnetism before the light matter coupling is developed.

2.2 Basic electromagnetism

[2] Maxwell's equations are given as

$$\begin{aligned}\boldsymbol{\nabla} \times \boldsymbol{B} &= \mu_0 \boldsymbol{J} + \mu_0 \epsilon_0 \frac{\partial \boldsymbol{E}}{\partial t} \\ \boldsymbol{\nabla} \times \boldsymbol{E} &= -\frac{\partial \boldsymbol{B}}{\partial t} \\ \boldsymbol{\nabla} \cdot \boldsymbol{B} &= 0 \\ \boldsymbol{\nabla} \cdot \boldsymbol{E} &= \frac{\rho}{\epsilon_0}\end{aligned} \tag{2.15}$$

where $\boldsymbol{J}[\frac{\mathrm{A}}{\mathrm{m}^2}]$ is the electric current density, $\boldsymbol{E}[\frac{\mathrm{V}}{\mathrm{m}}]$ the electric field, $\boldsymbol{B}[\frac{\mathrm{Wb}}{\mathrm{m}^2}]$ is the magnetic flux density, $\rho[\frac{\mathrm{C}}{\mathrm{m}^3}]$ is the charge density. μ_0 and ϵ_0 are the permeability and permittivity of free space, respectively. [25] In the following, we will resort to a useful restatement of equations 2.15 To this end, define the electromagnetic vector potential as

$$\boldsymbol{B} = \boldsymbol{\nabla} \times \boldsymbol{A} \tag{2.16}$$

which is in agreement with the third of Maxwell's equations 2.15 since the divergence of the curl of any smooth vector potential is zero. [26] $\boldsymbol{A}$'s relation to the electric field is

$$\begin{aligned}\boldsymbol{\nabla} \times \boldsymbol{E} &= -\frac{\partial}{\partial t}(\boldsymbol{\nabla} \times \boldsymbol{A}) \\ \boldsymbol{\nabla} \times (\boldsymbol{E} + \frac{\partial}{\partial t}\boldsymbol{A}) &= 0\end{aligned} \tag{2.17}$$

Now, since $\boldsymbol{\nabla} \times \boldsymbol{\nabla}\Phi = 0$ for a smooth scalar field, Φ, we may write

$$\boldsymbol{E} + \frac{\partial}{\partial t}\boldsymbol{A} = -\boldsymbol{\nabla} \cdot \Phi \tag{2.18}$$

[1] Although the single particle term most often includes $\hat{\boldsymbol{p}}_i$, we do not write it as an argument to equation 2.14

[2] This section is in SI units

whence

$$\boldsymbol{E} = -\frac{\partial}{\partial t}\boldsymbol{A} - \boldsymbol{\nabla}\cdot\Phi \tag{2.19}$$

Upon substitution into Maxwell's equations 2.15, the following couple of equations arise

$$\begin{aligned} \boldsymbol{\nabla}^2\Phi + \frac{\partial}{\partial t}(\boldsymbol{\nabla}\cdot\boldsymbol{A}) &= \frac{1}{\epsilon_0}\rho \\ \boldsymbol{\nabla}^2\boldsymbol{A} - \mu_0\epsilon_0\frac{\partial^2\boldsymbol{A}}{\partial t^2} - \boldsymbol{\nabla}\left(\boldsymbol{\nabla}\boldsymbol{A} + \mu_0\epsilon_0\frac{\partial\Phi}{\partial t}\right) &= -\mu_0\boldsymbol{J} \end{aligned} \tag{2.20}$$

By the established relation between electric and magnetic fields and the scalar and vector potentials, one can gain access to both electric and magnetic fields by solving the coupled equations 2.20. Furthermore, it is evident that the these equations exhibit a freedom in the sense that two different pairs $(\boldsymbol{A}, \Phi)$ and $(\boldsymbol{A}', \Phi')$ can give rise to the same physical fields. This freedom is called *gauge invariance*.

2.3 Light matter coupling

In classical mechanics, the motion of an electron in an electromagnetic field is governed by the Lorentz force

$$\boldsymbol{F} = \boldsymbol{v}\times\boldsymbol{B} + \boldsymbol{E} \tag{2.21}$$

where $\boldsymbol{v}$ is the electrons velocity at time t. In order to extend the Hamiltonian in equation 2.14 to that of a system of electrons interacting with an electromagnetic field, note that the single particle Hamiltonian can in the time independent case be cast in the form

$$\hat{H} = \sum_{i=1}^{N}\frac{\hat{\boldsymbol{p}}_i}{2} + V_I(\boldsymbol{r}_i) \tag{2.22}$$

where $\hat{p}_i$ is the momentum operator for electron i and $V_I(\boldsymbol{r}_i)$ is the electrostatic potential experienced by electron i. The effect of introducing the electromagnetic field amounts to the following substitution

$$\hat{\boldsymbol{p}} \longrightarrow \hat{\boldsymbol{p}} + \hat{\boldsymbol{A}}(\boldsymbol{r}, t) \tag{2.23}$$

This is made evident by the fact that the Hamiltonian in classical field theory for an electron in an electromagnetic field is given by [27]

$$H(\boldsymbol{r}, t) = \frac{1}{2}(\boldsymbol{p} + \boldsymbol{A}(\boldsymbol{r}, t))^2 - \Phi(\boldsymbol{r}, t) \tag{2.24}$$

By applying Hamilton's equations [28] to equation 2.24, equation 2.21 is obtained. The substitution 2.23 is referred to as *minimal coupling*. By applying the canonical quantization step [24], the single particle Hamiltonian in equation 2.22 is expressed on the following form

$$\hat{H} = \sum_{i=1}^{N}\frac{(\hat{\boldsymbol{p}}_i + \hat{\boldsymbol{A}}(\boldsymbol{r}, t))^2}{2} + V_I(\boldsymbol{r}_i) \tag{2.25}$$

where we have employed the gauge $\Phi(\boldsymbol{r}, t) = 0$. [29] An important approximation can be made in the above expression, namely the semiclassical approximation. This amounts to replacing $\hat{\boldsymbol{A}}$ with the classical field, $\boldsymbol{A}(\boldsymbol{r}, t)$. For a laser with sufficiently high photon number, the classical nature of light is prominent, and the quantum description becomes a cumbersome, and in fact redundant one for our purposes. [3] In the subsequent chapters, all efforts will be geared towards incorporating equation 2.25 into the Hubbard model. However, to achieve this with the necessary level of rigor, we first specialize our generical Hamiltonian in equation 2.14 to the case electrons on a one dimensional crystal lattice.

2.4 Electrons in a crystal lattice

[4] For an electron in a one-dimensional crystal lattice, the Hamiltonian can be written as

$$\hat{h}_1(r) = \frac{\hat{p}^2}{2} + \sum_{i=1}^{L} V_I(r - R_i) \tag{2.26}$$

where r is the coordinate of the electron, L is the number of atoms/sites in the lattice and R_i denotes the positions of the atoms/sites in the crystal lattice. This Hamiltonian assumes an electron that is not interacting with the other electrons present in the solid. The nearest neighboor atoms are separated by the lattice constant, a. As a central assumption, the potential is a periodic function in the lattice parameter, $V(r) = V(r + na)$ for arbitrary $n \in Z$. In addition, the periodicity of the charge density, $\rho(r)$, at different sites implies that the wavefunctions for an electron residing on different sites are separated by a complex phase,

$$e^{ikR_n}\psi_\lambda(k, r) = \psi_\lambda(k, r + R_n) \tag{2.27}$$

where k is some quantity yet to be determined and λ the band index. Upon writing

$$\psi_\lambda(k, r) = \frac{e^{ikr}}{\sqrt{L}} u_k(r) \tag{2.28}$$

it follows from equation 2.27 that

$$u_k(r) = u_k(r + a) \tag{2.29}$$

Equation 2.28 together with 2.29 is referred to as as *Bloch's theorem*. The Bloch states defined by equation 2.28 can be interpreted as plane waves modulated by a function carrying the periodicity of the lattice. An alternative derivation can be found in [12] or other introductory textbooks on condensed matter physics. In order to model the crystal as a finite system while circumventing the difficulty of surface effects, periodic boundary conditions are employed. This entails demanding that $\psi(r + La) = \psi(r)$ for

[3] However, it is important to emphasize that the process of spontaneous emission is not captured in the semiclassical approximation, and is only adequately treated in the framework of quantum field theory.

[4] From here on out, we lose the vector notation since all systems studied are one dimensional.

some integer L. From this consideration, k can be shown to take the following L discrete values

$$k = -\frac{\pi}{a}, -\frac{\pi}{a} + \frac{\pi}{La}, ..., 0, ..., \frac{\pi}{a} - \frac{\pi}{La} \tag{2.30}$$

Furthermore, the states in equation 2.28 exhibit orthogonality and completeness

$$\int_L \psi_\lambda^*(k, r)\psi_\xi(k', r) = \delta_{\lambda,\xi}\delta_{k,k'} \tag{2.31}$$

where the integral is taken over the length of the one dimensional crystal, La, which will be done throughout this section. Equation 2.31 holds true since $\{\psi_\lambda(k, r)\}$ are eigenstates of the crystal Hamiltonian 2.26. By the completeness property, any eigenstate of the Hamiltonian in equation 2.26 can be written as a linear combination of these eigenstates

$$\Psi(r) = \sum_{k,\lambda} c_{k,\lambda}\psi_\lambda(k, r) \tag{2.32}$$

where $c_{k,\lambda}$ are complex coefficients. At present, it is of interest to look for stationary states of the system. To this end, consider the Schrödinger equation for an electron located at a single atom in the crystal lattice

$$\hat{h}_{1,i}(r)\phi_\lambda(r - R_i) = \epsilon_\lambda\phi_\lambda(r - R_i) \tag{2.33}$$

where

$$\hat{h}_{1,i}(r) = \frac{\hat{p}^2}{2} + V_I(r - R_i) \tag{2.34}$$

is the Hamiltonian of an electron located at atom i. $\phi_\lambda(r - R_i)$ can be thought of as atomic wave functions, for which we may attribute variable spatial extent. Usually, the starting point of band structure calculations will be to limit the extent of $\phi_\lambda(r - R_i)$ to one atom. The following ansatz wave function satisfies Bloch's theorem

$$\psi_\lambda(k, r) = \sum_{n=1}^{L} \frac{e^{ikR_n}}{\sqrt{L}}\phi_\lambda(r - R_n) \tag{2.35}$$

as an eigenstate of the Hamiltonian in equation 2.26. The energy expectation value is calculated as

$$\epsilon_\lambda(k) = \int dr\psi_\lambda^*(k, r)\hat{h}_1(r)\psi_\lambda(k, r) \tag{2.36}$$

This is justified since

$$\begin{aligned} &\int dr\psi_\lambda^*(k, r)\psi_\lambda(k, r) \\ &= \frac{1}{L}\sum_{n=1}^{L}\sum_{m=1}^{L} e^{ik(R_n - R_m)} \int dr\phi_\lambda^*(r - R_m)\phi_\lambda(r - R_n) \end{aligned} \tag{2.37}$$

which along with the approximation

$$\int dr\phi_\lambda^*(r - R_m)\phi_\lambda(r - R_n) \approx \delta_{n,m} \tag{2.38}$$

gives

$$\int dr\psi_\lambda^*(k,r)\psi_\lambda(k,r) \approx 1 \tag{2.39}$$

Now, to get an expression for $\epsilon_\lambda(k)$, we introduce the approximation

$$\epsilon_\lambda \approx \tilde{\epsilon}_\lambda + \alpha_\lambda(k) \tag{2.40}$$

where

$$\begin{aligned}\tilde{\epsilon}_\lambda =& \frac{1}{L}\sum_{n=1}^{L}\sum_{m=1}^{L} e^{ik(R_m-R_n)} \int dr\phi_\lambda^*(r-R_n)\big(\frac{\hat{p}^2}{2m} + V_I(r-R_m)\big)\phi_\lambda(r-R_m) \\ &+ \frac{1}{L}\sum_{n=1}^{L}\int dr\phi_\lambda^*(r-R_n)\sum_{l\neq n} V_I(r-R_l)\phi_\lambda(r-R_n)\end{aligned} \tag{2.41}$$

and

$$\begin{aligned}\alpha_\lambda(k) =& \frac{1}{L}\sum_{n=1}^{L} e^{ik(R_{n+1}-R_n)} \int dr\phi_\lambda^*(r-R_n)\sum_{l=1}^{L} V_I(r-R_l)\phi_\lambda(r-R_{n+1}) \\ &+ \frac{1}{L}\sum_{n=1}^{L} e^{-ik(R_{n+1}-R_n)} \int dr\phi_\lambda^*(r-R_{n+1})\sum_{l=1}^{L} V_I(r-R_l)\phi_\lambda(r-R_n) \\ =& e^{ika}\frac{1}{L}\sum_{n=1}^{L}\int dr\phi_\lambda^*(r-R_n)\sum_{l=1}^{L} V_I(r-R_l)\phi_\lambda(r-R_{n+1}) \\ &+ e^{-ika}\frac{1}{L}\sum_{n=1}\int dr\phi_\lambda^*(r-R_{n+1})\sum_{l=1}^{L} V_I(r-R_l)\phi_\lambda(r-R_n)\end{aligned} \tag{2.42}$$

Now, $\tilde{\epsilon}_\lambda$ is the renormalized atomic energy and $\alpha_\lambda(k)$ the overlap integral representing the terms that involve nearest neighbor interactions. [12] If we define the overlap integrals as follows

$$t_{0,\lambda} = -\frac{1}{L}\sum_{n=1}\int dr\phi_\lambda^*(r-R_{n+1})\sum_{l=1}^{L} V_I(r-R_l)\phi_\lambda(r-R_n) \tag{2.43}$$

we may write equation 2.40 as

$$\epsilon_\lambda(k) \approx \tilde{\epsilon}_\lambda - 2t_{0,\lambda}\cos(ka) \tag{2.44}$$

The approximation scheme referred employed above is to as the *tight binding approximation*. [30] [12] Figure 2.1 depicts the dispersion given in equation 2.44 where $2t_0 = 1$, and the renormalized atomic energy, $\tilde{\epsilon}_\lambda = 0$.

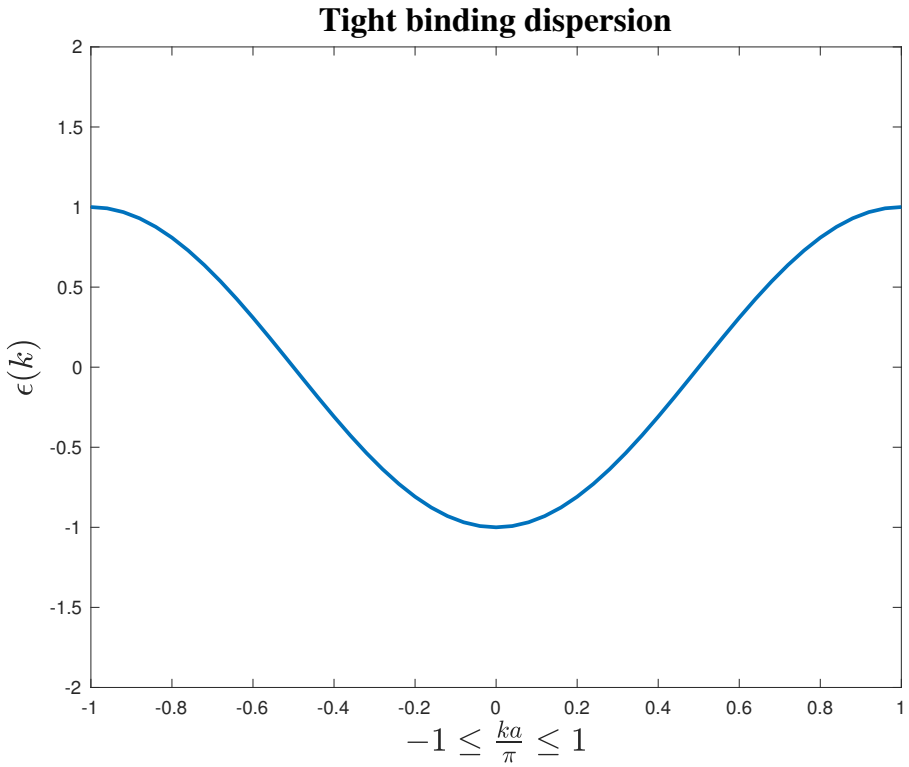

Figure 2.1: The tight binding dispersion with $2t_0 = 1$, and the renormalized atomic energy, $\tilde{\epsilon} = 0$.

2.5 Second quantization

The purpose of the present chapter is to introduce a formalism that is particularly convenient for many-particle systems. The formalism is referred to as second quantization whereas the previous formulation exemplified through equations 2.14 and 2.25 is dubbed first quantization. Second quantization has a great advantage over first quantization in the ease with which observables and correlation functions can be evaluated. [31] Prior to utilizing the full power of this method, it is instructive to get acquainted with the formalism as it applies to the single particle case. The generic Hamiltonian in equation 2.14 is solved for the instance of one particle, i.e., we solve

$$\hat{h}_1 |\nu\rangle = E_\nu |\nu\rangle \tag{2.45}$$

to give a complete set of single particle eigenstates, $\{|\nu\rangle\}$. The time dependence of equation 2.14 is dropped, since it is not of importance for this section. Now, by using the completeness relation, $\hat{h}_1(r)$ in equation 2.14 can be written as

$$\hat{h}_1(r) = \sum_{\mu,\nu} \langle\mu| \hat{h}_1 |\nu\rangle |\mu\rangle \langle\nu| \tag{2.46}$$

where

$$\langle\mu| \hat{h}_1 |\nu\rangle = \int dr \psi^*_\mu(r) \hat{h}_1(r) \psi_\nu(r) \tag{2.47}$$

since $\langle r|\mu\rangle = \psi_\mu(r)$. Note that the mention of r is lost in $\hat{h}_1$ on the left hand side of equation 2.47, which is a feature of the bra-ket notation. From equation 2.46 the physical

interpretation is that the Hamiltonian acts as to annihilate an electron from the state $|\nu\rangle$ and place it in $|\mu\rangle$. In order to make this statement more mathematically apparent, we employ the mathematical trick of writing $\langle 0|0\rangle = 1$ where $|0\rangle$ is the vacuum ket, i.e., a quantum state with no particles. By writing

$$\hat{h}_1(r) = \sum_{\mu,\nu} \langle\mu|\, \hat{h}_1\, |\nu\rangle\, (|\mu\rangle\, \langle 0|)(|0\rangle\, \langle\nu|) \tag{2.48}$$

our language of annihilation and creation processes becomes more apt. These processes can be associated to operators, whence the equation admits the form

$$\hat{h}_1(r) = \sum_{\mu,\nu} \hat{h}_{1\mu,\nu} \hat{c}^\dagger_\mu \hat{c}_\nu \tag{2.49}$$

where $\hat{h}_{1\mu,\nu} := \langle\mu|\, \hat{h}_1\, |\nu\rangle$ and $\hat{c}^\dagger_\nu$ and $\hat{c}_\nu$ are creation and annihilation operators, respectively. Although it can be shown from some of the considerations to come, it is merely stated here that the creation and annihilation operators obey the following anti commutation relations

$$\begin{aligned} \left\{\hat{c}_\alpha, \hat{c}^\dagger_\beta\right\} &= \delta_{\alpha,\beta} \\ \left\{\hat{c}^\dagger_\alpha, \hat{c}^\dagger_\beta\right\} &= 0 \\ \left\{\hat{c}_\alpha, \hat{c}_\beta\right\} &= 0 \end{aligned} \tag{2.50}$$

where

$$\left\{\hat{c}_\alpha, \hat{c}^\dagger_\beta\right\} = \hat{c}_\alpha \hat{c}^\dagger_\beta + \hat{c}^\dagger_\beta \hat{c}_\alpha \tag{2.51}$$

In order to showcase the utility of this method, we must first introduce an alltogether different way of representing the many body eigenstates of the Hamiltonian in equation 2.14. Such a state can be written as

$$\Psi(r_1, r_2, ..., r_N) = \sum_{\alpha_1,\alpha_2,...,\alpha_N} A_{\alpha_1,\alpha_2,...,\alpha_N} \psi(\alpha_1, \alpha_2, ..., \alpha_N) \tag{2.52}$$

where

$$\psi(\alpha_1, \alpha_2, ..., \alpha_N) = \frac{1}{\sqrt{N!}} \begin{vmatrix} \phi_{\alpha_1}(r_1) & \phi_{\alpha_2}(r_1) & \cdots & \phi_{\alpha_N}(r_1) \\ \phi_{\alpha_1}(r_2) & \phi_{\alpha_2}(r_2) & \cdots & \phi_{\alpha_N}(r_2) \\ \vdots & \vdots & \ddots & \vdots \\ \phi_{\alpha_1}(r_N) & \phi_{\alpha_2}(r_N) & \cdots & \phi_{\alpha_N}(r_N) \end{vmatrix} \tag{2.53}$$

is a Slater determinant and α_i denote single particle orbitals where we include the spin quantum number. Furthermore, all single particle orbitals are assumed to be orthogonal, i.e.,

$$\int dr \phi^*_\alpha(r) \phi_\beta(r) = \delta_{\alpha,\beta} \tag{2.54}$$

The Slater determinant ensures the correct anti-symmetrization of the fermionic wave function. That is, $\alpha_i \leftrightarrow \alpha_j$ amounts to exchanging two columns in the determinant expression, resulting in the desired anti-symmetry of equation 2.52: $\Psi(r_1, r_2, ..., r_i, ..., r_j, ..., r_N) = -\Psi(r_1, r_2, ..., r_j, ..., r_i, ..., r_N)$. Although there is explicit

mention of the coordinates of each of the N electrons inside the determinant expression, it need only be indexed by the quantum numbers $\{\alpha_i\}$. Therefore, the same information as that of equation 2.53 can be surmised from the following representation

$$\left|n_{\alpha_1}, n_{\alpha_2}, n_{\alpha_3}, ...\right\rangle \tag{2.55}$$

where $n_{\alpha_i} = 1$ if an electron is present in orbital ϕ_{α_i} and $n_{\alpha_i} = 0$ otherwise. This representation comes without the redundancy of keeping track of the identities of each and every electron and it is referred to as the *occupation number representation*. As an example, a two particle Slater determinant

$$\psi(\alpha_1, \alpha_2) = \frac{1}{\sqrt{2!}} \begin{vmatrix} \phi_{\alpha_1}(r_1) & \phi_{\alpha_2}(r_1) \\ \phi_{\alpha_1}(r_2) & \phi_{\alpha_2}(r_2) \end{vmatrix} \tag{2.56}$$

corresponds to the occupation number representation

$$\left|n_{\alpha_1} = 1, n_{\alpha_2} = 1, n_{\alpha_3} = 0, ...\right\rangle \tag{2.57}$$

with all remaining occupation numbers set to zero. In a more compact notation, a many body state can be expressed as $|\{n_\alpha\}\rangle$ where $\{n_\alpha\}$ is the set of occupation numbers in equation 2.55. In the same manner as for the single particle case in equations 2.45-2.49, the single particle term in equation 2.14 can for complete sets $\{|\{n_\alpha\}\rangle\}$ and $\{\left|\{n_\beta\}\right\rangle\}$ of many particle states be written as

$$\hat{h}_1(r_i) = \sum_{\{n_\alpha\}\{n_\beta\}} |\{n_\alpha\}\rangle \langle\{n_\alpha\}| \hat{h}_1 \left|\{n_\beta\}\right\rangle \left\langle\{n_\beta\}\right| \tag{2.58}$$

where now we change the argument from r to r_i to hone in on the coordinate of one out of a total of N electrons. Furthermore,

$$\langle\{n_\alpha\}| \hat{h}_1 \left|\{n_\beta\}\right\rangle = \int dr_1 dr_2 ... dr_N \psi^*(\alpha_1, \alpha_2, ..., \alpha_N) \hat{h}_1(r_i) \psi(\alpha_1, \alpha_2, ..., \alpha_N) \tag{2.59}$$

From equation 2.53 is is seen that this integral is a sum of expressions of the form

$$\begin{aligned} &\int dr_1 \phi^*_{\alpha_a}(r_1) \phi_{\beta_b}(r_1) \int dr_2 \phi^*_{\alpha_c}(r_2) \phi_{\beta_d}(r_2) \dots \\ &\int dr_i \phi^*_{\alpha_i}(r_i) \hat{h}_1(r_i) \phi_{\beta_i}(r_i) ... \int dr_N \phi^*_{\alpha_e}(r_N) \phi_{\beta_f}(r_N) \\ &= \int dr_i \phi^*_{\alpha}(r_i) \hat{h}_1(r_i) \phi_{\beta}(r_i) \delta_{\alpha_a,\beta_b} \delta_{\alpha_c,\beta_d} \delta_{\alpha_e,\beta_f} \end{aligned} \tag{2.60}$$

where we have used equation 2.54. Clearly, this expression only allows for one pair of orbitals to differ in order for it to be non-zero. Since at most one orbital is different for non zero matrix elements, $\left\langle\{n_\mu\}\right| V |\{n_\nu\}\rangle$, we can write

$$\hat{h}_1(r_i) = \sum_{\alpha_i,\beta_i} h_{1\alpha_i,\beta_i} \hat{c}^\dagger_{\alpha_i} \hat{c}_{\beta_i} \tag{2.61}$$

Now, we made the above procedure simple by considering only one term in equation 2.14. The treatment above is easily extended to $\hat{h}_1 := \sum_{i=1}^{N} \hat{h}_1(r_i)$, with essentially the same result, i.e.,

$$\hat{T} = \sum_{\alpha,\beta} h_{1\alpha,\beta} \hat{c}_\alpha^\dagger \hat{c}_\beta \tag{2.62}$$

where we have relabeled the indices in order to emphasize that the whole first term in equation 2.14 is considered. However, note that equations 2.61 and 2.62 are equal, due to the fact that $\{\alpha_i, \beta_i\}$ and $\{\alpha, \beta\}$ run over the same orbitals. A similar line of reasoning leads to an expression for the two particle interaction in equation 2.14. It is readily seen that for the two particle term

$$U_C = \frac{1}{2} \sum_{i \neq j} U_C(|r_i - r_j|) \tag{2.63}$$

$\langle \{n_\mu\} | U_C | \{n_\nu\} \rangle$ will only give rise to matrix elements of the form

$$U_{C,\alpha,\beta,\gamma,\delta} = \int dr_i dr_j \phi_\alpha^*(r_i) \phi_\beta^*(r_j) U_C(|r_i - r_j|) \phi_\gamma(r_i) \phi_\delta(r_j) \tag{2.64}$$

Thus, this expression will only give something non-zero when at most *two* pairs of orbitals are different. The result is

$$U_C = \frac{1}{2} \sum_{\alpha,\beta,\gamma,\delta} U_{C,\alpha,\beta,\gamma,\delta} \hat{c}_\alpha^\dagger \hat{c}_\beta^\dagger \hat{c}_\gamma \hat{c}_\delta \tag{2.65}$$

For an application to the Hubbard model, transformations between bases is particularly important. By the completeness relation, a transformation between two complete sets of basis states $\{|\tilde{\psi}_\nu\rangle\}$ and $\{|\psi_\nu\rangle\}$ can be written as

$$|\tilde{\psi}_\nu\rangle = \sum_\mu \langle \tilde{\psi}_\nu | \psi_\mu \rangle^* |\psi_\mu\rangle \tag{2.66}$$

which can be thought of as an operator basis change

$$\hat{\tilde{c}}_\nu^\dagger = \sum_\mu \langle \tilde{\psi}_\nu | \psi_\mu \rangle^* \hat{c}_\mu^\dagger \tag{2.67}$$

The position space representation will be granted special attention, and is given as

$$|r\rangle = \sum_\mu \langle r | \psi_\mu \rangle^* |\psi_\mu\rangle = \sum_\mu \psi_\mu^*(r) |\psi_\mu\rangle \tag{2.68}$$

where $|r\rangle$ is the position space ket. The corresponding operator can be expressed as

$$\hat{\Psi}_\sigma^\dagger(r) = \sum_\nu \langle r | \psi_{\nu,\sigma} \rangle^* \hat{c}_{\nu,\sigma}^\dagger = \sum_\nu \psi_{\nu,\sigma}^*(r) \hat{c}_{\nu,\sigma}^\dagger \tag{2.69}$$

where the spin quantum number, σ, has been extracted from the generic quantum number μ in equation 2.66 and marks the first explicit mention of the spin quantum

number in this section. $\hat{\Psi}^{\dagger}_{\sigma}(r)$ is referred to as the field operator. From equation 2.50, the field operator can be shown to obey anti-commutation relations, i.e.,

$$\begin{aligned}\left\{\hat{\Psi}_{\sigma}(r), \hat{\Psi}^{\dagger}_{\rho}(r')\right\} &= \delta(r-r')\delta_{\sigma,\rho} \\ \left\{\hat{\Psi}_{\sigma}(r), \hat{\Psi}_{\rho}(r')\right\} &= 0 \\ \left\{\hat{\Psi}^{\dagger}_{\sigma}(r), \hat{\Psi}^{\dagger}_{\rho}(r')\right\} &= 0\end{aligned} \tag{2.70}$$

where $\delta(r-r')$ is the Dirac-Delta function. With the formalism developed above, the single particle terms in the first quantized Hamiltonian in 2.14 can be cast in second quantized form as follows

$$\begin{aligned}\hat{T} &= \sum_{i=1}^{N} \hat{h}_1(r_i) = \sum_{\sigma,\rho}\sum_{\mu,\nu} \hat{T}_{\mu,\nu,\sigma,\rho}\hat{c}^{\dagger}_{\mu,\sigma}\hat{c}_{\nu,\rho} \\ &= \sum_{\sigma,\rho}\sum_{\mu,\nu}\int dr \psi^{*}_{\mu,\sigma}(r)\hat{T}\psi_{\nu,\rho}(r)\hat{c}^{\dagger}_{\mu,\sigma}\hat{c}_{\nu,\rho} \\ &= \sum_{\sigma}\int dr\Big(\sum_{\mu}\psi^{*}_{\mu,\sigma}(r)\hat{c}^{\dagger}_{\mu,\sigma}\Big)\hat{T}\Big(\sum_{\nu}\psi_{\nu,\sigma}(r)\hat{c}_{\nu}\Big) \\ &= \sum_{\sigma}\int dr \hat{\Psi}^{\dagger}_{\sigma}(r)\hat{T}\hat{\Psi}_{\sigma}(r)\end{aligned} \tag{2.71}$$

where $\hat{T}_{r,\sigma,\rho} = \hat{T}_r\delta_{\sigma,\rho}$ is assumed in going from line 2 to 3. The two particle interaction term in equation 2.65 follows a similar derivation

$$\begin{aligned}U_C &= \frac{1}{2}\sum_{\alpha,\beta,\gamma,\delta} U_{C,\alpha,\beta,\gamma,\delta}\hat{c}^{\dagger}_{\alpha}\hat{c}^{\dagger}_{\beta}\hat{c}_{\gamma}\hat{c}_{\delta} \\ &= \frac{1}{2}\sum_{\sigma,\rho}\sum_{\mu,\mu',\nu,\nu'}\int dr dr' \psi^{*}_{\mu,\sigma}(r)\psi^{*}_{\mu',\rho}(r')U_C(|r-r'|)\psi_{\nu,\rho}(r')\psi_{\nu',\sigma}(r) \\ &\ldots \hat{c}^{\dagger}_{\mu,\sigma}\hat{c}^{\dagger}_{\mu',\rho}\hat{c}_{\nu,\rho}\hat{c}_{\nu',\sigma} \\ &= \frac{1}{2}\sum_{\sigma,\rho}\int dr dr' \hat{\Psi}^{\dagger}_{\sigma}(r)\hat{\Psi}^{\dagger}_{\rho}(r')U_C(|r-r'|)\hat{\Psi}_{\rho}(r')\hat{\Psi}_{\sigma}(r)\end{aligned} \tag{2.72}$$

In going from line 1 to 2, the spin quantum numbers have been extracted from the indices in line 1. Note, that we are in equation 2.67 not restricted to changes from momentum to position and vice versa, but sometimes between different position bases, for which the delocalized Bloch basis and the localized Wannier basis are bases which admit such an inter-dependence. For the upcoming chapter on the Hubbard model, the Hamiltonian constructed from equations 2.71 and 2.72

$$\begin{aligned}\hat{H} &= \sum_{\sigma}\int dr \hat{\Psi}^{\dagger}_{\sigma}(r)\hat{T}\hat{\Psi}^{\dagger}_{\sigma}(r) \\ &+ \frac{1}{2}\sum_{\sigma,\rho}\int dr dr' \hat{\Psi}^{\dagger}_{\sigma}(r)\hat{\Psi}^{\dagger}_{\rho}(r')U_C(|r-r'|)\hat{\Psi}_{\rho}(r')\hat{\Psi}_{\sigma}(r)\end{aligned} \tag{2.73}$$

will be the starting point.

Chapter 3

The Hubbard Model

Research efforts concerning HHG in solid state materials have up until now mainly been geared at single active electron systems. [32] [11] Simply put, all systems studied thus far have the advantage of having a description in terms of a single electron on top of a periodic potential. In other words, although a solid is comprised of many electrons, one can treat the effect of other electrons as a *mean field* - which means that the effect of the other electrons act on the electron in question in an average way.

Despite the complex electronic structure of the transition metal compounds, the Hubbard model uses a single band description. Moreover, long range interaction are neglected, motivated by the fact high degree of correlation favors localization of the electrons. [33] Even though a single band description is employed, the Hubbard model is able to explain the insulating behaviour of certain metal oxides that are predicted to be metals under regular band theory. [34] The ability to explain insulating behaviour is the mere consequence of explicit treatment of electron correlation effects. It is worth mentioning that a band picture of the Hubbard model can be devised [34], where the "bands" are referred to as Hubbard subbands [34], or in other parts of the literature as Hubbard bands. [1] [35] [36] They differ from regular band theory in ways that will be elaborated on in this chapter. However, they find an analogous description in terms of doubly occupied sites and vacancies - in the literature referred to as doublons and holons. [21]

3.1 Hamiltonian

Due to the translational symmetry of the potential, Bloch's theorem gives an analytical solution to the one particle wavefunction in a crystal lattice in terms of band index and crystal momentum, k. However, this solution will only apply to the single particle terms of the Hamiltonian, and attacking the problem of calculating the matrix elements of the electron-electron interaction can be more demanding. One can only hope that if evaluated in the basis of the one particle Hamiltonian, that the interaction-matrix elements are small, and that corrections can be tackled in perturbation theory. [37]

Now, the idea of of tackling the many-body problem in terms of a single particle eigenvalue problem will be applied. We generalize the Hamiltonian in equation 2.26 to

that of a system of N interacting electrons on a crystal lattice, and write

$$\hat{H} = \sum_{i=1}^{N} \frac{\hat{p}_i^2}{2} + \sum_{l=1}^{L}\sum_{i=1}^{N} V_I(r_i - R_l) + \frac{1}{2}\sum_{i\neq j} U_C(|r_i - r_j|) \tag{3.1}$$

To accommodate the many-particle nature of the system, we perform the following substitution in equation 3.1

$$V_I \longrightarrow V_I + V_A = V \tag{3.2}$$

where V_I is the electrostatic potential of an electron experienced only due to the ions (and not the other electrons), while V_A represents a mean effect of the other electrons. Thus, V can be thought of as an effective electrostatic potential. This change in the single particle operator is alleviated by a corresponding subtraction in the two-particle interaction term

$$\sum_{1\leq i<j\leq N} U_C(|r_i - r_j|) \longrightarrow \sum_{1\leq i<j\leq N} U_C(|r_i - r_j|) - \frac{1}{N-1}(V_A(r_i) + V_A(r_j)) = U \tag{3.3}$$

As a result, it is assumed that the single particle part has absorbed the effect of the electron-electron interaction term to as large a degree as possible. Physically, envisage an electron immersed in a system in which the electronic charge density due to the other electrons *screens* the attraction between the electrons and ions. For electron i, the charge density

$$|\Psi(r_1, r_2, ..., r_{i-1}, r_{i+1}, ..., r_N)|^2 \tag{3.4}$$

adds an auxiliary core potential, V_A to the problem. Upon substituting equation 3.2 into equation 3.1 and focusing on a single particle on the lattice, we may solve for the renormalized Bloch functions, $\tilde{\psi}_{k\sigma}(r)$. Explicitly, they are eigenstates of

$$\hat{h}_1(r) = \frac{\hat{p}^2}{2} + \sum_{i=1}^{L} V(r - R_i) \tag{3.5}$$

Thus, we obtain a suitable basis which can be used to express the matrix elements of the interaction term in equation 3.3. For the purposes in this thesis, it will be advantageous to transform the basis to a localized one. This transformation is realized through Wannier functions. [12] [29] They are defined as follows

$$w_\sigma(r - R_n) = \frac{1}{L}\sum_{k} \tilde{\psi}_{k\sigma}(r) e^{-ikR_n} \tag{3.6}$$

where L is the number of lattice sites, $\tilde{\psi}_{k\sigma}(r)$ is a Bloch function whose properties are defined in equations 2.27 and 2.28, only this time it is a solution to a the Hamiltonian in equation 3.5. From equation 2.31 it can be shown that

$$\int dr w_\sigma^*(r - R_i) w_\sigma(r - R_j) = \delta_{i,j} \tag{3.7}$$

To make contact with our general Hamiltonian, the field operator in equation 2.69 is expressed in terms of Wannier functions

$$\hat{\Psi}_\sigma^\dagger(r) = \sum_{i=1}^{L} w_\sigma^*(r - R_i)\hat{c}_{i,\sigma}^\dagger \tag{3.8}$$

For the single particle term in the generic Hamiltonian in equation 2.73, write

$$\begin{aligned}\hat{T} &= \sum_{\sigma} \int dr \Big(\sum_{i=1}^{L} w_{\sigma}^{*}(r - R_i)\hat{c}_{i,\sigma}^{\dagger} \Big) \hat{h}_1(r) \Big(\sum_{j=1}^{L} w_{\sigma}(r - R_j)\hat{c}_{j,\sigma} \Big) \\ &= \sum_{\sigma} \sum_{i,j=1}^{L} t_{ij} \hat{c}_{i,\sigma}^{\dagger} \hat{c}_{j,\sigma}\end{aligned} \tag{3.9}$$

where

$$t_{ij} = \int dr w_{\sigma}^{*}(r - R_i)\hat{h}_1(r) w_{\sigma}(r - R_j) \tag{3.10}$$

which is independent of σ. t_{ij} is usually referred to as the hopping matrix element. For the interaction term in equation 2.73,

$$\begin{aligned}U &= \frac{1}{2} \sum_{\sigma,\rho} \int dr dr' \hat{\Psi}_{\sigma}^{\dagger}(r) \hat{\Psi}_{\rho}^{\dagger}(r') U_C(|r - r'|) \hat{\Psi}_{\rho}(r') \hat{\Psi}_{\sigma}(r) \\ &= \frac{1}{2} \sum_{\sigma,\rho} \sum_{ijkl} U_{Cijkl} \hat{c}_{i,\sigma}^{\dagger} \hat{c}_{j,\rho}^{\dagger} \hat{c}_{k,\rho} \hat{c}_{l,\sigma}\end{aligned} \tag{3.11}$$

where

$$U_{C,ijkl} = \int dr dr' w_{\sigma}^{*}(r - R_i) w_{\rho}^{*}(r' - R_j) U_C(|r - r'|) w_{\rho}(r' - R_k) w_{\sigma}(r - R_l) \tag{3.12}$$

As explained in [33], the nearest neighboor interaction terms can be approximated as having energies of $\approx 6eV$, while the onsite integrals, i.e., $i = j = k = l$, dominate with approximately $20eV$ for 3d electrons in transition metals. Thus, a valid (but coarse) approximation is to only retain terms in the sum of equation 3.11 for which $i = j = k = l$. Explicitly,

$$U = \frac{1}{2} \sum_{\sigma,\overline{\sigma}} U_{C,iiii} \sum_{i=1}^{L} \hat{n}_{i,\sigma} \hat{n}_{i,\overline{\sigma}} = U \sum_{i=1}^{L} \hat{n}_{i,\uparrow} \hat{n}_{i,\downarrow} \tag{3.13}$$

where we defined $U_{C,iiii} = U$. With the approximation in equation 3.13 the Hamiltonian in equation 2.73 is cast in the Wannier basis as follows

$$\hat{H} = \sum_{\sigma} \sum_{ij} t_{ij} \hat{c}_{i,\sigma}^{\dagger} \hat{c}_{j,\sigma} + U \sum_{i=1}^{L} \hat{n}_{i,\uparrow} \hat{n}_{i,\downarrow} \tag{3.14}$$

In actual computations, tackling the kinetic term in equation 3.14 in full generality, i.e., including t_{ij} for $|i - j| > 1$ grossly complicates the problem. Concretely, they represent denser matrices in the basis which will be employed later. A well established approximation at this point is the tight binding approximation laid out in the section 2.4, in which only terms involving $t_{i,i\pm1}$ are retained. Translational symmetry ensures that $t_{i,i\pm1}$ is independent of i. Therefore, we define

$$\hat{T} = -t_0 \sum_{\sigma} \sum_{i=1}^{L} \hat{c}_{i,\sigma}^{\dagger} \hat{c}_{i+1,\sigma} + h.c. \tag{3.15}$$

where the operators obey periodic boundary conditions, i.e.,

$$\hat{c}_i = \hat{c}_{L+i} \tag{3.16}$$

Upon substituting the kinetic term in equation 3.14 with that from the tight binding approximation, equation 3.15, the Hubbard Hamiltonian is obtained

$$\hat{H} = -t_0 \sum_{\sigma} \sum_{j=1}^{L} \left(\hat{c}^{\dagger}_{j,\sigma} \hat{c}_{j+1,\sigma} + h.c \right) + U \sum_{j=1}^{L} \hat{n}_{j,\uparrow} \hat{n}_{j,\downarrow} \tag{3.17}$$

Equation 3.17 has the following physical interpretation. The Hubbard Hamiltonian describes a system of electrons moving through a discrete set of lattice positions, under the influence of the mutual interaction term involving U. The first term will be referred to as the hopping term - a particularly appropriate image in real space since the operators acts as to remove an electron from a site and place it in a neighboring site. The last term acts as to raise the systems energy whenever there are two electrons with opposite spin on one site. In the limit of $U << t$ we basically retain the single electron description in chapter 2 section 2.4. In the opposite limit, $U >> t$, the low energy states of the system tend to distribute the electrons with adjacent spins anti-parallel to each other. Such a state is called an anti-ferromagnetic state.

The Hubbard model aims at modeling the strongly correlated behavior of 3d electrons in transition metal oxides by s like orbitals, which is a shortcoming to the theory. Moreover, only a single band is included. To a good approximation, when the Fermi level lies inside of the conduction band, this picture is justified. An important remark regarding 3.17 and other lattice Hamiltonians is the neglect of any explicit mention of the site-energy, t_{ii}. This is merely a matter of defining an absolute energy scale and it can therefore be set equal to zero.

For the upcoming chapters, the end goal is the application of equation 3.17 to a system of 12 sites and 12 electrons in the presence of an electromagnetic field. However, before developing the theory further it is helpful to turn to an example in which only two electrons are placed on a lattice of L sites.

3.2 The contrast to band theory

The total wave function for two electrons on an L site lattice is given as

$$\Psi(\alpha_1, \alpha_2) = \phi(r_1, r_2)\Xi(\sigma_1, \sigma_2) \tag{3.18}$$

where α_1 and α_2 are generic quantum labels comprised of the spin part and position part of electrons with labels 1 and 2, respectively. r_1 and r_2 denote the coordinates of electrons with labels 1 and 2, respectively. $\phi(r_1, r_2)$ is the spatial part of $\Psi(\alpha_1, \alpha_2)$ and $\Xi(\sigma_1, \sigma_2)$ the spin part. σ_1 and σ_2 denote the spins of electrons with labels 1 and 2, respectively. Now, define $\phi(i, j)$ as the spatial wave function of a system in which the electron with position label r_1 is at lattice site i and and the other electron with position label r_2 is at lattice site j. Specifically, assign the first argument to electron "1" and the second argument to electron "2", i.e.,

$$\phi(\underbrace{\ i\ }_{r_1}, \underbrace{\ j\ }_{r_2}) \tag{3.19}$$

Furthermore, the spin part can be separated in terms of its eigenvalue of the total spin operator, $\hat{s}$, i.e., $s = 1$ and $s = 0$. The spin part is denoted $\Xi^s_m(\sigma_1, \sigma_2)$ where m is the spin magnetic quantum number. [24] For s=1, denote

$$\begin{aligned} \Xi^1_1(\sigma_1, \sigma_2) &= |\uparrow\uparrow\rangle \\ \Xi^1_0(\sigma_1, \sigma_2) &= \frac{1}{\sqrt{2}}(|\uparrow\downarrow\rangle + |\downarrow\uparrow\rangle) \\ \Xi^1_{-1}(\sigma_1, \sigma_2) &= |\downarrow\downarrow\rangle \end{aligned} \tag{3.20}$$

and for the singlet state, $s = 0$

$$\Xi^0_0(\sigma_1, \sigma_2) = \frac{1}{\sqrt{2}}(|\uparrow\downarrow\rangle - |\downarrow\uparrow\rangle) \tag{3.21}$$

It is thus evident that in the spin triplet case, $\phi(i, j)$ must be anti-symmetric and for the spin singlet case, symmetric in order for equation 3.18 to have the correct anti-symmetry. Now, one can hone in on the spatial part of equation 3.18, and look for a solution to the Hubbard model in equation 3.17. In the following we will do so in a manner similar to that done in John Hubbard's original paper. [33] For the present, it is not necessary to restrict ourselves to the tight binding approximation. We once again state the Hamiltonian in equation 3.14 as

$$\hat{H} = \sum_{\sigma} \sum_{ij}^{L} t_{ij} \hat{c}^{\dagger}_{i,\sigma} \hat{c}_{j,\sigma} + U \sum_{j=1}^{N} \hat{n}_{j,\uparrow} \hat{n}_{j,\downarrow} \tag{3.22}$$

Now, note that for a solution of

$$\hat{H}\phi(i, j) = E\phi(i, j) \tag{3.23}$$

it follows from equation 3.22 that this can be written as

$$\hat{H}\phi(i, j) = \sum_{l} t_{il}\phi(l, j) + \sum_{l} t_{jl}\phi(i, l) + U\delta_{ij}\phi(i, j) \tag{3.24}$$

since $\hat{H}$ in equation 3.17 only acts as to move electrons between sites, and not flip their spins. It is obvious from this equation that there will be no high energy contribution from the last term for spin triplet states, seeing as the spatial (anti-symmetric) part of the wave function vanishes, i.e., $\phi(i, i) = 0$. Thus, we need only be concerned with the spin singlet state in equation 3.21. The eigenvalue equation 3.24 becomes, explicitly

$$\sum_{l} t_{il}\phi(l, j) + \sum_{l} t_{jl}\phi(i, l) + U\delta_{ij}\phi(i, j) = E\phi(i, j) \tag{3.25}$$

Now, in order to compare the Hubbard model to a regular band picture, a transition to momentum space is necessary. A Fourier transformation of $\phi(i, j)$ may proceed as follows

$$\begin{aligned} \phi(i, j) &= L^{-1} \sum_{k} \sum_{p} e^{ikR_i} e^{ipR_j} \tilde{\phi}(k, p) \\ &= L^{-1} \sum_{K} \sum_{p} e^{iK(R_i + R_j)} e^{i\frac{1}{2}p(R_i - R_j)} \tilde{\phi}(p, K) \end{aligned} \tag{3.26}$$

where a change of variables was performed in the last equation. Upon insertion of equation 3.26 into equation 3.25 along with the Fourier transform of the hopping parameter, t_{ij}, [29]

$$\epsilon(k) = L^{-1} \sum_{ij} t_{ij} e^{ik(R_i - R_j)} \tag{3.27}$$

we get

$$E\tilde{\phi}(p,K) = (\epsilon(K + \frac{1}{2}p) + \epsilon(K - \frac{1}{2}p))\tilde{\phi}(p,K) + \frac{U}{L}\sum_k \tilde{\phi}(k,K) \tag{3.28}$$

Upon rearranging, we obtain

$$\tilde{\phi}(p,K) = \frac{UL^{-1}\sum_k \tilde{\phi}(k,K)}{E - \epsilon(K + \frac{1}{2}p) - \epsilon(K - \frac{1}{2}p)} \tag{3.29}$$

from which the following result is seen by summing over p on both sides

$$\frac{U}{L}\sum_p \frac{1}{E - \epsilon(K + \frac{1}{2}p) - \epsilon(K - \frac{1}{2}p)} = 1 \tag{3.30}$$

A subtle thing to note at this point is the fact that between the L number of singularities of equation 3.30, there are L-1 solutions for E. They are in fact nested between the singular points, but all lie somewhere on the band $\epsilon(k)$ for some k. [33] Now, define the average band energy as

$$T_0 = L^{-1}\sum_k \epsilon(k) \tag{3.31}$$

and insert $E = 2T_0 + U$ into equation 3.30. If U is so large as to justify the following approximation

$$U + 2T_0 - \epsilon(K + \frac{1}{2}p) - \epsilon(K - \frac{1}{2}p) \approx U \tag{3.32}$$

then $E = U + 2T_0$ represents the L-th solution of equation 3.30. In conclusion, the case study of placing two electrons on a L-site lattice resulted in L possible ways of placing a first electron in the band, $\epsilon(k)$ (corresponding to the L values of K), and L-1 ways to configure the remaining electron such that the resulting state became a low energy eigenstate. For each value of K, however, there is one high energy configuration.

One can now surmise that for n electrons placed among L lattice sites, there are now (L-n) possible ways of placing an additional electron without introducing an additional energy contribution of order U to the system. At the same time, there are n possible ways of making such a high energy state by suitably placing the last electron on an already occupied site. The L-n number of low energy placements of the last electron amounts to different ways of placing the remaining electron in the lower band sketched in figure 3.1, while the n possible high energy configurations correspond to occupation of the upper band. These bands are referred to as subbands, since they differ from regular bands in some regards. An important remark about the emerging band picture is the fact that population in the upper subband in fact necessitates some population in the lower subband. [34]

Hubbard did in fact show that the dispersions for (pseudo-) particles of spin σ residing in one of the two subbands are described by the roots of

$$(E - \epsilon(k))(E - T_0 - U) + n_{\overline{\sigma}}U(T_0 - \epsilon(k)) = 0 \tag{3.33}$$

where $n_{\overline{\sigma}}$ is the average number of electrons with spin $\overline{\sigma}$ per site. The proof of this, which involves the method of Green's functions, is provided in appendix B. The spin σ electron dispersion for the two bands at half filling, $n_\sigma = n_{\overline{\sigma}} = 1/2$, with $U = 5t_0$ from equation 3.22 is shown in figure 3.1. Although the complexity of the general many particle problem is too vast to be tackled by the procedure above, the filling of the upper subband in figure 3.1 can be thought of as arising from single electrons being placed on top of occupied sites in the lattice. The formalism of subbands benefits from the

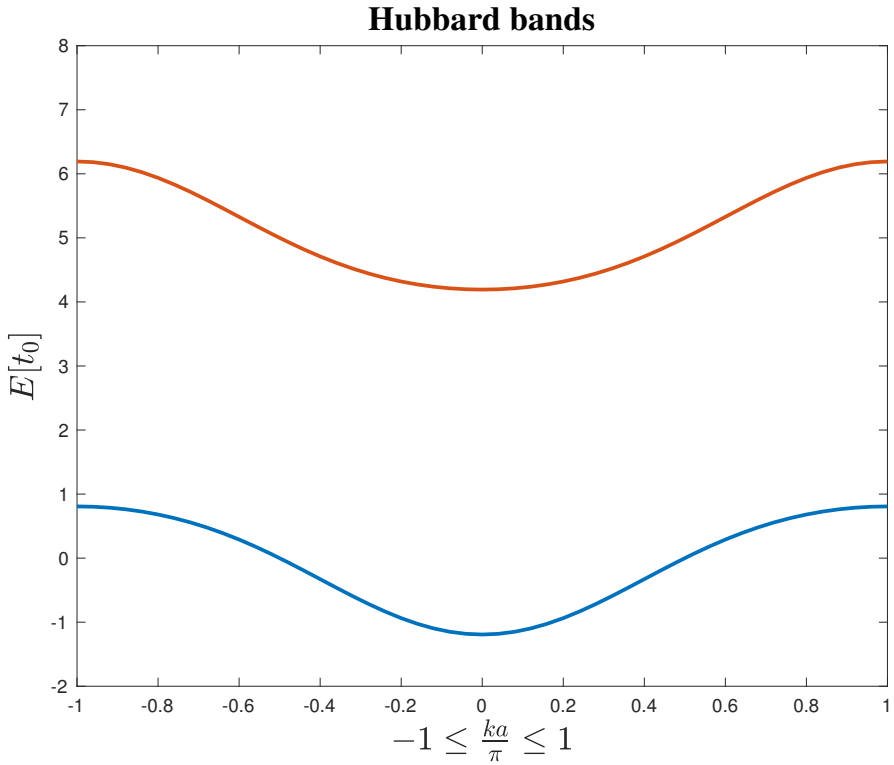

Figure 3.1: The two Hubbard subbands arising from a system at half filling ($n = n_\sigma + n_{\overline{\sigma}} = 1$) and $U = 5t_0$ in equation 3.22.

vantage point of discussing the light matter processes in strongly correlated systems in a manner reminiscent to that of two-band semiconductor models. [5] In semiconductor, photoinduced interband transitions happen in the manner illustrated in figure 1.5, and do not necessitate any two particle effects. However, in the strongly correlated material, a viable interpretation of the bound state with energy $E = 2T_0 + U$ is the interpretation as the sum of an electron with energy T_0 and another with energy $T_0 + U$. [34] Thus, in the spirit of describing the physics from the viewpoint of single electrons, one can imagine an excitation to the upper subband as arising from an electron being excited from an initial energy of T_0 to an energy $T_0 + U$.

With the interpretation following equation 3.17 in mind, it is the hopping term which is responsible for promoting electrons to the high energy configurations. As a result, the hopping term can be viewed as the mediator of transitions between the Hubbard bands. It will be the scope of the following chapter to elaborate on how the incorporation of light matter coupling will alter this hopping term.

3.3 Light matter coupling

According to equation 2.25, the single particle part of the Hamiltonian in equation 3.5 can be written

$$\hat{h}_1(r,t) = \frac{1}{2}(\hat{p} + A)^2 + V(r) \tag{3.34}$$

where we define $V(r) = \sum_{i=1}^{L} V(r - R_i)$ and $A = A(r,t)$ for brevity. Furthermore, the spin index is left out, since the same value of the quantity we wish to calculate is obtained regardless of the spin. By substituting equation 3.34 into equation 3.9 is can be seen that the Hamiltonian in equation 3.14 will contain the modified hopping matrix elements

$$t_{ij}(t) = \int dr w^*(r - R_i)\big[\frac{1}{2}(\hat{p} + A(r,t))^2 + V(r)\big]w(r - R_j) \tag{3.35}$$

For a differentiable complex valued function, $\lambda = \lambda(r,t)$, the following relation holds

$$(\hat{p} + A)^2 w(r) = e^{-i\lambda}\big(\hat{p} + (A - \frac{\partial}{\partial r}\lambda)\big)^2 e^{i\lambda} w(r) \tag{3.36}$$

where $\phi(r)$ can be considered an arbitrary trial function. By working from the right hand side of the equation,

$$\begin{aligned} &e^{-i\lambda}\hat{p}^2 e^{i\lambda} w(r) \\ &= (\frac{\partial}{\partial r}\lambda)^2 w(r) - i(\frac{\partial^2}{\partial r^2}\lambda)w(r) + 2(\frac{\partial}{\partial r}\lambda)(\hat{p}w(r)) + \hat{p}^2 w(r) \end{aligned} \tag{3.37}$$

Moreover,

$$\begin{aligned} &e^{-i\lambda}\hat{p}(A - \frac{\partial}{\partial r}\lambda)e^{i\lambda} w(r) \\ &= (\hat{p}A)w(r) + A(\frac{\partial}{\partial r}\lambda)w(r) + A(\hat{p}w(r)) + i(\frac{\partial^2}{\partial r^2}\lambda)w(r) \\ &- (\frac{\partial}{\partial r}\lambda)^2 w(r) - (\frac{\partial}{\partial r}\lambda)(\hat{p}w(r)) \end{aligned} \tag{3.38}$$

and

$$\begin{aligned} &e^{-i\lambda}(A - \frac{\partial}{\partial r}\lambda)\hat{p}e^{i\lambda} w(r) \\ &= (A - \frac{\partial}{\partial r}\lambda)\big((\frac{\partial}{\partial r}\lambda)w(r) + \hat{p}w(r)\big) \end{aligned} \tag{3.39}$$

Lastly,

$$\begin{aligned} &e^{-ie\lambda}(A - \frac{\partial}{\partial r}\lambda)^2 e^{i\lambda} w(r) \\ =&A^2 w(r) - A(\frac{\partial}{\partial r}\lambda)w(r) - (\frac{\partial}{\partial r}\lambda)Aw(r) + (\frac{\partial}{\partial r}\lambda)^2 w(r) \end{aligned} \tag{3.40}$$

By defining

$$\lambda(r,t) = \int_{r_0}^{r} dy A(y,t) \tag{3.41}$$

where r_0 is some arbitrary fixed point, it is immediate from the fundamental theorem of calculus that

$$\frac{d}{dr}\lambda(r,t) = A(r,t) \tag{3.42}$$

Now, the modified matrix element can be interpreted as arising from the substitution

$$w(r-R_j) \longrightarrow \tilde{w}(r-R_j) = w(r-R_j)e^{i\lambda(r,t)} \tag{3.43}$$

in equation 3.10. Furthermore, since the upper integration limit of λ is r, i.e., the position of the electron, we may approximate

$$w(r-R_j)e^{i\lambda(r,t)} \approx w(r-R_j)e^{i\lambda(R_j,t)} \tag{3.44}$$

since the electron is highly localized around R_j. Upon applying this result to the time dependent matrix element, equation 3.35, we obtain

$$t_{ij}(t) \approx e^{i(\lambda(R_j,t)-\lambda(R_i,t))}t_{ij} \approx e^{i(j-i)aA(t)}t_{ij} \tag{3.45}$$

where we in the first approximation have defined

$$t_{ij} = \int dr w^*(r-R_i)\Big[\frac{\hat{p}^2}{2} + V(r)\Big]w(r-R_j) \tag{3.46}$$

and in the second approximation employed the dipole approximation, explicitly stated as

$$\lambda(R_j,t) - \lambda(R_i,t) = \int_{r_0}^{R_j} dy A(y,t) + \int_{R_i}^{r_0} dy A(y,t) \approx A(t)(R_j - R_i) \tag{3.47}$$

With the modified matrix element in equation 3.46, the Hubbard Hamiltonian, equation 3.17, assumes the following form

$$\hat{H}(t) = -t_0 \sum_{\sigma}\sum_{j=1}^{L}\left(e^{iaA(t)}\hat{c}^{\dagger}_{j,\sigma}\hat{c}_{j+1,\sigma} + h.c\right) + U\sum_{j=1}^{L}\hat{n}_{j,\uparrow}\hat{n}_{j,\downarrow} \tag{3.48}$$

3.4 The current operator

The continuity equation is given as

$$\frac{\partial\rho(\boldsymbol{r},t)}{\partial t} + \boldsymbol{\nabla}\boldsymbol{J}(\boldsymbol{r},t) = 0 \tag{3.49}$$

where $\rho(\boldsymbol{r},t)$ is some density, while $\boldsymbol{J}(\boldsymbol{r},t)$ is the current of that density. Equation 3.49 is well known from examples in e.g. fluid mechanics and can be stated for quantum mechanical observables as well. In order to see this, the Heisenberg equation of motion approach is applied to the number density at site j for electrons with spin σ as follows

$$\frac{d}{dt}\hat{n}_{j,\sigma} = i\big[\hat{H}(t), \hat{n}_{j,\sigma}\big] \tag{3.50}$$

where $\hat{H}(t)$ is the Hamiltonian of equation 3.48. Upon calculating the commutator above, the following result is obtained

$$\begin{aligned}&\frac{d}{dt}\hat{n}_{j,\sigma}\\&= -it_0[e^{iaA(t)}(\hat{c}^{\dagger}_{j-1,\sigma}\hat{c}_{j,\sigma} - \hat{c}^{\dagger}_{j,\sigma}\hat{c}_{j+1,\sigma})\\&+ e^{-iaA(t)}(\hat{c}^{\dagger}_{j+1,\sigma}\hat{c}_{j,\sigma} - \hat{c}^{\dagger}_{j,\sigma}\hat{c}_{j-1,\sigma})]\end{aligned} \tag{3.51}$$

It is readily seen that upon identifying

$$\hat{j}_{j,\sigma} = -it_0[e^{iaA(t)}(\hat{c}^{\dagger}_{j-1,\sigma}\hat{c}_{j,\sigma} - h.c.] \tag{3.52}$$

equation 3.51 can be written as

$$\frac{d}{dt}\hat{n}_{j,\sigma} + \hat{j}_{j,\sigma} - \hat{j}_{j-1,\sigma} = 0 \tag{3.53}$$

Since the starting point was the number density, $\hat{n}_{j,\sigma}$, the quantity $\hat{j}_{j,\sigma}$ can in light of equation 3.49 be interpreted as a current density for electrons with spin σ at site j. Moreover, The total charge current density operator is defined in the following way

$$\hat{J}_{\rho}(t) = -\sum_{\sigma}\sum_{j=1}^{L}\hat{j}_{j,\sigma} \tag{3.54}$$

To get the total current operator, simply multiply $\hat{J}_{\rho}(t)$ by the lattice constant, a. The result is given explicitly as

$$\hat{J}(t) = iat_0\sum_{\sigma}\sum_{j=1}^{L}[e^{iaA(t)}\hat{c}^{\dagger}_{j,\sigma}\hat{c}_{j+1,\sigma} - h.c.] \tag{3.55}$$

where we have shifted $j \longrightarrow j+1$ with respect to definition 3.52. [29] Before considering the interacting properties of our system in the context of HHG, a bit of theory regarding the $U = 0$ limit of the Hamiltonian in equation 3.48 will be presented. This will provide a context for the analysis of our results in the final section.

Chapter 4

High Harmonic Generation

4.1 HHG in single band models

Most of current research into HHG attributes the emission of radiation to two fundamental mechanisms - intraband acceleration and interband tunneling. [10] [38] [39] Intraband acceleration is when an electron gains crystal momentum as a result of acceleration in the electromagnetic field. [11] Interband processes describe the field induced transitions between bands. Both processes occur in for instance semiconductors. Often, the initial state of a semiconductor is modelled as system with an initially filled valence band and an empty conduction band prior to pulse-excitation. [32] If the valence band electrons populates the entire Brillouin zone, no current can flow. Therefore, any laser induced current in this system necessitates an interband process to pump the electrons into the conduction band.

Realistically, light matter coupling in a condensed matter system will involve an interplay between different bands in addition to intraband acceleration. [5] However, one can gain insight into the process by considering a one band model. There are a couple of physical scenarios that justifies such a description. Firstly, in a metal, for which the Fermi energy is located in the middle of the conduction band [29], electrons may be excited above the Fermi level and subsequently accelerated in momentum space without necessarily jumping to a higher energy band due to Zener tunneling. [30] Another approach is to assume that while initially unpopulated, most of the population in the valence band has been pumped by interband transitions into the conduction band. The time evolution can be initiated at this point. [40] Hence, only a part of the full process is modeled. Even though the described scenarios might sound like an oversimplification, it can be helpful to get some familiarity with it before delving into the study of more complex systems.

4.1.1 Current operator

To demonstrate the abovementioned acceleration process, consider the macroscopic current in a system

$$\begin{aligned}\left\langle \hat{J}(t)\right\rangle &= \sum_{\sigma}\sum_{k}\frac{\partial}{\partial k}\epsilon(k)\left\langle \hat{c}^{\dagger}_{k,\sigma}\hat{c}_{k,\sigma}\right\rangle \\ &= \sum_{\sigma}\sum_{k}\frac{\partial}{\partial k}\epsilon(k)n_{\sigma}(k) \\ &:= \sum_{k}\frac{\partial}{\partial k}\epsilon(k)n(k)\end{aligned} \tag{4.1}$$

expressed as a sum in momentum space. [5] $\epsilon(k)$ is the momentum dispersion, and $n_\sigma(k)$ is the population of electrons of spin σ with crystal momentum k. In the last equality, we defined $n(k) = n_\downarrow(k) + n_\uparrow(k)$. According to Bloch's acceleration theorem [30], the effect of an electromagnetic field on the crystal momentum may be expressed as

$$\frac{\partial k(t)}{\partial t} = -E(t) \tag{4.2}$$

giving

$$k(t) = k(0) - \int_0^t E(t')dt' = k(0) + A(t) \tag{4.3}$$

using equation 2.19 with $\Phi = 0$. There are two ways to conceive of this result, each of which amounts to a particular reference frame. One choice for the remainder of the thesis falls upon the reference frame in which the dispersion is time dependent, giving the following expression for the current

$$J(t) = \sum_{\sigma}\sum_{k}\frac{\partial}{\partial k}\epsilon(k(0) + A(t))n_{\sigma}(k(0)) \tag{4.4}$$

[5]. For the proof of the correspondence between equation 4.4 and equation 3.55, the reader may consult appendix A.

In order to gain some intuition about the transient location of the electrons in momentum space, we must let the population vary in time, while keeping the dispersion time independent. Such a distribution is governed by the following partial differential equation

$$\frac{d}{dt}n(k(t)) = -E(t)\frac{\partial}{\partial k}n(k(t)) \tag{4.5}$$

which is deduced from

$$\frac{d}{dt}n(k(t)) = \frac{\partial k}{\partial t}\frac{\partial n}{\partial k} \tag{4.6}$$

and equation 4.2. A solution to equation 4.5 is a Gaussian electron distribution

$$n(k(t)) = \exp\left\{-\frac{(k(0) + A(t))^2}{2\sigma^2}\right\} \tag{4.7}$$

where σ is its standard deviation. [1] Lastly, in this frame of reference, the current operator admits the form

$$J(t) = \sum_k \frac{\partial \epsilon(k)}{\partial k} n(k(t)) \tag{4.8}$$

Because of the time dependence in equation 4.8, it is possible to view the electron distribution as a function of time. It is a good assumption to start with a conduction band filled with electrons according to a Gaussian distribution in k-space. [40] In equation 4.7, we use $\sigma = \frac{\pi}{4a}$ along with the lattice parameter $a = 7.1739$ [a.u.]. As a result of applying the pulse specified in the beginning of chapter 6, the current in the bottom panel of figure 4.1 is obtained. A notable feature of the bottom panel in figure 4.1 is the appearance of kinks at the location of high electric field strengths. Upon adopting the viewpoint of equation 4.7, this can be explained in terms of figure 4.2.

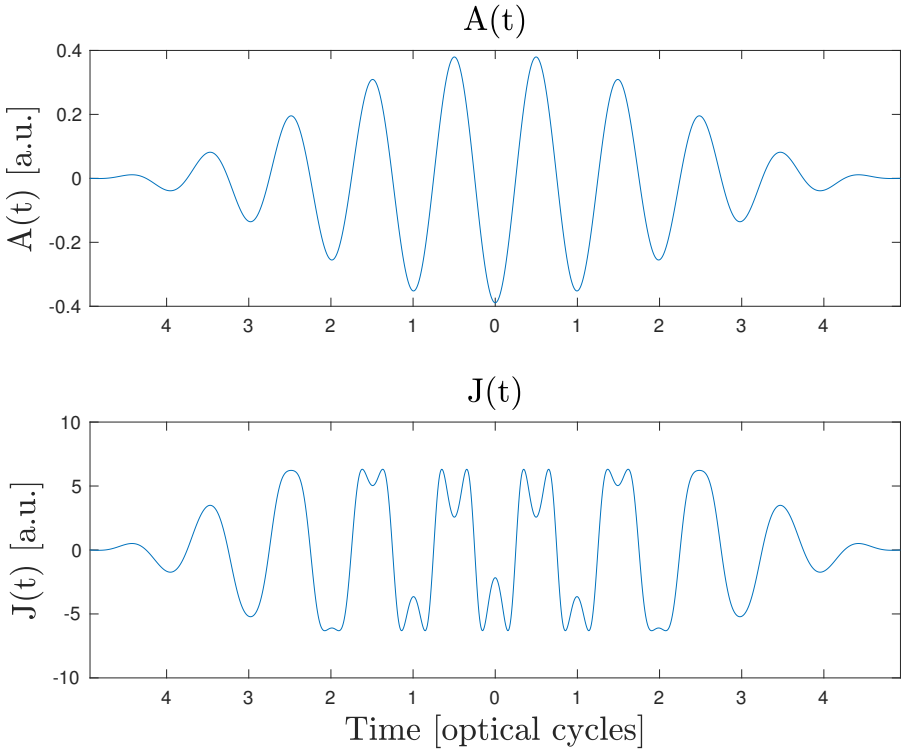

Figure 4.1: Macroscopic current obtained by modeling the time evolution of the Gaussian distribution of electrons in equation 4.7 in the Brillouin zone.

4.1.2 Bloch Oscillations

In the bottom panel of figure 4.2 the population of electrons in the Brillouin zone is indicated as a function of time. Observe that electrons reaching the boundary of the Brillouin zone will reappear on the other side, yielding a rapid change in crystal momentum. Most notably, said events correspond to the aforementioned kinks in the total current, which has also been plotted in the top panel of figure 4.2. In real space,

[1] This is not to be confused with the electron spin. However, for the remaining part of this chapter, spin is not used.

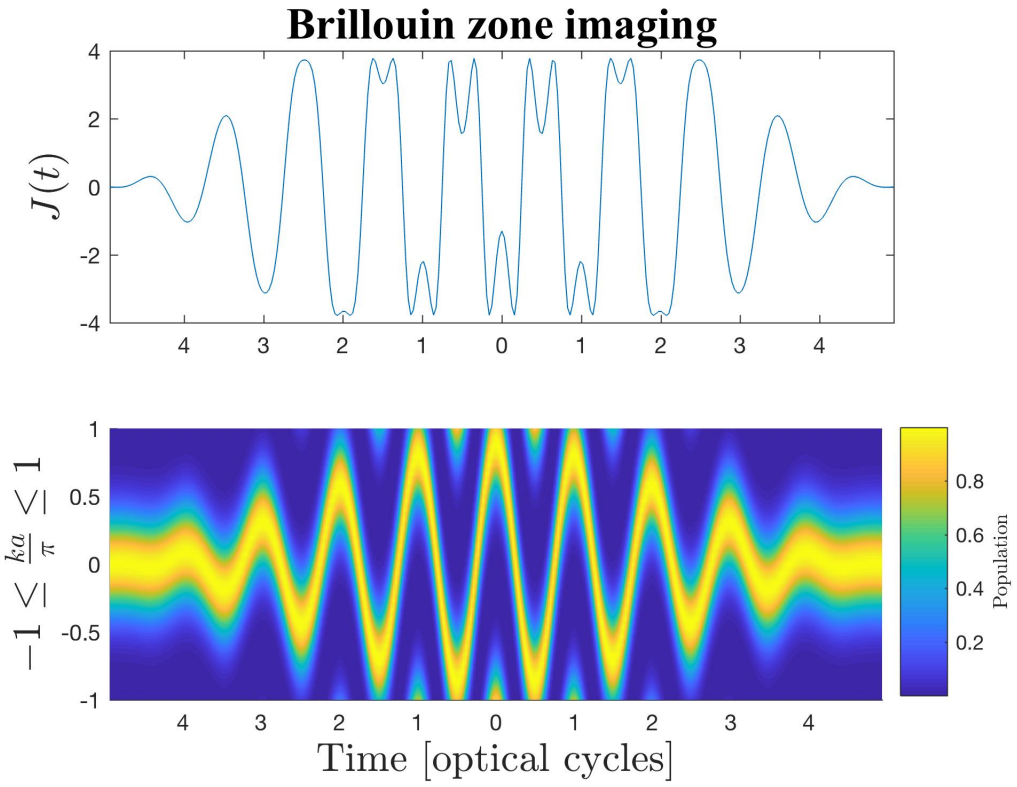

Figure 4.2: Dynamical Bloch Oscillations modeled by an initial Gaussian electron distribution

these processes correspond to *Bragg scattering* - a process in which the electron wave scatters off the lattice. [14] This is conceivable since when the crystal momentum approaches $\frac{\pi}{a}$, the wavelength is short enough to reach the scattering condition, and thus the electron crystal momentum undergoes a rapid change. The current seemingly aquires higher frequency components due to this process when analyzing figure 4.2. The contribution of these higher frequency components to the current can be assessed by a Fourier transform. Moreover, this is the procedure followed in order to analyze the frequency components in the emitted light, since an accelerating charge radiates. [25] To predict the amount of radiation, the dipole acceleration, $\frac{d}{dt}J(t)$, is the relevant quantity. [1] [8]

$$I_{\text{rad}}(\omega) \propto \left| \int \frac{d}{dt} J(t) e^{i\omega t} \right|^2 = |i\omega J(\omega)|^2 \tag{4.9}$$

The result is shown in figure 4.3. Interestingly, only harmonics of odd order give contributions here. It will in the following be shown that this is a general property of solid state systems, with the exception of more complex pulse conditions. [23]

In order to explain the observed characteristics of figure 4.3, especially the appearance of odd order harmonics, define

$$\omega_B(t) = aE(t) \tag{4.10}$$

which can be used to restate the acceleration theorem, equation 4.2, in a different way

$$a\frac{d}{dt}k(t) = -\omega_B(t) \tag{4.11}$$

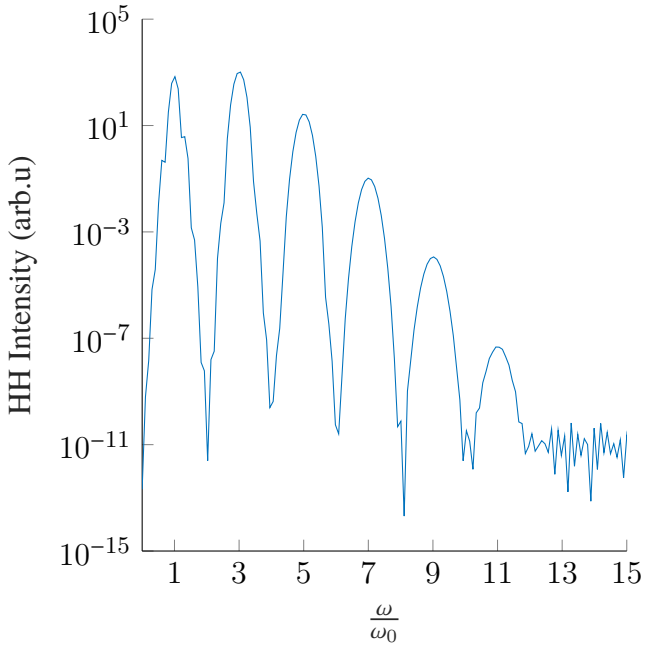

Figure 4.3: Resulting HHG spectrum from the parameters outlined in the two previous figures. ω_0 is the carrier wave frequency of $A(t)$. For details of the laser pulse, the reader is referred to chapter 6

for which the most simple instance is the static field case. Here, the crystal momentum has the following simple time dependence

$$k(t) = \frac{-t\omega_B}{a} \tag{4.12}$$

Now, as $t = \frac{\pi}{\omega_B}$ the electron has reached the end of the Brillouin zone. The condition when $|k| = \frac{\pi}{a}$ is the Bragg scattering condition. To emphasize the quantum mechanical aspect of this, note that ω_B is the same as a potential drop between two lattice sites. The effect of the light matter interaction is to modify the potential into that of a tilted potential, and as a result lead to Wannier Stark Localization.[2] [13]

The tight binding band structure from equation 2.44, together with the definition of the group velocity [41], gives

$$v_g = \frac{d\epsilon(k)}{dk} = 2t_0 a \sin(ka) \tag{4.13}$$

To make the analysis simple, consider the following AC-field

$$\Omega_B(t) = \Omega_B \cos(\omega_0 t) \tag{4.14}$$

From the acceleration theorem, we see that

$$k(t) = -\frac{\Omega_B}{a\omega_0} \sin(\omega_0 t) \tag{4.15}$$

[2]In fact, a periodic lattice admits the same tilted shape as in figure the picture seen in the context of HHG in atomic systems, see figure 1.3. This is made particularly clear when writing the Hamiltonian in 2.25 in the length gauge.

which combined with the expression of the group velocity, $v_g(k) = \frac{\partial \epsilon(k)}{\partial k}$, and the fact that $\omega(k) = \epsilon(k)$ (in atomic units) yields

$$v_g = -2at_0 \sin\left(\frac{\Omega_B}{\omega_0}\sin(\omega_0 t)\right) \tag{4.16}$$

This equation can be conveniently expressed with the help of the Bessel function of the first kind [42]

$$v_g = -4at_0 \sum_{M=0}^{\infty} \mathcal{J}_{2M+1}(\frac{\Omega_B}{\omega_0})\sin((2M+1)\omega_0 t) \tag{4.17}$$

It is convenient to introduce such a spectral resolution of the group velocity, because one can at once identify its Fourier components as

$$v_g(N\omega_0) = \mathcal{J}_N(\frac{\Omega_B}{\omega_0}) \tag{4.18}$$

whence it is seen that only odd order harmonics are present. Now, to calculate the energy resolved intensity of radiation, we turn to equation 4.9, i.e.

$$I_{\text{rad}}(N\omega_0) = \left|\int \frac{dv_g(t)}{dt} e^{iN\omega_0 t}\right|^2 = \left|iN\omega_0 v_g(N\omega_0)\right|^2 \propto (N\omega_0)^2 \mathcal{J}_N^2(\frac{\Omega_B}{\omega_0}) \tag{4.19}$$

However, this theoretical framework also lets us speak about the field field dependence of the harmonic radiation. Specifically, one can with the theory developed inquire what the highest frequency components observed in the spectrum are. If we in equation 4.16 let $\frac{\Omega_B}{\omega_0} >> 1$, we may approximate

$$v_g(t) \propto \sin(\Omega_B t) \tag{4.20}$$

for the times around $t = 0, \frac{\pi}{\omega_0}, \ldots$, since the inner $\sin$ function in equation 4.16 can be approximated by its argument. Thus, at these times the group velocity oscillates with a frequency dictated by the field strength through Ω_B in equation 4.10. Since this is the maximal frequency component, a cut off behaviour can be deduced as

$$N_{\text{max}} \approx \frac{\Omega_B}{\omega_0} \tag{4.21}$$

As for the Bessel functions in equation 4.17, they introduce nodes in the harmonic spectrum as a function Ω_B. In comparing this result with the cut off relation in the three step model in the introduction, equation 1.2, equation 4.21 displays a different cut off scaling. That is, atoms exhibit a quadratic scaling with field strength, whereas in intraband processes, the scaling is linear in field strength.

4.2 A three step model in solids

The celebrated three step model was laid out in the introduction, and has provided useful insight into HHG in atoms. In an attempt to settle the issue of the importance of inter and intraband processes, something reminiscent of a a three step model has been

employed in the solid state counterpart as well. [16] [11] To explain the process in a three step model, one imagines the buildup of interband polarization as the tunneling step. Physically, this amounts to electron-hole pairs being created. After that, the newly created pairs are accelerated towards higher momenta by the electromagnetic field - the acceleration step. Lastly, once the excited electrons recombine with the holes, radiation is emitted - the recombination step. In the atomic three step model promulgated by Lewenstein et. al. [7] it is only the third process that is *assumed* to give rise to radiation. This turns out to be a good approximation to atomic systems. In solids however, it is rather the last couple of processes that are at play.

In this section, we made some strides towards an analytic treatment of HHG in a single band model. However, as remarked earlier, the inclusion of significant correlation effects renders most analytical methods inadequate. Although the analytical methods end here, it will be the subject of the following chapter to develop an algorithm capable of treating the Hubbard Hamiltonian in generality and as a result gain further insight into the process of HHG.

Chapter 5

Numerical Methods

This chapter will contain an elaboration on the theory required to solve the Hubbard model in a time dependent setting. The theory presented herein will also prove relevant for time independent problems, as solving the time independent problem is necessitated in finding an initial condition prior to pulse excitation of the system.

5.1 Exact diagonalization

The mathematical problem at hand has been formulated in equations 2.2 and 3.48. It will be the purpose of this chapter to present a numerical scheme capable of solving these equations. It is clearly the chief purpose of any numerical method to present as few approximations as possible on top of the mathematical problem it is intended to solve. The method presented herein benefits in this regard due to the fact that there are few approximations made beyond the Hubbard Hamiltonian 3.48. This advantage lends itself to the discrete nature of lattice Hamiltonians in condensed matter systems.

Recall that when equation 2.73 is expressed in the Wannier basis, the electrons in the Hubbard model can be said to reside on specific lattice points. Hence, the available positions of an electron on the lattice is not a continuum, as opposed to e.g. the position of an electron in free space. Thus, one basis element is merely the placement of each electron in the system on lattice sites in accordance with the Pauli exclusion principle.

Exact diagonalization refers to the generation of a basis comprised of all possible configurations of the system and the generation of the system Hamiltonian in this basis. The first step towards a numerical description of the Hubbard model is to implement a basis over which the Hamiltonian of the system can be expressed. The method employed here is conceptually simple, and has been used extensively for these types of problems. [43] [44] [45]

5.1.1 Symmetries

The reader may already infer that the difficulty in solving the problem at hand lies in the exponential growth in system size when solving systems with many sites and many electrons. Therefore, one should make use of the symmetries provided by our Hamiltonian. If a Hamiltonian admits a certain symmetry, then it can be brought onto a block diagonal form. The implication being a reduction of the problem into smaller chunks. A symmetry of the Hamiltonian can be expressed as an operator $\hat{O}$ for which

$\left[\hat{O}, \hat{H}\right] = 0$. [43] As long as this relation is fulfilled, a system that is in an eigenstate of the operator $\hat{O}$ will remain so for the course of the time evolution. As a result, during the dynamics of the system, there is no crossover between eigenstates belonging to different block-diagonals in the Hamiltonian matrix. For the Hubbard model in equation 3.48, the following symmetries will be applied

1. Spin symmetry:

$$\hat{S}_\alpha = \frac{1}{2} \sum_{i=1}^{L} \sum_{\mu=\uparrow,\downarrow} \sum_{\nu=\uparrow,\downarrow} \hat{c}^\dagger_{i,\mu} \sigma_\alpha^{\mu,\nu} \hat{c}_{i,\nu} \tag{5.1}$$

   where L is the number of sites in the system and $\sigma_\alpha^{\mu,\nu}$ are the Pauli matrices

$$\sigma_x = \begin{pmatrix} 0 & 1 \\ 1 & 0 \end{pmatrix}, \sigma_y = \begin{pmatrix} 0 & -i \\ i & 0 \end{pmatrix}, \sigma_z = \begin{pmatrix} 1 & 0 \\ 0 & -1 \end{pmatrix} \tag{5.2}$$

   and $\hat{c}^\dagger_{i,\mu}$ ($\hat{c}_{i,\mu}$) is the creation (annihilation) operator of an electron with spin μ in the Wannier orbital at site i. Specifically, we will use the $\hat{S}_z$ symmetry.

2. Particle number symmetry:

$$\hat{N}_e = \sum_{\sigma} \sum_{i=1}^{L} \hat{n}_{i,\sigma} \tag{5.3}$$

In figure 5.1 we display the symmetry of $\hat{N}_e$ alone for the case of 6 sites. The left panel partitions the Hamiltonian into block diagonals according to different values of N_e. In the right panel, the sparsity pattern of the largest subspace, $N_e = 6$, is shown.

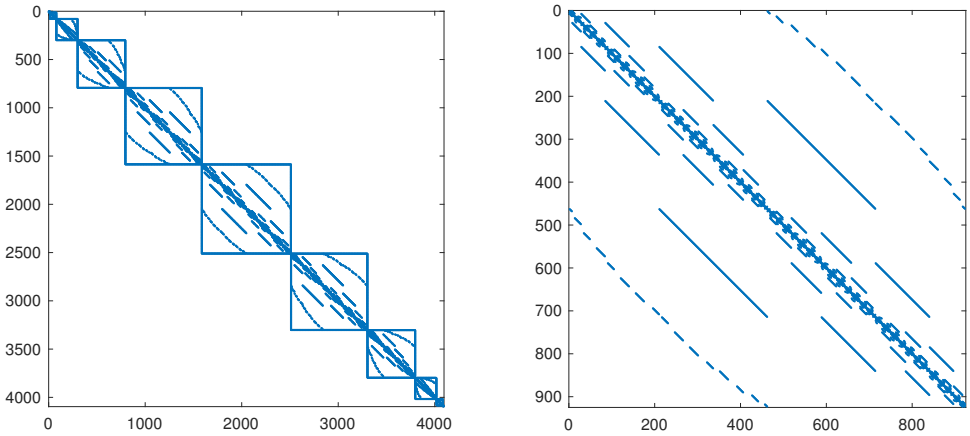

Figure 5.1: The left panel shows the different subspaces of $\hat{N}_e$ for L=6. In the right panel, the subspace of $N_e = 6$. For the Hamiltonian used to make these figures, no use of the $\hat{S}_z$ symmetry has been made.

Prior to exploiting any symmetries, note that the Hubbard model for L sites has

$$\begin{aligned}&\sum_{N_\downarrow=0}^{L}\sum_{N_\uparrow=0}^{L}\binom{L}{N_\downarrow}\binom{L}{N_\uparrow}\\&=2^L2^L=4^L\end{aligned} \tag{5.4}$$

possible configurations, where $N_\downarrow$ is the number of spin down electrons and $N_\uparrow$ the number of spin up electrons. As explained in chapter 3, the configuration referred to as *half filling* is a system for which $N_e = L$. If we additionally require that $S_z = 0$, equation 5.4 gives $\left(\frac{L}{\frac{L}{2}}\right)^2$ configurations. In comparing the number of configurations with and without the use of these symmetries, we get

$$\frac{4^L}{\left(\frac{L}{\frac{L}{2}}\right)^2}\approx\frac{\pi L}{2} \tag{5.5}$$

Thus, in going to the subspace of half filling granted by the symmetry of fixed particle number, and the $S_z = 0$ subspace, the dimension of the problem has been reduced by roughly a factor of L. Generally, the utility of symmetry reductions does not keep up with the exponential growth of the problem as system size increases. Therefore, it will not be of interest to look into other symmetries than spin and particle number conservation in this thesis. *For the remaining part of the thesis, the subspaces of $S_z = 0$ and $N_e = L$ (half filling) will be used unless stated otherwise.*

5.1.2 Conventions

Before embarking on the process of tackling the problem numerically, some conventions must be adhered to. A general element of our basis can be devised as follows

$$|\phi_m\rangle = [\hat{c}^\dagger_{m_1,\downarrow}\hat{c}^\dagger_{m_2,\downarrow}\ldots\hat{c}^\dagger_{m_{\frac{L}{2}},\downarrow}][\hat{c}^\dagger_{\overline{m}_1,\uparrow}\hat{c}^\dagger_{\overline{m}_2,\uparrow}\ldots\hat{c}^\dagger_{\overline{m}_{\frac{L}{2}},\uparrow}]\,|\rangle = \left|\phi_\downarrow\right\rangle\left|\phi_\uparrow\right\rangle \tag{5.6}$$

where again $|\rangle$ is the vacuum state, and the state is partitioned into sectors of different spin for the ease of computation. The two sets $\{m_i\}$ and $\{\overline{m}_i\}$ are sets of lattice positions, each with $\frac{L}{2}$ elements. Spin down operators are placed to the left of spin up operators as a convention. Secondarily, a convention of letting the site indices increase from left to right is defined. In symbolic terms, if $i < j$, then $m_i < m_j$ and $\overline{m}_i < \overline{m}_j$. The next step would be to evaluate the action of each term in the Hamiltonian, equation 3.17, on the basis states above. For the hopping term of equation 3.17, this amounts to

$$\begin{aligned}&\hat{c}^\dagger_{i,\uparrow}\hat{c}_{i+1,\uparrow}\left|\phi_\uparrow\right\rangle\\&=[\hat{c}^\dagger_{m_1,\downarrow}\hat{c}^\dagger_{m_2,\downarrow}\ldots\hat{c}^\dagger_{m_{\frac{L}{2}},\downarrow}]\hat{c}^\dagger_{i,\uparrow}\hat{c}_{i+1,\uparrow}[\hat{c}^\dagger_{\overline{m}_1,\uparrow}\hat{c}^\dagger_{\overline{m}_2,\uparrow}\ldots\hat{c}^\dagger_{\overline{m}_{\frac{L}{2}},\uparrow}]\,|\rangle\end{aligned} \tag{5.7}$$

where an even number of fermion exchanges have been performed. For the subsequent action of $\hat{c}^{\dagger}_{i,\uparrow}\hat{c}_{i+1,\uparrow}$ on the spin up sector, we get

$$\begin{aligned}
&\hat{c}^{\dagger}_{i,\uparrow}\hat{c}_{i+1,\uparrow}\,|\phi_m\rangle \\
&= \hat{c}^{\dagger}_{i,\uparrow}\hat{c}_{i+1,\uparrow}[\hat{c}^{\dagger}_{\overline{m}_1,\uparrow}\hat{c}^{\dagger}_{\overline{m}_2,\uparrow}\ldots\hat{c}^{\dagger}_{\overline{m}_{\frac{L}{2}},\uparrow}]\,|\rangle \\
&= \underbrace{[\hat{c}^{\dagger}_{\overline{m}_1,\uparrow}\hat{c}^{\dagger}_{\overline{m}_2,\uparrow}\ldots\hat{c}^{\dagger}_{\overline{m}_l,\uparrow}}_{2l \text{ fermion exchanges}}\hat{c}^{\dagger}_{i,\uparrow}\hat{c}_{i+1,\uparrow}\ldots\hat{c}^{\dagger}_{\overline{m}_{\frac{L}{2}},\uparrow}]\,|\rangle = |\phi_n\rangle
\end{aligned} \tag{5.8}$$

with the purpose of showing that signs arising from anti-commutation operations is usually unproblematic. An important caveat is the treatment of periodic boundary conditions (equation 3.16) since hopping processes on the system boundary will give rise to minus signs. For the electron interaction term in the equation 3.45, the action is simply

$$\begin{aligned}
&\hat{n}_{i,\downarrow}\hat{n}_{i,\uparrow}\,|\phi_m\rangle \\
&= \hat{n}_{i,\downarrow}[\hat{c}^{\dagger}_{m_1,\downarrow}\hat{c}^{\dagger}_{m_2,\downarrow}\ldots\hat{c}^{\dagger}_{m_{\frac{L}{2}},\downarrow}]\hat{n}_{i,\uparrow}[\hat{c}^{\dagger}_{\overline{m}_1,\uparrow}\hat{c}^{\dagger}_{\overline{m}_2,\uparrow}\ldots\hat{c}^{\dagger}_{\overline{m}_{\frac{L}{2}},\uparrow}]\,|\rangle = \delta_{1,m_i}\delta_{1,\overline{m}_i}\,|\phi_m\rangle
\end{aligned} \tag{5.9}$$

and the algorithmic procedure is just a matter of counting the number of occupied sites, whence no off diagonal matrix elements are created.

5.1.3 Basis generation

Proceeding to the more practical aspects, the states need to be stored in memory somehow. The basis states can be stored as binary numbers conforming to the following enumeration scheme,

$$|\phi_m\rangle = \left|m'_1, m'_2, \ldots, m'_L\right\rangle \left|\overline{m}'_1, \overline{m}'_2, \ldots, \overline{m}'_L\right\rangle \tag{5.10}$$

where $\{m'_i\}$ and $\{\overline{m}'_i\}$ are given the numbers 0 or 1 denoting a vacant site or an occupied site, respectively. Example states for L=4 are

$$\begin{aligned}
&|1,0,1,0\rangle\,|0,1,1,0\rangle \\
&|1,1,0,0\rangle\,|0,1,1,0\rangle \\
&|0,0,1,1\rangle\,|1,0,1,0\rangle \\
&\vdots
\end{aligned} \tag{5.11}$$

among a total of $\binom{4}{2}^2 = 36$ basis states. Below, a pseudocode is made to illustrate the creation of the basis set subject to the constraint of half filling and $S_z = 0$. See algorithm 1.

We showed the representation in terms of binary numbers, as it is much easier to do manipulations, i.e., act with the Hubbard Hamiltonian in equation 3.48 on the binary representation as exemplified in equation 5.11. However, it is less memory demanding to store them in the decimal representation. Therefore, a transformation between these representations is desired. To this end, we need to resort to a "look up" table of sorts in

Algorithm 1 Algorithm for basis generation at half filling and $S_z = 0$

```
1: function Basis(L)                                   ▷ L is the number of sites in the system
2:     sz = (L choose L/2)                             ▷ Number of configurations in one spin sector
3:     spinsector(1:sz)=0 ▷ Allocate space for the configurations for the spin up/down sector
4:     for g = 1 to sz do                              ▷ Loop over the number of elements in this spin sector
5:         dec = 0                                     ▷ The decimal number of the state
6:         occup = 0                                   ▷ Number of electrons in the spin sector
7:         for i = 0 to L − 1 do                       ▷ Loop over the lattice sites
8:             if occup < L/2 − 1] then
9:                 binar ← randint(0, 1)               ▷ Random integer 0 or 1 is assigned
10:                adder ← binar × 2^i
11:                if binar = 1 then
12:                    occup + 1 ← occup
13:                else
14:                    Continue                        ▷ A sufficient number of electrons is reached
15:                end if
16:            else if i == L − 1 and occup < L/2 then ▷ Condition for adding electrons
17:                binar = 1
18:                binar ∗ 2^i ← adder
19:                occup + 1 ← occup
20:            else if occup > L/2 − 1 then
21:                continue
22:
23:            end if
24:            dec ← dec + adder
25:        end for
26:        if g > 1 and dec ∈ spinsector then ▷ Determine if you have already made the state
27:            continue
28:        else if dec not in spinsector and occup == L/2 then
29:            flag = 0
30:        end if
31:        if flag == 0 then
32:            break
33:        end if
34:        spinsector(g) = dec                         ▷ Resulting decimal number is added to "spinsector"
35:    end for
36: end function
```

order to go back and forth between these representations in a one to one correspondence. Realizing the described one-to-one correspondence between the decimal and the binary representations calls for a function, for which the following is employed

$$I = I_{\downarrow} + 2^{L} I_{\uparrow} \tag{5.12}$$

where I is an index that enumerates the basis state in equation 5.9, and I_{σ} are binary numbers pertaining to the spin σ sector. There are different ways of assigning a decimal number to the different sectors of the state in equation 5.10. One way is according to

the prescription

$$\begin{aligned} \left|m'_1, m'_2, \ldots, m'_L\right\rangle &\longmapsto I_\downarrow = \sum_{i=0}^{L-1} m'_{L-i} \times 2^i \\ \left|\overline{m}'_1, \overline{m}'_2, \ldots, \overline{m}'_L\right\rangle &\longmapsto I_\uparrow = \sum_{i=0}^{L-1} \overline{m}'_{L-i} \times 2^i \end{aligned} \tag{5.13}$$

It is clear that given I, one can find $I_\downarrow$ in equation 5.12 as follows

$$I_\downarrow = \mathrm{mod}(I, 2^L) \tag{5.14}$$

and moreover,

$$I_\uparrow = (I - I_\downarrow)2^{-N} \tag{5.15}$$

In this way, the set of basis states of the system is simply stored in a column of maximally 4^L decimal numbers.

Algorithm 2 Algorithm for the generation of the decimal basis

```
1:  function DecimalBasis(sz)                ▷ Number of elements in spin up/down sector
2:      for i = 1 to sz do
3:          for j = 1 to sz do
4:              k = sz(i − 1) + j            ▷ Indexing the basis state
5:              I↑ = spinsector(i)
6:              I↓ = spinsector(j)
7:              I(k) = 2^L I↓ + I↑           ▷ Create the basis states in decimal representation
8:          end for
9:      end for
10:     sort(I) ← I                          ▷ Sort the vector in ascending order
11: end function
```

The code snippet above merely demonstrates the generation of the possible configurations in one spin sector. To make the decimal number pertaining to one of the actual basis states in equation 5.10, use the conversion formulas 5.14-5.15. A possible algorithm is based on taking random combinations of the states of the spin sectors, combine them according to the decimal formula 5.11 above to I, whence one obtains a long list of decimal numbers. One throws out non-unique/repeated instances of a states. Such an procudure is shown in algorithm 2.

5.1.4 Hamiltonian

The binary representation in equation 5.10 is the representation from which we create our Hamiltonian. Now, say that subsequent to the hopping term in equation 3.17 acting on a basis state, the following basis state is obtained

$$\hat{T}\,|\phi_m\rangle \rightarrow |\phi_n\rangle \tag{5.16}$$

As an example, a single term of the Hubbard Hamiltonian in equation 3.17 has the following effect on a basis state, $|\phi\rangle_m$

$$\begin{aligned} -t_0\hat{c}^{\dagger}_{2,\uparrow}\hat{c}_{2,\uparrow}\,|\phi_m\rangle &= -t_0\hat{c}^{\dagger}_{2,\uparrow}\hat{c}_{2,\uparrow}\,|0101\rangle_{\downarrow}\,|1010\rangle_{\uparrow} \\ &= -t_0\,|0101\rangle_{\downarrow}\,\hat{c}^{\dagger}_{2,\uparrow}\hat{c}_{2,\uparrow}\,|1010\rangle_{\uparrow} \\ &= -t_0\,|0101\rangle_{\downarrow}\,|1100\rangle_{\uparrow} \\ &= -t_0\,|\phi_n\rangle \end{aligned} \tag{5.17}$$

In order to know what element of the Hamiltonian this pertains to, i.e., what $|\phi_n\rangle$ is, a *binary search* must be performed. Simply transform $|\phi_n\rangle$'s binary representation to a decimal number, and then search to find the placement/index of the decimal number in the your decimal basis (as generated in algorithm 2). As a result you obtain two indices; one representing $|\phi_n\rangle$ and another representing $|\phi_m\rangle$. These two indices determine which slot in the Hamiltonian 3.17 gets filled. Algorithm 3 illustrates a way of creating a Hamiltonian matrix. Although algorithm 3 displays only the action of the hopping term in equation 3.17, it is easily extended to the full Hamiltonian.

Algorithm 3 Algorithm for the generation of $\hat{H}$

```
function HAMILTONIAN(Basis,sz)
    for g = 1 to sz^2 do
        |φ_g⟩ = |m_1, m_2, ..., m_L⟩_↓ |m_1, m_2, ..., m_L⟩_↑ ← I(g)   ▷ Decimal to binary.
        −t_0 |φ_g̃⟩ ← Ĥ |φ_g⟩
        I(g̃) ← Ĥ |φ_g⟩                                  ▷ Assign the state a decimal number
        g̃ ← I(g̃)                                        ▷ Perform a binary search for g̃
        Ĥ_{g̃,g} − t_0 ← Ĥ_{g̃,g}                         ▷ Append the matrix element to the Hamiltonian
    end for
end function
```

The sparsity pattern of the resulting Hamiltonian is shown in figure 5.2 for 12 sites. However, the sparsity matrix is obtained by performing algorithm 3 with the full Hamiltonian, equation 3.17. It is calculated that the number of non zero elements in this particular Hamiltonian makes up 0.0017% of the whole matrix.

5.2 Krylov subspace methods

To obtain the ground state in the exact basis, we turn to an often used method in many body calculations - namely the Lanczos method. [43] [44] [45] The utility of this method stems from the fact that the Hamiltonian 3.17 is a sparse matrix in the exact basis -

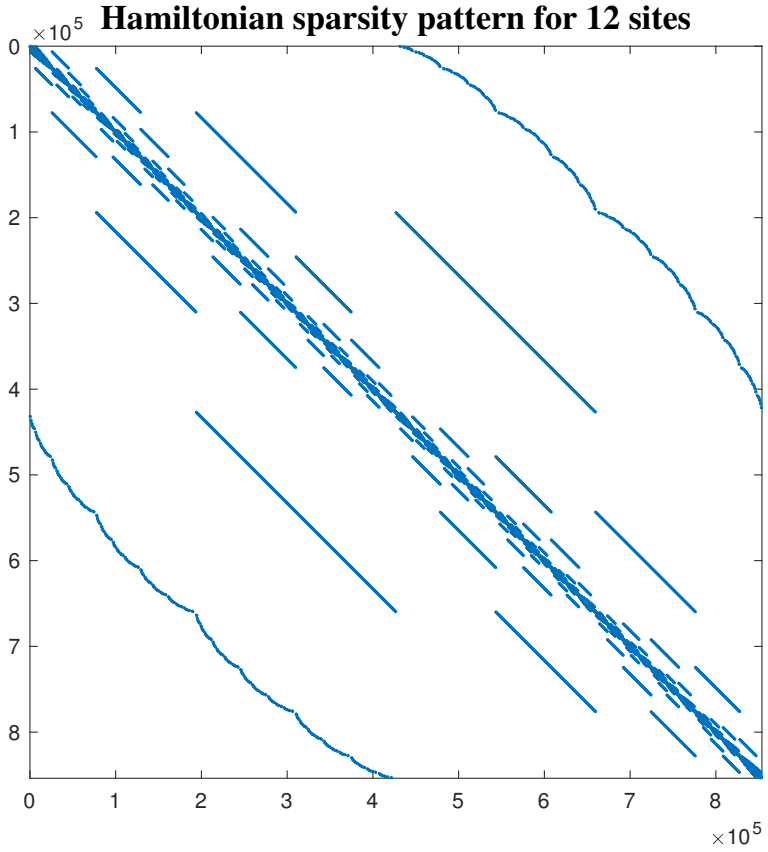

Figure 5.2: Sparsity pattern of the Hubbard Hamiltonian, equation 3.17 for 12 sites.

which can be seen as a result of the tight-binding approximation. A large dimension and sparsity makes our system ideally suited for the Lanczos algorithm. The procedure starts with a random, normalized vector, $\boldsymbol{q}_0$. A vector orthonormal to $\boldsymbol{q}_0$ can be found with the Gram-Schmidt procedure

$$\tilde{\boldsymbol{q}}_1 = \hat{H}\boldsymbol{q}_0 - (\boldsymbol{q}_0^\dagger \hat{H}\boldsymbol{q}_0)\boldsymbol{q}_0 \tag{5.18}$$

where

$$\beta_1 = \|\boldsymbol{q}_1\| \tag{5.19}$$

Cast in another way,

$$\hat{H}\boldsymbol{q}_0 = \boldsymbol{q}_1\beta + \alpha\boldsymbol{q}_0 \tag{5.20}$$

where

$$\alpha_0 = \boldsymbol{q}_0\hat{H}\boldsymbol{q}_0 \tag{5.21}$$

Further application of the above procedure will yield a tridiagonal matrix structure, for which the general recursion is given by

$$\hat{H}\boldsymbol{q}_j = \alpha_j\boldsymbol{q}_j + \beta_j\boldsymbol{q}_{j-1} + \beta_{j+1}\boldsymbol{q}_{j+1} \tag{5.22}$$

where

$$\alpha_j = \boldsymbol{q}_j^\dagger\hat{H}\boldsymbol{q}_j \tag{5.23}$$

$$\tilde{\boldsymbol{q}}_{j+1} = \hat{H}\boldsymbol{q}_j - \alpha_j\boldsymbol{q}_j - \beta_j\boldsymbol{q}_{j-1} \tag{5.24}$$

$$\beta_{j+1} = \left\| \tilde{\boldsymbol{q}}_{j+1} \right\| \tag{5.25}$$

and

$$\boldsymbol{q}_{j+1} = \frac{\tilde{\boldsymbol{q}}_{j+1}}{\beta_{j+1}} \tag{5.26}$$

The tridiagonal matrix structure is written as

$$\hat{H}_K = \begin{pmatrix} \alpha_0 & \beta_1 & 0 & \dots & 0 \\ \beta_1 & \alpha_1 & \beta_2 & \ddots & \vdots \\ 0 & \beta_2 & \ddots & \ddots & \vdots \\ \vdots & \ddots & \ddots & \ddots & \beta_{K-1} \\ 0 & \dots & 0 & \beta_{K-1} & \alpha_{K-1} \end{pmatrix} \tag{5.27}$$

where K is defined as the Krylov dimension. Furthermore we define the *Krylov space* as the following vector space

$$\mathcal{K}(\hat{H}, \boldsymbol{q}_0) = \text{span}\{\boldsymbol{q}_0, \hat{H}\boldsymbol{q}_0, ..., \hat{H}^{K-1}\boldsymbol{q}_0\} \tag{5.28}$$

To generate the matrix in 5.27, one may either append $\{\beta_i\}_{i=1,2,...,K-1}$ and $\{\alpha_i\}_{i=0,1,...,K-1}$ to the Krylov matrix during the solution of equations 5.23-5.25, or alternatively, first calculate $\{\boldsymbol{q}\}_{i=1,2,...,K-1}$, and then calculate

$$\hat{H}_K = (\boldsymbol{q}_0\boldsymbol{q}_1...\boldsymbol{q}_{K-1})^\dagger \hat{H} (\boldsymbol{q}_0\boldsymbol{q}_1...\boldsymbol{q}_{K-1}) \tag{5.29}$$

After the Krylov matrix is built, a diagonalization in the Krylov space is performed in order to find the ground state. Given the transformation in equation 5.29, one may deduce the transformation of vectors in one basis to the other. Denote for instance the ground state eigenvector of $\hat{H}_K$ by $\boldsymbol{\xi}$. Then, the corresponding eigenstate of $\hat{H}$ is

$$\boldsymbol{\Psi} = \sum_{i=1}^{K-1} \xi_i \boldsymbol{q}_{i-1} \tag{5.30}$$

where ξ_i are the components of the ground state of $\hat{H}_K$. The vast reduction of matrix dimension lends itself to the fact that iterations of the type $\hat{H}^N\boldsymbol{q}$ converges towards the eigenstates belonging to eigenvalues of large magnitudes. In order to explain this, consider writing the initial random vector as a linear combination of the eigenstates of $\hat{H}$

$$\boldsymbol{q}_0 = \sum_n c_n \boldsymbol{\lambda_n} \tag{5.31}$$

where c_n are complex coefficients and $\boldsymbol{\lambda_n}$ are the eigenstates of $\hat{H}$. Now, upon acting with $\hat{H}$ N times, we obtain

$$\hat{H}^N \boldsymbol{q}_0 = \sum_n c_n E_n^N \boldsymbol{\lambda_n} \tag{5.32}$$

since $\hat{H}\,|n\rangle = E_n\,|n\rangle$. It is clear that the dominant contribution in the linear combination of equation 5.32 comes from the state for which $|E_n|$ is largest. Therefore, we can construct a basis out of the Krylov space, equation 5.28. One may question the utility of such a method applied to a Hamiltonian for which the actual ground state belongs to

the energy of smallest magnitude. In that case, the following restatement of equation 5.32 can be devised

$$(\hat{H} - \sigma)^N \boldsymbol{q}_0 = \sum_n c_n (E_n - \sigma)^N \boldsymbol{\lambda_n} \tag{5.33}$$

where σ is some real parameter chosen in order to select out the ground state of $\hat{H}$.

5.3 The Arnoldi-Lanczos propagator

Given the tools necessary to calculate the time independent problem, we now proceed to propagate the system in time. The problem at hand is reiterated from equation **??**, which is solved along with equation 3.48. The mathematical problem can be formulated as

$$\begin{aligned} \boldsymbol{\Psi}(t) &= \hat{T} e^{-i \int_0^t \hat{H}(\bar{t}) d\bar{t}} \boldsymbol{\Psi}(0) \\ &= \hat{U}(t, 0) \boldsymbol{\Psi}(0) \end{aligned} \tag{5.34}$$

where $\hat{T}$ is the time ordering operator. At small time increments, one may express

$$\boldsymbol{\Psi}(t + \Delta t) \simeq e^{-i \int_t^{t+\Delta t} \hat{H}(\bar{t}) d\bar{t}} \boldsymbol{\Psi}(t) \tag{5.35}$$

at which point various approximations can be applied. The small time step can for instance be used to assume a constant Hamiltonian over the time interval $[t, t + \Delta t]$. A convenient approximation at this point is the Simpson's method, which applied to the integral in equation 5.35 gives

$$\int_t^{t+\Delta t} \hat{H}(\bar{t}) d\bar{t} \approx \frac{\Delta t}{6} [\hat{H}(t) + 4\hat{H}(t + \frac{\Delta t}{2}) + \hat{H}(t + \Delta t)] := \hat{\bar{H}}(t, \Delta t) \tag{5.36}$$

In order to make the many-body Hamiltonian 3.48 tractable for the time propagation, the Krylov subspace reduction of the previous chapter is applied to $\hat{\bar{H}}(t)$ in each time step. [46] Specifically, creating an orthonormal basis in the Krylov space from $\hat{\bar{H}}(t)$ along with the start vector $\boldsymbol{q}_0 = \boldsymbol{\Psi}(t)$, and transforming $\hat{\bar{H}}(t)$ to the Krylov space by means of equation 5.27 can be used to re-express equation 5.35 in the Krylov space as follows

$$\boldsymbol{\Psi}(t + \Delta t)_K = e^{-i \hat{\bar{H}}_K(t, \Delta t)} \boldsymbol{\Psi}(t)_K \tag{5.37}$$

where the state vectors are represented in the Krylov space. Now since $K \ll \dim(\hat{H})$, $\hat{\bar{H}}_K$ can easily be diagonalized, i.e.,

$$\hat{\bar{H}}_K = \hat{S} \hat{D} \hat{S}^{-1} \tag{5.38}$$

where $\hat{S}$ is the matrix of eigenvectors of $\hat{\bar{H}}_K$ and $\hat{D}$ a diagonal matrix of the eigenvalues of $\hat{\bar{H}}$. From this, equation 5.37 can be expressed as

$$\boldsymbol{\Psi}(t + \Delta t)_K = \hat{S} e^{-i \hat{D}} \hat{S}^{-1} \boldsymbol{\Psi}(t)_K := \boldsymbol{\xi} \tag{5.39}$$

Finally, in the same manner as the time independent Lanczos algorithm, the state in equation 5.34 is obtained via

$$\boldsymbol{\Psi}(t + \Delta t) = \sum_{i=1}^{K-1} \xi_i \boldsymbol{q}_{i-1} \tag{5.40}$$

Chapter 6

Results and Discussion

The Hubbard Hamiltonian presented in equation 3.48 is solved with the Arnoldi-Lanczos time propagator for 12 sites. Typical parameters used throughout this section is the hopping term, $t_0 = 0.191$ [a.u.], and the electron-electron repulsion energy, U, expressed in units of t_0. Furthermore, the lattice constant is set to $a = 7.1739$ [a.u.] throughout. The parameters are chosen to mimic Sr_2CuO_3. [21]

For the purpose of generating high harmonic radiation, a $\cos^2$ enveloped pulse is employed, given as

$$A(t) = \frac{E_0}{\omega_0} \sin\Big(\omega_0(t-\bar{t}) + \phi - \frac{\pi}{2}\Big) \cos^2\Big(\frac{\omega_0(t-\bar{t})}{2M}\Big) \\ \dots \{\theta((t-\bar{t}) - \frac{MT}{2}) - \theta((t-\bar{t}) + \frac{MT}{2})\} \tag{6.1}$$

with E_0 the peak electric field strength, ω_0 the carrier angular frequency, M the number of optical cycles, T the period of one cycle of the pulse, $\bar{t}$ the middle of the time interval, ϕ the carrier-envelope phase and θ is the heaviside step function. $\phi = 0$ in all forthcoming simulations. A ten cycle pulse with a cycle duration of 1257 [a.u.] will be used throughout unless stated otherwise. The vector potential is shown in figure 6.1, and is normalized to unity. Herein, a field strength of $E_0 = 0.0019$ [a.u.] and a carrier frequency of $\omega_0 = 0.005$ [a.u.] will be used for the majority of the figures. The macroscopic current from equation 3.55 forms the centerpiece of the subsequent analyses. A theoretical prerequisite to understanding how the current relates to the emission of radiation is the concept of the radiating charge. The power radiated by a moving charge is calculated through the Larmor formula. [25] [8] More specifically, it is the acceleration of the charge that is used in order to calculate the harmonic intensity. Since the current in equation 3.55 is proportional to the speed of the particles, the dipole acceleration can be identified as the time derivative of the current. More precisely, the objective is to calculate [1]

$$a(t) = \frac{d}{dt} J(t) \tag{6.2}$$

where $J(t)$ is understood as the expectation value of the current operator at time t. a(t) will be referred to as the dipole acceleration. As a word of warning, the dipole acceleration can give rise to numerical noise as a result of not vanishing smoothly at the start and end of the pulse. [8] In order to resolve this issue, a window function is applied to $a(t)$. An example of such a window would be to multiply $a(t)$ by the pulse

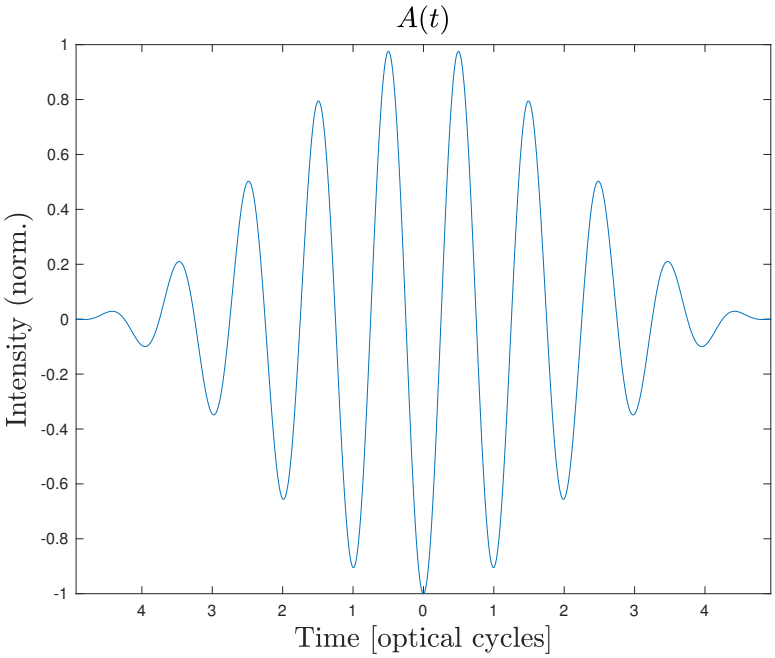

Figure 6.1: Vector potential, $A(t)$, expressed as a function of optical cycles. The intensity is normalized to unity in this figure.

envelope. Rather, the same approach as that used in reference [8] is used here, where the window function is defined as

$$\xi_\epsilon(t) = \begin{cases} 0 & \text{if } t < t_0 \text{ or } t > t_1 \\ \sin^2(\frac{\pi(t-t_0)}{2\epsilon}) & \text{if } t > t_0 \text{ and } t < \tilde{t}_0 \\ 1 & \text{if} t > \tilde{t}_0 \text{ and } t < \tilde{t}_1 \\ \sin^2(\frac{\pi(t_1-t)}{2\epsilon}) & \text{if } t > \tilde{t}_1 \text{ and } t < t_1 \end{cases} \tag{6.3}$$

where t_0 and t_1 mark the start and end of the pulse, respectively. $\tilde{t}_0 := t_0 + \epsilon$ and $\tilde{t}_1 := t_1 - \epsilon$ are defined with some ϵ with the duration of a few femtoseconds. Given a pulse duration of 300 fs, a value of $\epsilon \sim 30$fs or less gives desired results. [1]

In order to resolve the emission of radiation in the frequency domain, the absolute value squared of the Fourier transform is calculated

$$I_{\text{rad}}(\omega) = \left| \int_{t_0}^{t_1} \xi_\epsilon(t) a(t) e^{i\omega t} dt \right|^2 \approx |i\omega J(\omega)|^2 \tag{6.4}$$

where equation 6.2 was used in the approximation. The approximate result is due to the incorporation of the window function, equation 6.3.

[1] This is a point that is perhaps best exemplified by calculating the HHG spectrum with and without the window. The most prominent characteristic of the latter is that it often exhibits noisy harmonics at low frequencies.

6.1 Benchmark

To start off the analysis of the developed numerical code, a benchmark is in place to ensure the correctness of our results. In the spirit of making the problem numerically tractable, some notable approximations are employed. It is unknown from the article in reference [1] which time propagator is used, and moreover which time step is needed to ensure the desired results. According to Nyquist's theorem, the sampling rate of the time interval over which the propagation is performed gives an estimate for the highest discernable frequency component present in our calculated current. However, even if the simulation is performed within the confines of the resulting frequency, the convergence of the wave function at arbitrary times is not assured. Figure 6.2 shows a comparison between original data from R.E.F. Silva *et al.*, and my data. Two values of $\frac{U}{t}$ are shown, and the overall shape fits well. The fine structure of the harmonics is not a perfect match, but is likely considered to have origin in different numerical methods. However, a good quantitative agreement on the basis of two vastly differing interaction strengths indicates that our numerical code can be applied to study other properties, and even go beyond the results of R.E.F. Silva *et al.*

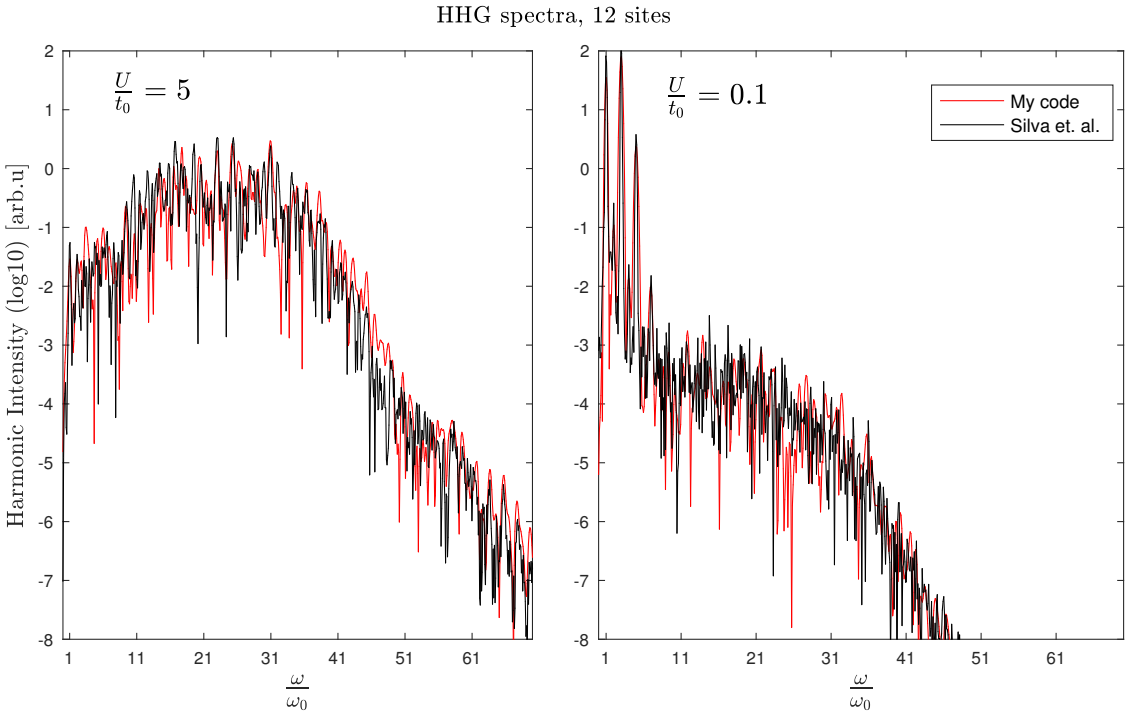

Figure 6.2: A comparison of data from [1] and data from my own code applied to a case of strong correlation (left panel) and to a case of weak correlation (right panel).

The HHG spectra resulting from three different interaction strengths are compared in figure 6.3. We have included the zero U case in order to demonstrate the limit of zero interaction in our numerical code. In this case, the spectrum in figure 4.3 is essentially reproduced. To draw attention to the case of strongest coupling, $\frac{U}{t_0} = 5$, the harmonic yield is centered at $\frac{\omega}{\omega_0} \approx 20$. At the same time, note that since $\omega_0 = 0.005$ [a.u.] and $U = 0.0956$ [a.u.], we have that $U \approx 20\omega_0$. Since this energy coincides with the value of ω for which the yield is highest in figure 6.3, we may attribute the region of highest yield

to transitions between the Hubbard bands - seeing as they have an energy separation of U at direct momentum transitions. (See chapter 3) Therefore, as is probably expected, the harmonic spectrum is indicative of the underlying electronic structure. This hypothesis is further corroborated for the case of $\frac{U}{t} = 2$ which gives a peak at $\frac{\omega}{\omega_0} \approx 8$. Based on the interaction strengths in figure 6.3, the region of highest yield seems to follow a scaling of $N \sim \frac{U}{\omega_0}$ where N is the harmonic order. Low order harmonics are more prominent in the realm of low U, whereas high order harmonics become increasingly apparent at high U. The extreme of zero U has already been demonstrated to give clear low order harmonics in chapter 4.1, and is replicated by our developed numerical algorithm in figure 6.3.

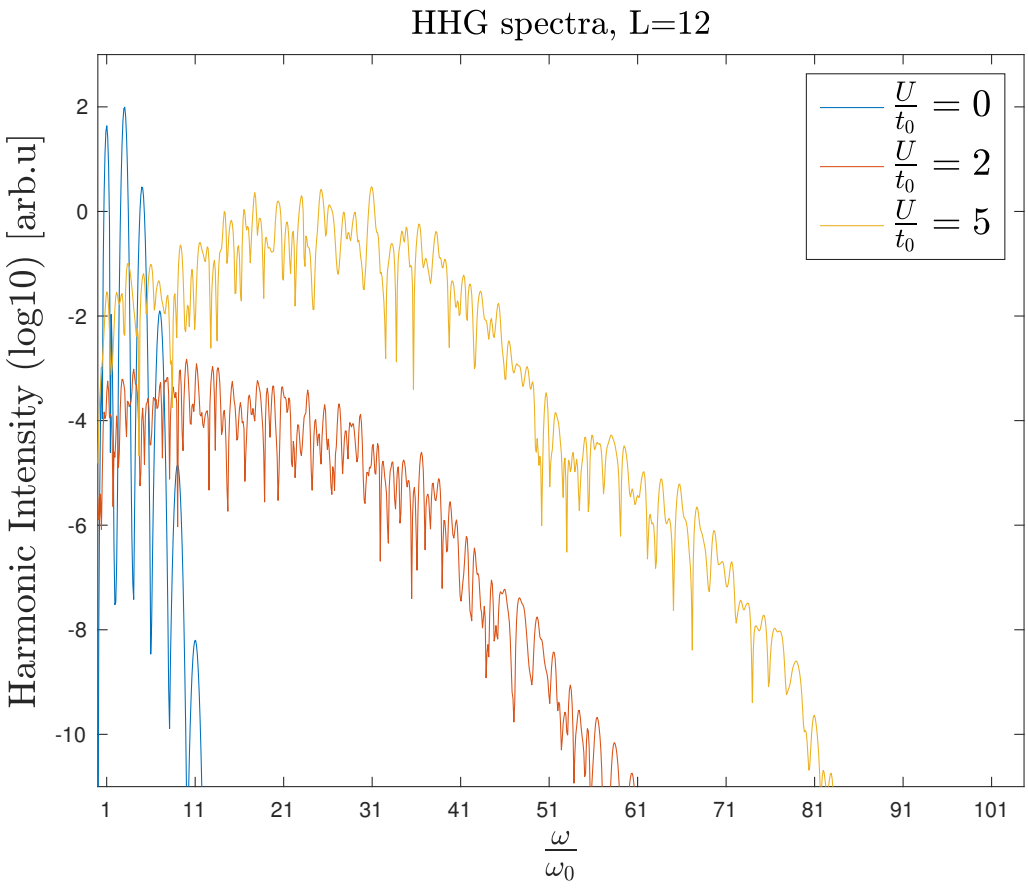

Figure 6.3: HHG spectra for 12 sites with parameters $\frac{U}{t} = 0$, and 2 and 5. The two last cases display an irregular structure which is not manifested in single active electron theories. See for instance [40].

6.2 Time frequency analysis

The HHG spectra depicted in figures 6.2 and 6.3 will in an experimental setting correspond to the yield of the total radiation that hits a detector during the duration of the pulse. However, experiments currently enable the resolution of emitted harmonics to the precision of 1-2 femtoseconds (fs) in the time domain. [47] Thus, with the certainty that this time scale is within experimental bounds, one may proceed by performing a time-frequency analysis with fs windows. Theoretically, a time frequency analysis is performed by multiplying the dipole acceleration, a(t) in equation 6.2, by a narrow Gaussian function with FWHM (full width at half maximum) on the order of a few fs. These functions are referred to as *sliding windows*. More specifically, the same sliding window as used in [1] is used here, and is of the form $\exp\left[-\frac{(t-\tau)^2}{\sigma^2}\right]$, where $\sigma = \frac{1}{3\omega_0}$ and τ marks the time at which the harmonics is detected. Figure 6.4 shows such a time-resolved harmonic emission. In figure 6.4 an interesting correlation between the onset of emitted radiation with the time the pulse attains the threshold field strength, F_{th}, is observed. Roughly speaking, the threshold field strength is attained at the instances of increased harmonic emission in the middle and the lower panel of figure 6.4. [1] We restate equation 1.3 from the introduction here

$$F_{th} = \frac{\Delta}{2e\xi} \tag{6.5}$$

where again Δ is the optical gap and ξ the correlation length of a doublon hole pair. It was mentioned that Δ scales linearly with U. In comparing the middle panel with the bottom panel, it is seen that the onset of high harmonic radiation for $\frac{U}{t_0} = 5$ happens at a later time than for the case of $\frac{U}{t_0} = 2$. This is because for stronger correlation, the time taken for the field to reach threshold field strength is prolonged in light of equation 6.17. It should be emphasized that each of the figures 6.2 and 6.3 are essentially comprised of sums of the time slices used in order to calculate the time-frequency spectrogram in figure 6.4. With the attosecond metrology that is currently achievable, there is a promising prospect of using analyses of the likes of that in 6.4 to gain useful information about the behavior of strongly correlated systems on the attosecond time scale. This is the main finding purported in the recent paper of R.E.F. Silva *et al.* [1]

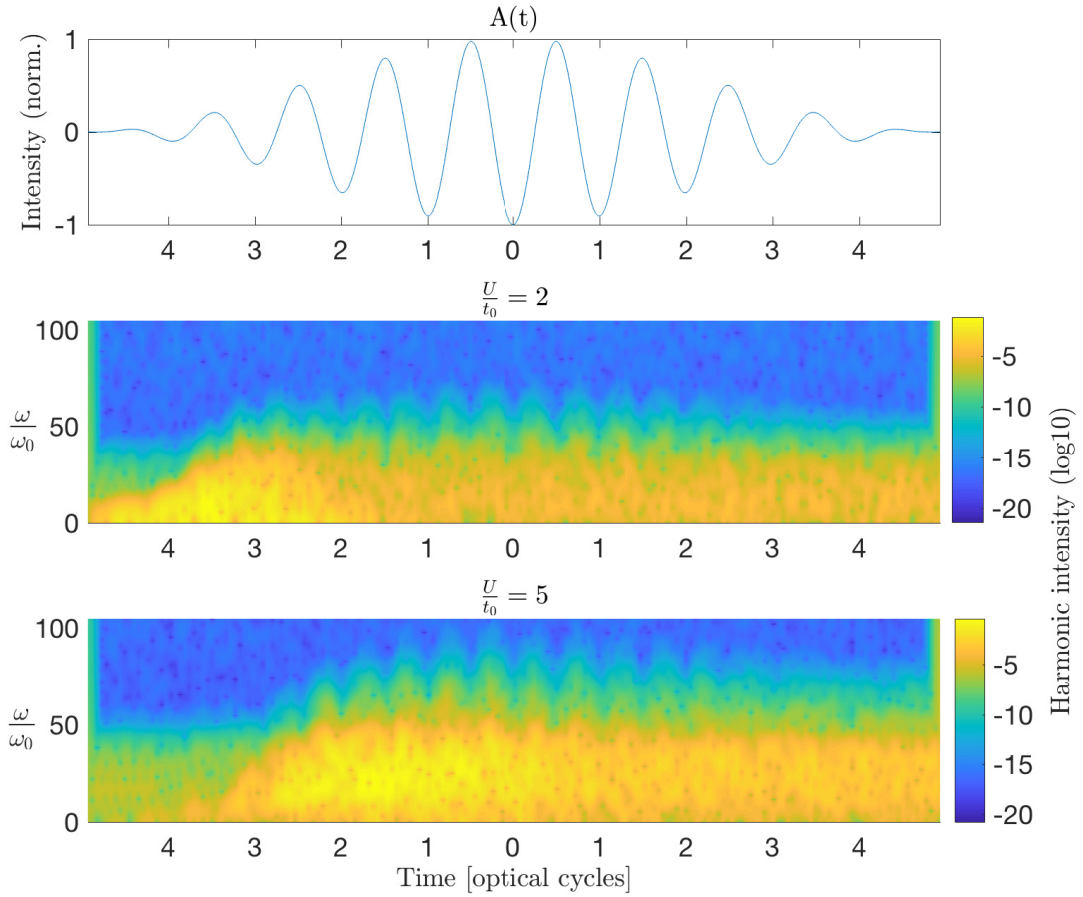

Figure 6.4: In the top panel, the vector potential is plotted as a function of time, and is normalized to unity. The middle panel shows a time frequency analysis for the case $\frac{U}{t} = 2$. The bottom panel shows the case of $\frac{U}{t} = 5$. Time frequency analysis is performed on the generated dipole accelerations, with a sliding window as in [1]. The color plot is drawn on a logarithmic scale. Along the x-axis in the two lower panels, the angular frequency of the emitted harmonics is given in units of the angular frequency of the driving field. In comparison with the publication, smaller intensities are here highlighted in places where the authors in [1] have chosen to remove the coloring.

Excited states in the Hubbard model are characterized by the population of the upper Hubbard band [34] - i.e., doubly occupied sites. Clearly, the excitation process depends on the coupling strength, U. Figure 6.5 shows the projection of the wave function at time t onto the ground state. Explicitly, the projection is defined as $W(t) = |\langle\Psi_0|\Psi(t)\rangle|^2$, where $|\Psi(t)\rangle$ is the propagated wave function and $|\Psi_0\rangle$ the ground state. Now, since figure 6.5 draws a comparison on the grounds of different coupling strengths only, it is seen that the same field strength will more efficiently expedite the excitation process in $\frac{U}{t} = 2$ as compared to $\frac{U}{t} = 5$. This is because the energy gap from the ground state to the first excited state is lower in the former case. Moreover, the middle and the bottom panels of figure 6.5 both display time intervals of coherence between the ground state and first excited state. Most importantly, the coherence in the described time intervals are accompanied by increased harmonic emission, as can be seen from figure 6.4. The

described events substantiate the importance of coherence in the process of HHG in strongly correlated systems.

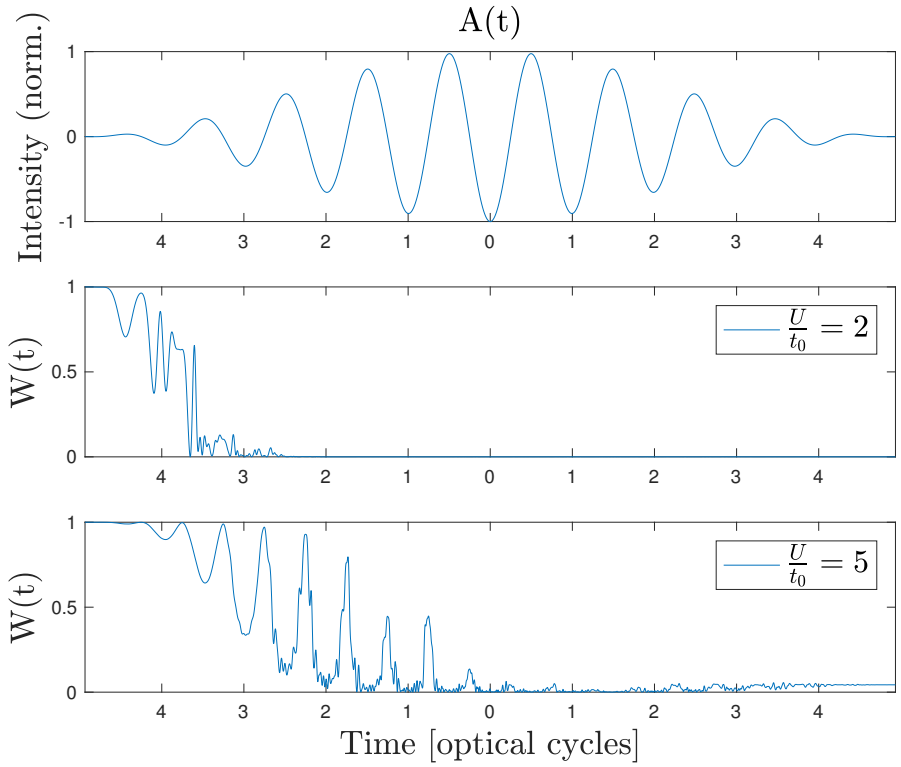

Figure 6.5: Top panel: Vector potential normalized to unity and otherwise conforming to the pulse parameters already stated. Middle panel: Ground state projection for 12 sites with $\frac{U}{t} = 2$. Bottom panel: The same system with $\frac{U}{t} = 5$.

6.3 Phase transitions

It will be the objective of this section to demonstrate that the already presented results show signatures of an insulator to metal phase transition. Generally, correlation functions are a way to properly ascertain the fact of a phase transition taking place. The relevant correlation functions undergo a sudden change during this event, and the key quantities are presented here. Firstly, note that in a highly correlated Hubbard model, the lowest energy eigenstates will tend to have the spins aligned in an anti-ferromagnetic fashion. [34] This configuration is characterized as a state with high *anti-ferromagnetic order*. In the other limit of weak correlation, there is less restriction on the ordering and states with doubly occupied sites can easily occur. A key remark is that we may attribute the scenario of high anti-ferromagnetic ordering to the insulating phase, and the scenario of low anti ferromagnetic ordering (and similarly the preponderance of doubly occupied sites) to a metallic phase. Both described characteristics can be quantified through the doublon correlation function

$$D(t) = \frac{1}{L} \left\langle \sum_{j=1}^{L} \hat{n}_{j,\uparrow} \hat{n}_{j,\downarrow} \right\rangle (t) \tag{6.6}$$

and the spin-spin correlation function [48]

$$\eta(t) = \frac{1}{L}\left\langle \sum_{j=1}^{L} \hat{\boldsymbol{S}}_j \hat{\boldsymbol{S}}_{j+1} \right\rangle (t) \tag{6.7}$$

where L is the number of sites in the system, and $\langle \ldots \rangle (t)$ is understood as $\langle \Psi(t)| \ldots |\Psi(t)\rangle$ for the state of the system, $|\Psi(t)\rangle$, at time t. D(t) is the number of doubly occupied sites normalized over system size, whereas η is a quantity measuring the degree to which the spins in the lattice are aligned anti-parallel. Furthermore,

$$\hat{\boldsymbol{S}}_i = \frac{1}{2} \sum_{\alpha=\uparrow,\downarrow} \sum_{\beta=\uparrow,\downarrow} \hat{c}^{\dagger}_{i,\alpha} \boldsymbol{\sigma}^{\alpha,\beta} \hat{c}_{i,\beta} \tag{6.8}$$

where

$$\sigma_x = \begin{pmatrix} 0 & 1 \\ 1 & 0 \end{pmatrix}, \sigma_y = \begin{pmatrix} 0 & -i \\ i & 0 \end{pmatrix}, \sigma_z = \begin{pmatrix} 1 & 0 \\ 0 & -1 \end{pmatrix}$$

are the Pauli matrices. [31] It can be shown that

$$\hat{\boldsymbol{S}}_i \hat{\boldsymbol{S}}_j = \frac{1}{2}(\hat{S}^+_i \hat{S}^-_j + \hat{S}^-_i \hat{S}^+_j) + \hat{S}^z_i \hat{S}^z_j \tag{6.10}$$

where

$$\hat{S}^+_i = \hat{S}^x_i + i\hat{S}^y_i = \hat{c}^{\dagger}_{i,\uparrow} \hat{c}_{i,\downarrow} \tag{6.11}$$

and

$$\hat{S}^-_i = \hat{S}^x_i - i\hat{S}^y_i = \hat{c}^{\dagger}_{i,\downarrow} \hat{c}_{i,\uparrow} \tag{6.12}$$

For the last term in equation 6.10 we have

$$\hat{S}^z_i = \frac{1}{2}(\hat{n}_{i,\uparrow} - \hat{n}_{i,\downarrow}) \tag{6.13}$$

From a numerical point of view, the above definitions present intricate combinations of creation and annihilation operators, and it may hence be instructive to demonstrate how this acts on a many body state following the methods of chapter 5. A general basis element is reiterated here as

$$|\phi_m\rangle = [\hat{c}^{\dagger}_{m_1,\downarrow} \hat{c}^{\dagger}_{m_2,\downarrow} \ldots \hat{c}^{\dagger}_{m_{\frac{L}{2}},\downarrow}][\hat{c}^{\dagger}_{\overline{m}_1,\uparrow} \hat{c}^{\dagger}_{\overline{m}_2,\uparrow} \ldots \hat{c}^{\dagger}_{\overline{m}_{\frac{L}{2}},\uparrow}] \,|\rangle = \left|\phi_{\downarrow}\right\rangle \left|\phi_{\uparrow}\right\rangle \tag{6.14}$$

It is seen that

$$\hat{S}^+_i \hat{S}^-_j \,|\phi_m\rangle = \hat{c}_{i,\downarrow} \hat{c}^{\dagger}_{j,\downarrow} \left|\phi_{m,\downarrow}\right\rangle \hat{c}^{\dagger}_{i,\uparrow} \hat{c}_{j,\uparrow} \left|\phi_{m,\uparrow}\right\rangle \tag{6.15}$$

Furthermore,

$$\begin{aligned} \hat{c}_{i,\downarrow} \hat{c}^{\dagger}_{j,\downarrow} \left|\phi_{m,\downarrow}\right\rangle &= \hat{c}_{i,\downarrow} \hat{c}^{\dagger}_{j,\downarrow} [\hat{c}^{\dagger}_{m_1,\downarrow} \hat{c}^{\dagger}_{m_2,\downarrow} \ldots \hat{c}^{\dagger}_{m_{\frac{L}{2}},\downarrow}] \,|\rangle \\ &= -[\underbrace{\hat{c}^{\dagger}_{m_1,\downarrow} \hat{c}^{\dagger}_{m_2,\downarrow} \ldots \hat{c}^{\dagger}_{m_l,\downarrow}}_{2l \text{ fermion exchanges}} \hat{c}^{\dagger}_{j,\downarrow} \hat{c}_{i,\downarrow} \ldots \hat{c}^{\dagger}_{m_{\frac{L}{2}},\downarrow}] \,|\rangle \end{aligned} \tag{6.16}$$

A similar procedure is conducted on the spin up sector in equation 6.15

$$\hat{c}_{i,\uparrow}\hat{c}^{\dagger}_{j,\uparrow}\left|\phi_{m,\uparrow}\right\rangle = [\underbrace{\hat{c}^{\dagger}_{\overline{m}_1,\uparrow}\hat{c}^{\dagger}_{\overline{m}_2,\uparrow}\ldots\hat{c}^{\dagger}_{\overline{m}_l,\uparrow}}_{2l \text{ fermion exchanges}}\hat{c}^{\dagger}_{j,\uparrow}\hat{c}^{\dagger}_{i,\uparrow}\ldots\hat{c}^{\dagger}_{\overline{m}_{\frac{L}{2}},\uparrow}]\,|\rangle \tag{6.17}$$

whence we see from equations 6.16 and 6.17 that the result of the first term in equation 6.10 acting on a basis state gives rise to an overall minus sign. The action of the second term in equation 6.10 is completely analogous, whereas the action of the last term essentially amounts to the same algorithm as that in equation 5.9.

Figure 6.6 shows the behavior of the correlation functions in equations 6.6 and 6.7 over the duration of the laser pulse. The negative of η is plotted for the purpose of clearly discerning the two functions. For $\frac{U}{t} = 5$ in the bottom panel of figure 6.6, a prolonged period of a low value of $D(t)$ (and a high value of $-\eta(t)$) can be seen before the field reaches the threshold field strength, F_{th}. The case of $\frac{U}{t} = 2$ in the middle panel of figure 6.6 shows that the ground state depletion in the middle panel of figure 6.5 happens in line with the decrease of anti-ferromagnetic order and the increase in doublon-hole pairs. That is, the depletion of the ground state marks the change in the defined correlation functions, and hence marks the onset of the phase transition. The same reasoning applies equally well to the instance of $\frac{U}{t_0} = 5$. It can also be seen that the change in the correlation functions directly reflects the high harmonic emission events in figure 6.4. Hence, in summarizing the observations from figures 6.4-6.6 we have studied the insulator to metal phase transition from the vantage points of time resolved HHG, ground state projection and correlation functions in time.

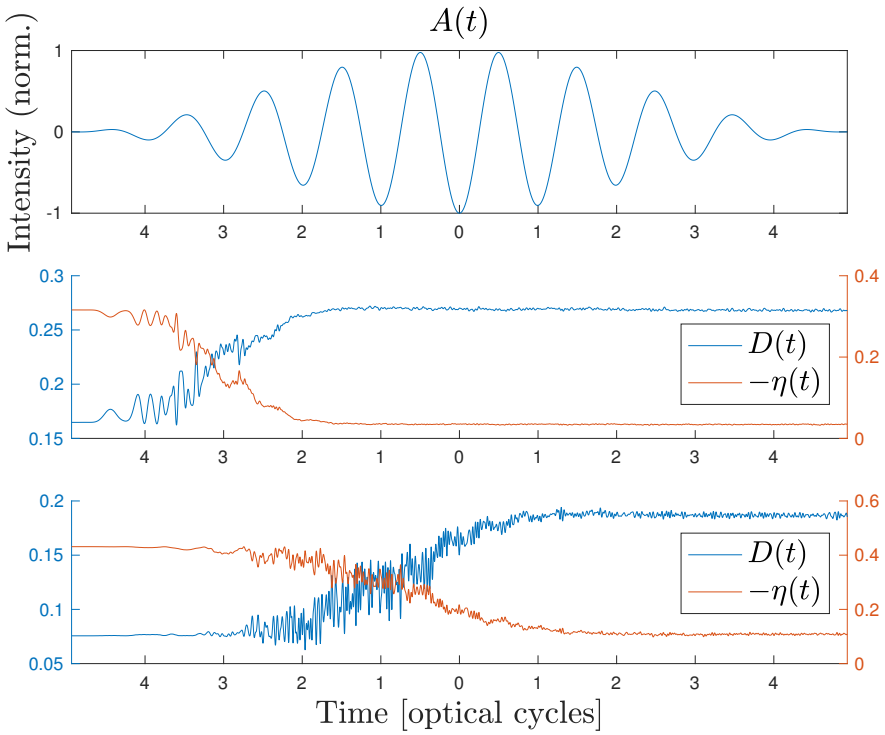

Figure 6.6: The indicator of a phase transition - the correlation functions in equations 6.6 and 6.7 shown for $\frac{U}{t_0} = 2$ in the middle panel and $\frac{U}{t_0} = 5$ in the bottom panel.

6.4 Different system sizes

Given the computational complexity outlined in the chapter on numerical methods, it is natural to inquire why 12 sites are needed. One can argue on the basis of convergence. That is, a sample of simulations across many system sizes is gathered and one concludes that for instance the discrepancy from L=6 to L=8 is larger than that between L=10 and L=12. R.E.F. Silva *et al.* has reported essentially similar results for L=12 and L=14 as a justification for presenting results for L=12. [1] A systematic account for the trend from L=6 to L=12 for the instance of the doublon correlation function is presented in the following.

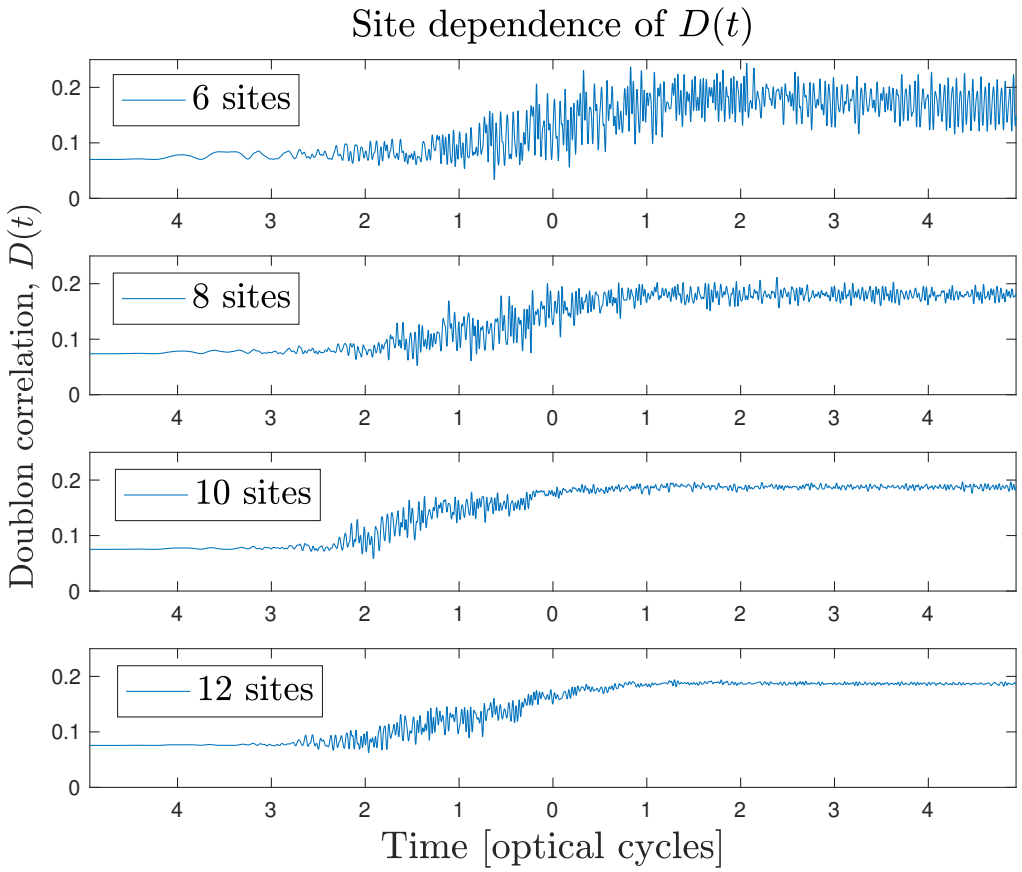

Figure 6.7: The doublon correlation function from equation 6.6 is presented in varying system sizes. All panels are results of simulations performed with $\frac{U}{t_0} = 5$.

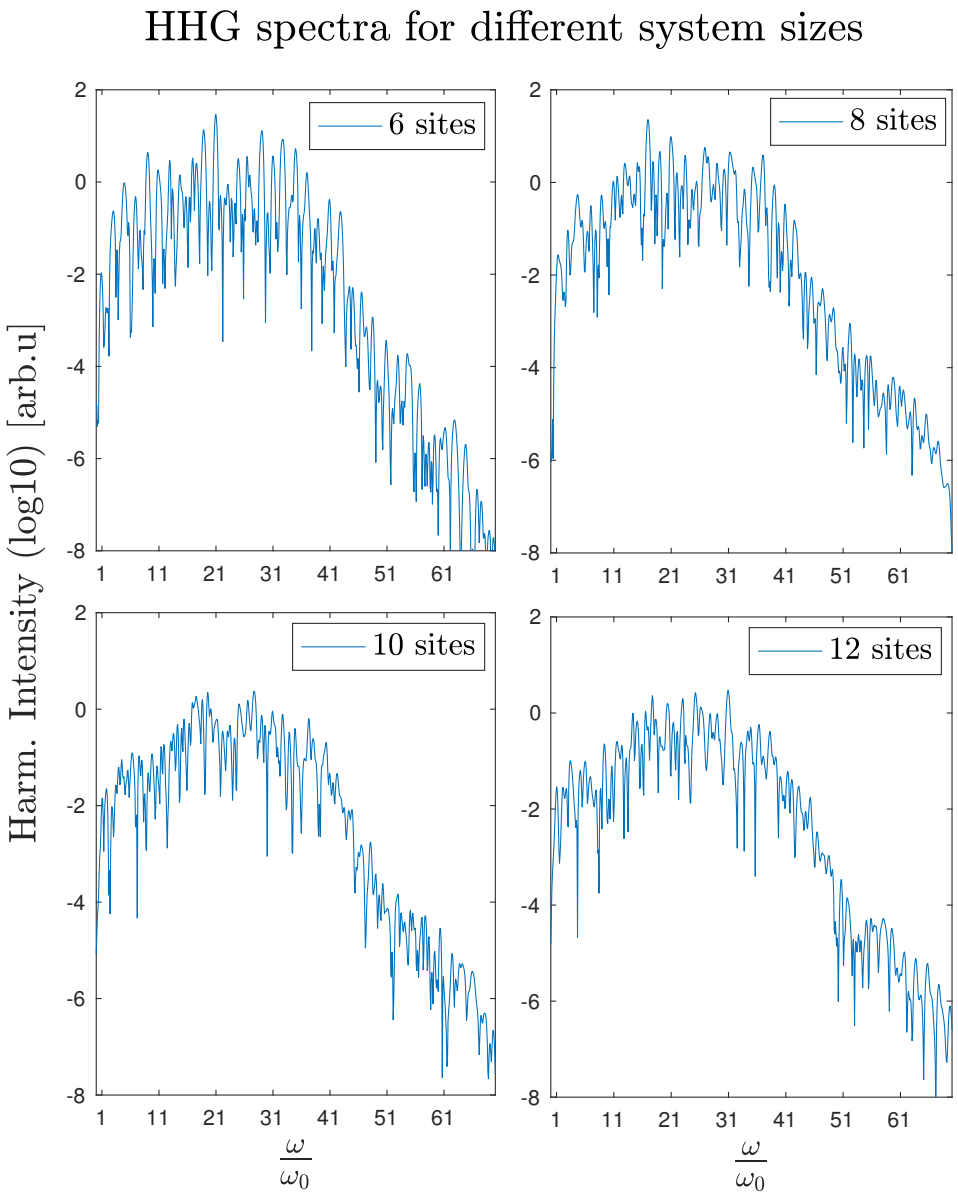

Figure 6.8: Comparison of HHG spectra for different system sizes. All panels are results of simulations performed with $\frac{U}{t_0} = 5$.

In 6.7, it is seen that the simulations with fewer sites are characterized by an oscillatory behavior after the phase transition has taken place. In order to explain this, recall the interpretation of the doublon-correlation function as the number of doubly occupied sites normalized over system volume. Now, when the system is comprised of few sites and few electrons, $D(t)$ in equation 6.6 will respond more sensitively to an event where a single particle jumps to a site where an electron with opposite spin already resides. With this interpretation in mind, we may conjecture that regions prior to, and after the phase transition, in figure 6.7 will become almost entirely flat when the system size increases further. On account of this, we may judge the case of 10 and 12 sites to be an adequate representation of the true physical scenario.

Interestingly, the HHG spectra resulting from different system sizes presented in

figure 6.8 are harder to discern between. As mentioned, the HHG spectrum in the presented coupling regime bears the characteristic of the single particle excitation energy, U. (see chapter 3) In this regard, the overall shape of the spectra is more a statement about the single particle energies - which is more or less site independent. Although considerable discrepancy across the panels in figure 6.7 has been demonstrated, this is arguably not paralleled in figure 6.8.

6.5 Dependence on field strength

Since much attention has been given the details of the phase transition, this section will provide an insight into the system properties at field strengths below F_{th}. This marks the first mention of an "ordinary" HHG-processes in the Hubbard model in this thesis. For a laser pulse that exceeds the threshold field strength at some point during the pulse, the resulting spectrum is independent of intensity. [1] In this section we denote the unit field strength as $E_0 = 0.0019$ [a.u.].

A broad overview of the effect of field strength is shown in figure 6.9 where we compare field strengths above and below F_{th}. For the intensity $E = 0.1E_0$ we see a harmonic spectrum reminiscent of atomic HHG-spectra and those of semiconductor HHG-spectra, the latter of which is usually modeled by a interband and intraband processes including a valence and a conduction band. [5] [22] That is, the signature of dynamical Bloch oscillations is present for the lowest order harmonics for the considered field strength. Furthermore, the spectrum acquires a plateau structure followed by a cut-off around $N \approx 30$. A notable feature of the lowest couple of field strengths in figure 6.9 is the emergence of clean harmonics at all orders, which is reminiscent of single active electron theories in general.

In figure 6.10 we show the spectra for two additional field strengths above and below $E = 0.1E_0$. The field strength of $E = 0.15E_0$ highlights the intermediate regime between the normal HHG process present in the Mott insulator and the regime of above threshold field strength. In particular, the spectrum of $E = 0.15E_0$ displays some of the irregularities seen in the spectrum produced for $E = E_0$. Whereas the case of $E = 0.1E_0$ exhibited a clear plateau structure, this feature seemingly vanishes for $E = 0.15E_0$. However, a cut-off can be seen at $\frac{\omega}{\omega_0} \approx 30$ for both of the aforementioned.

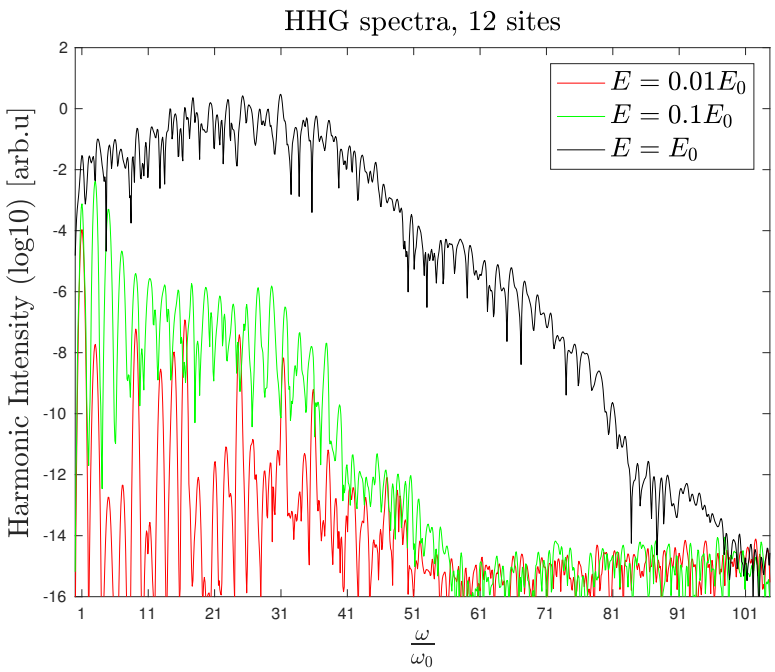

Figure 6.9: The effect of altering the field strength is investigated. $E_0 = 0.0019$ [a.u.] is the field strength for which the spectrum displays above threshold behavior as in figures 6.2-6.8.

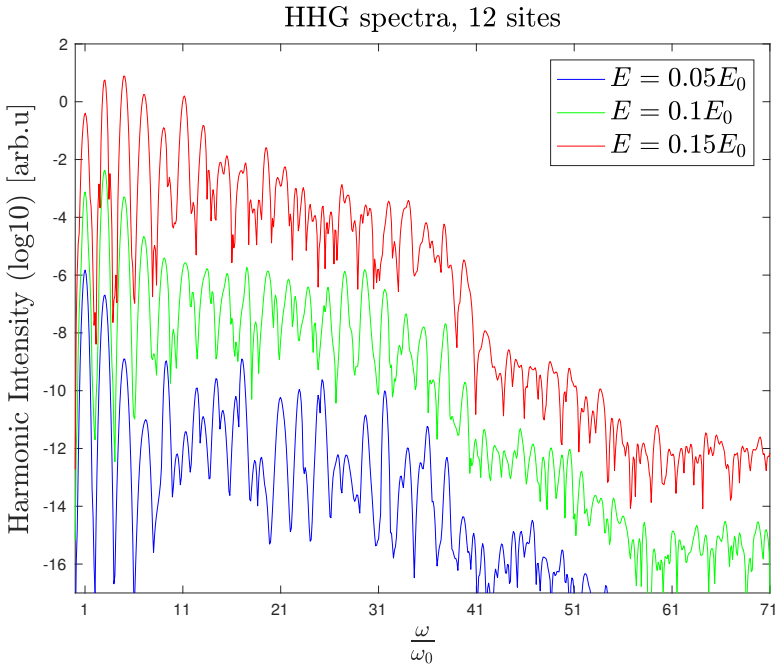

Figure 6.10: Three HHG spectra for intensities around $E = 0.1E_0$ are shown. With respect to the actual intensities, the spectra for $E = 0.05E_0$ and $E = 0.15E_0$ are shifted by -3 orders of magnitude and +3 orders of magnitude, respectively.

6.6 The Mott-Hubbard model

Despite the Hubbard model's neglect of anything other than on-site correlations, the so called Mott-Hubbard model

$$\hat{H} = -t_0 \sum_{\sigma} \sum_{i=1}^{L} (\hat{c}^{\dagger}_{i,\sigma} \hat{c}_{i+1,\sigma} + h.c.) + U \sum_{i=1}^{L} \hat{n}_{i,\uparrow} \hat{n}_{i,\downarrow} + V \sum_{i=1}^{L} \hat{n}_i \hat{n}_{i+1} \tag{6.18}$$

where

$$\hat{n}_i = \hat{n}_{i,\uparrow} + \hat{n}_{i,\downarrow} \tag{6.19}$$

[34] has been applied to study quantum interference effects in the a strongly correlated system as a means of calculating optical conductivity, among other quantities. [49] Recall how the light matter coupling only affects the single particle part of the Hamiltonian in equation 3.17. Hence, the complex phases in the Hamiltonian 3.48 can be added to the Mott-Hubbard Hamiltonian in the same manner as for the Hubbard model. Fortunately, this extension does not pose much of a numerical challenge, since the last term in 6.18 is diagonal in the exact basis. In [49] such a model with parameters $t_0 = 0.0184$ [a.u.], $U = 16.4t_0$ and $V = 2t_0$ is studied. In the following, the Mott-Hubbard model will be solved with this set of parameters with and without the nearest neighbor term, V. The authors in [49] have seen effects of this interaction in terms other properties than HHG, which they explain in terms of quantum path interference.

Figure 6.11 shows a comparison of the HHG-spectra obtained for the above parameters, and the same parameters except for $V = 0$. Incidentally, the energy spectrum of the Hamiltonian 6.18 is such that we make use of equation 5.32 for obtaining the ground state. As in earlier results, the yield is concentrated around $N \approx \frac{U}{\omega_0}$. At this point, a trend in the generated harmonic spectra emerges. Figure 6.11 shows a shift in the maximal yield towards higher energies - directly reflecting the increased electron-electron repulsion. More quantitatively, the orders N are shifted according to $N \approx \frac{U}{\omega}$, as was indicated in the context of figure 6.3. Since figure 6.11 represents a multiphoton process involving extra intermediate states in relation to the other spectra presented herein, the overall yield is lower.

We attribute the heightening of harmonic intensity at orders below $N \approx 60$ to the intermediate energy steps between those of the Hubbard model 3.48. The suppression of harmonic intensity above this order on the other hand, may find a similar explanation to that given by S. Wall *et al.* [49] Quantum interference of different excitation paths will lead to the suppression of certain harmonic intensities, while increasing other ones.

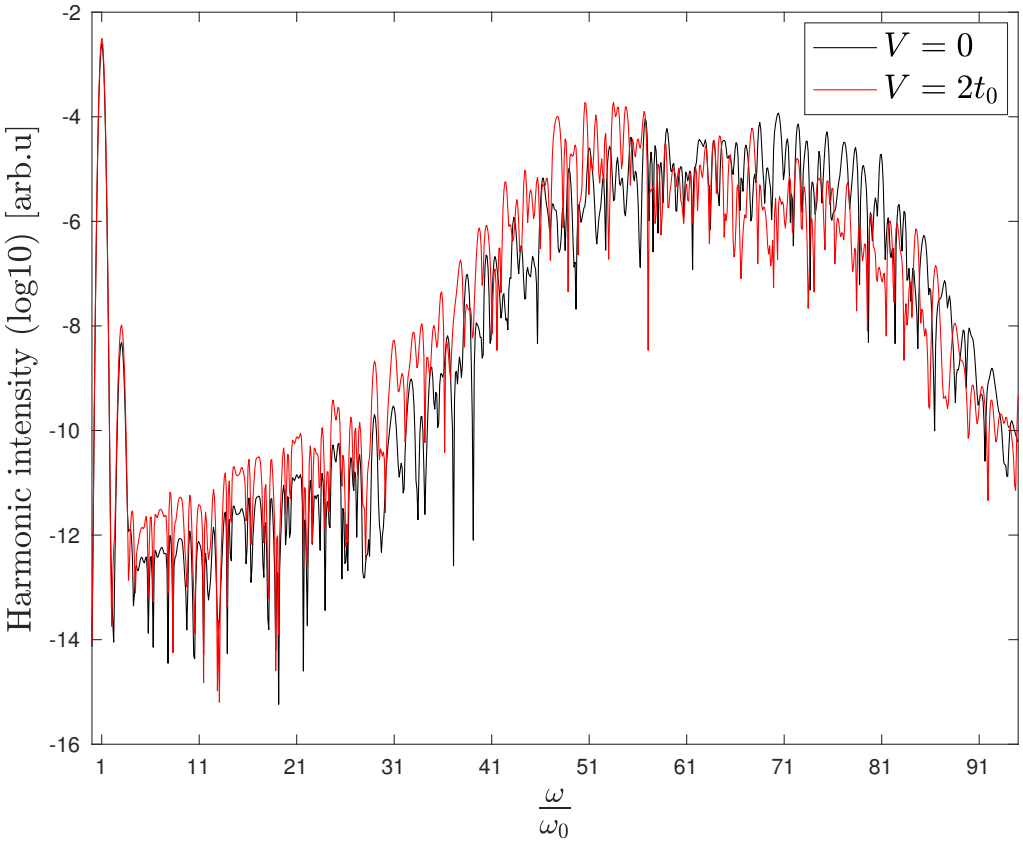

Figure 6.11: The effect of including the nearest neighbor interaction term in the Hubbard model - i.e., going from the model in equation 3.48 to that in equation 6.18.

6.7 Doping

We have in this thesis developed a numerical code capable of investigating the one dimensional Hubbard model in any subspaces of the symmetries of $\hat{S}_z$ and $\hat{N}_e$ explained in chapter 5. Therefore, we seek to explore other configurations than those of singlet states and half filling. In figure 6.12, such a simulation is performed for 10 sites. Despite the fact that all previous results have been calculated for 12 sites, we find that not imposing any $\hat{S}_z$ symmetry increases the computational demand so as to make 12 site simulations unfeasible. Therefore, we present the results for 10 sites instead. Its validity can be justified on the basis of the discussion following figure 6.7. Nevertheless, figure 6.12 forms a valid basis of comparison between different electron fillings. Moreover, it is calculated that simulations with the half-filling configuration gives the same HHG spectrum as that with half-filling *and* restriction to the subspace of $S_z = 0$. Figure 6.12 shows the comparison between a 10 site system with 6,10 and 14 electrons without restricting to any subspace of the S_z symmetry. In drawing attention to the case of $N_e = 6$, we see that the signature of dynamical Bloch oscillations are very much present. Since there are less electrons in the system, there are correspondingly less excitations to the upper Hubbard band. This result goes some way in disentangling the contributions from intra-subband acceleration (the process responsible for dynamical Bloch oscillations) and inter-subband processes. That is, since we *know* that the upper Hubbard band

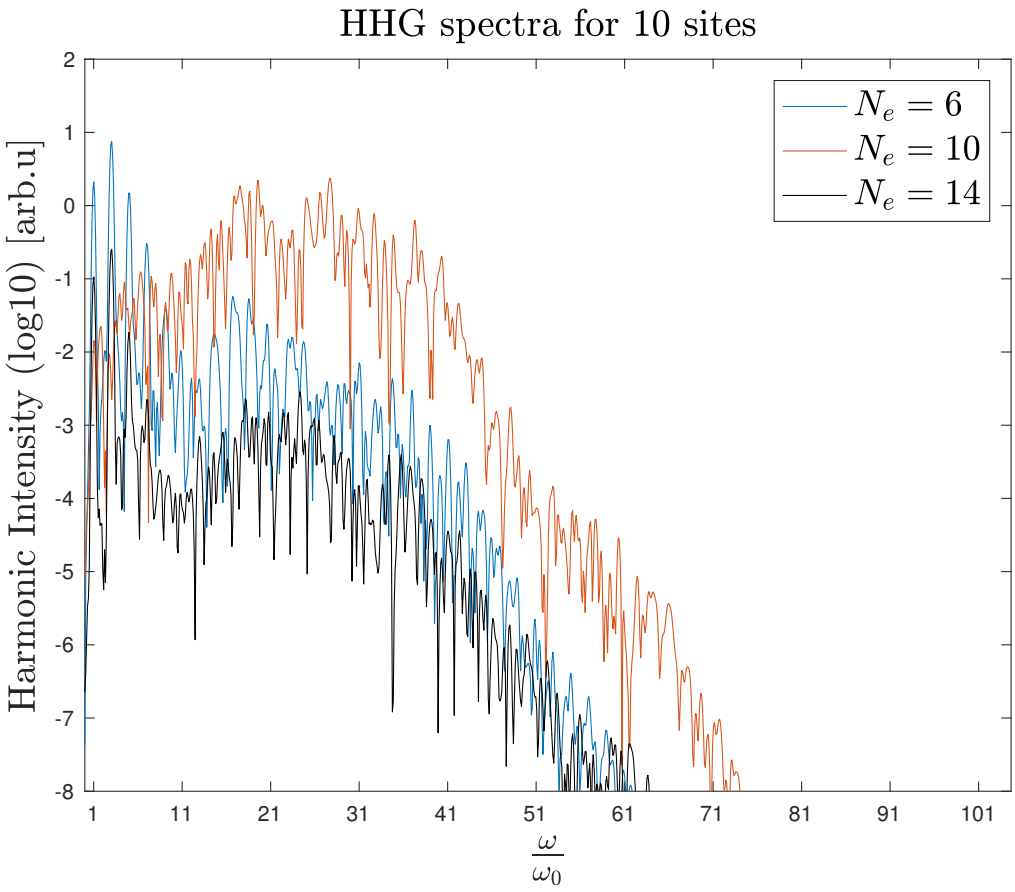

Figure 6.12: This figure displays simulation results from different subspaces of electron number.

is sparsely populated for $N_e = 6$, we can with a great deal of certainty attribute the low harmonic region to that of dynamical Bloch oscillations and the region of higher harmonics to inter-subband processes. In order to explain the case of 14 electrons, the reader is reminded about the interpretation following the Hubbard Hamiltonian, equation 3.17. For high electron fillings, there is a higher probability of an electron being obstructed by another electron already residing on a given site. Correspondingly, the degree to which the electron hops around the crystal lattice is limited. As a result, the dynamical Bloch oscillations are suppressed. Now, since there is less electron motion, this implies that few electrons get promoted to the upper Hubbard band. However, for electron numbers above half-filling some parts of the Hubbard band is naturally populated. Although the cases $N_e = 6$ and $N_e = 14$ presented less interband coherence, the fillings studied in figure 6.12 provides a prospect with regards to tuning the shape of the Harmonic spectrum in a given material on the basis of doping.

Chapter 7

Conclusion

In this thesis, an account for the the dynamics of strongly correlated systems has been provided in light of correlation functions, demonstrations of coherence and most importantly, both total HHG-spectra and time-frequency analyses. The results presented have been sought simplified through the formalism of Hubbard bands. In assessing the robustness of the Hubbard model in this context, equation 3.48, has been examined through comparing with the Mott-Hubbard model, equation 6.18, for parameters used in a recent experiment by S. Wall *et al.* [49] Moreover, HHG spectra for doped materials have been presented as a means of substantiating our hypotheses about the validity of the explanation in terms of Hubbard bands.

Seeing as electronic structure has been key in describing most observed phenomena up until this point, an interesting prospect is to determine in what way the spectrum will change, for any intensity, if another band is included. However, adding bands amounts to building a larger space of configurations - which would for 12 sites *effectively* amount to a 24 site problem, adding the orbital degree of freedom. When a laser pulse attains above threshold field strength, it is questionable whether the single band Hubbard model breaks down.

Among the most notable approximations employed in this thesis is the dipole approximation. For larger system sizes than what has been considered, it is questionable whether the vector potential can be treated as constant over the range of the system considered. It also remains to see whether the conclusions reached here withstands in two dimensional and three dimensional materials. In this regard, we will need to incorporate additional symmetries to those considered here in order to perform realistic simulations.

Based on what has been presented, it will be interesting to further explore the possibility of obtaining equations on closed form through an equation of motion technique. This is in fact what is done in the Semiconductor Bloch Equations, although they rely on the Hartree Fock approximation. [12] Future prospects should include analytical strides in order to mitigate the numerical difficulty inherent in the physics of these systems.

Appendix A

The current operator

The correspondence between the current in momentum space and that in real space, equations 4.4 and 3.55, respectively, is proved in this appendix. By adhering to the conventions

$$\hat{c}_{k,\sigma} = L^{-\frac{1}{2}} \sum_i \hat{c}_{i,\sigma} e^{-ikR_i} \tag{A.1}$$

and

$$\epsilon(k) = L^{-1} \sum_{ij} t_{ij} \cdot e^{ik(R_i - R_j)} \tag{A.2}$$

equation 4.4 may be expressed as

$$\begin{aligned} \hat{J}(t) = \sum_\sigma L^{-2} \sum_k \sum_{ijlm} t_{ij} i(R_i - R_j) e^{ik(R_i - R_j)} e^{i(R_i - R_j)A(t)} \\ \hat{c}^\dagger_{l,\sigma} \hat{c}_{m,\sigma} e^{ik(R_l - R_m)} \end{aligned} \tag{A.3}$$

where

$$\begin{aligned} \frac{\partial}{\partial k}\epsilon(k) &= L^{-1} \sum_{ij} t_{ij} \frac{\partial}{\partial k} e^{ik(R_i - R_j)} e^{i(R_i - R_j)A(t)} \\ &= L^{-1} \sum_{ij} i(R_i - R_j) t_{ij} e^{ik(R_i - R_j)} e^{i(R_i - R_j)A(t)} \end{aligned} \tag{A.4}$$

was used. By using the relation

$$L^{-1} \sum_k e^{ik(R_i - R_j)} = \delta(R_i - R_j) = \delta(i - j) \tag{A.5}$$

since $R_i - R_j = a(i - j)$, equation A.3 may be written as

$$\hat{J}(t) = N^{-1} \sum_\sigma \sum_{ijlm} \delta(i - j + l - m) t_{ij} ia(i - j) e^{ia(i-j)A(t)} \tag{A.6}$$

Now, define $\rho := i - j$ and $\xi := l - m$, and write

$$\begin{aligned} \hat{J}(t) &= N^{-1} \sum_\sigma \sum_{i\rho l\xi} \delta(\rho + \xi) ia\rho t_{i,i-\rho} \hat{c}^\dagger_{l,\sigma} \hat{c}_{l-\xi,\sigma} e^{ia\rho A(t)} \\ &= N^{-1} \sum_\sigma \sum_{i,\rho,l} t_{i,i-\rho} ia\rho e^{ia\rho A(t)} \hat{c}^\dagger_{l,\sigma} \hat{c}_{l+\rho,\sigma} \end{aligned} \tag{A.7}$$

Next, we make use of the fact that the system is translationally invariant, i.e., $t_{i,i-\rho} = t_{-\rho}$. Therefore, equation A.7 can be rewritten as

$$\begin{aligned}\hat{J}(t) &= i \sum_{\sigma} \sum_{l,\rho} t_{-\rho} i a \rho e^{ia\rho A(t)} \hat{c}^{\dagger}_{l,\sigma} \hat{c}_{l+\rho,\sigma} \\ &= +iat_0 \sum_{\sigma} \sum_{l=1}^{L} [e^{iaA(t)} \hat{c}^{\dagger}_{l,\sigma} \hat{c}_{l+1,\sigma} - h.c.]\end{aligned} \tag{A.8}$$

Appendix B

Pseudo-particle band structure

The concept of the pseudo-particle band structure presented in the chapter on the Hubbard model, chapter 3, can provide useful insight into the optical response of strongly correlated systems. It is therefore derived here, with an approach closely following that of Hubbards original article from 1963. [33].

We will denote the retarded (+) and advanced (-) Green's functions by

$$\left\langle\left\langle \hat{c}_{i,\sigma}(t); \hat{c}^{\dagger}_{j,\sigma}(t')\right\rangle\right\rangle^{(\pm)} = \mp i\theta(\pm(t-t'))\left\langle[\hat{c}_{i,\sigma}(t), \hat{c}^{\dagger}_{j,\sigma}(t')]_{\eta}\right\rangle \tag{B.1}$$

where $\theta(t-t')$ is the heaviside step function and $\eta = -1$ for fermions, denoting an anti-commutator. By using the Heisenberg equation

$$\frac{d}{dt}\hat{O} = i\big[\hat{H}, \hat{O}\big], \tag{B.2}$$

it is easy to show that

$$\begin{aligned} & i\frac{d}{dt}\left\langle\left\langle \hat{c}_{i,\sigma}(t); \hat{c}^{\dagger}_{j,\sigma}(t')\right\rangle\right\rangle^{(\pm)} \\ & = \pm\delta(\pm(t-t'))\left\langle[\hat{c}_{i,\sigma}(t), \hat{c}^{\dagger}_{j,\sigma}(t')]_{\eta}\right\rangle + \left\langle\left\langle[\hat{c}_{i,\sigma}(t), \hat{H}]; \hat{c}^{\dagger}_{j,\sigma}(t')\right\rangle\right\rangle^{(\pm)} \end{aligned} \tag{B.3}$$

where

$$\frac{d}{dt}\theta(t-t') = \delta(t-t') \tag{B.4}$$

was used. Hereafter, we will be concerned with the retarded Green's function, and hence we drop the superscript (±) in the Green's function. Using equation B.3 in conjunction with the fact that the correlation functions only depend on (t-t'), we may define

$$\left\langle\left\langle \hat{c}_{i,\sigma}; \hat{c}^{\dagger}_{j,\sigma}\right\rangle\right\rangle_{E} = \int_{-\infty}^{+\infty}\left\langle\left\langle \hat{c}_{i,\sigma}(t); \hat{c}^{\dagger}_{j,\sigma}(0)\right\rangle\right\rangle e^{iEt}dt \tag{B.5}$$

Now, a strategy that is often employed in these kinds of calculations, is to perform a substitution $E \longrightarrow E \pm i\epsilon$ in order to ensure convergence of the integral. For the retarded

Green's function, we obtain

$$\begin{aligned}
&\left\langle\left\langle \hat{c}_{i,\sigma}; \hat{c}^{\dagger}_{j,\sigma} \right\rangle\right\rangle_E \\
&= -i \int_{-\infty}^{+\infty} \theta(t) \left\langle\left\langle \hat{c}_{i,\sigma}(t); \hat{c}^{\dagger}_{j,\sigma}(0) \right\rangle\right\rangle e^{iEt} dt \\
&= \lim_{\epsilon \to 0^+} -i \int_{0}^{+\infty} \left\langle\left\langle \hat{c}_{i,\sigma}(t); \hat{c}^{\dagger}_{j,\sigma}(0) \right\rangle\right\rangle e^{i(E+i\epsilon)t} dt
\end{aligned} \tag{B.6}$$

Similarly, we must let ϵ tend to zero from below the real axis for the advanced Green's function. By taking the Fourier transform of equation B.3, we get

$$E \left\langle\left\langle \hat{c}_{i,\sigma}; \hat{c}^{\dagger}_{j,\sigma} \right\rangle\right\rangle_E = \frac{1}{2\pi} \left\langle\left\langle [\hat{c}_{i,\sigma}, \hat{c}^{\dagger}_{j,\sigma}]_{\eta} \right\rangle\right\rangle_E + \left\langle\left\langle [\hat{c}_{i,\sigma}, \hat{H}]; \hat{c}^{\dagger}_{j,\sigma} \right\rangle\right\rangle_E \tag{B.7}$$

by using the following property of the Fourier transform

$$\frac{1}{2\pi} \int \frac{d}{dt} f(t) e^{i\omega t} dt = i\omega f(\omega) \tag{B.8}$$

First, note that from the Hamiltonian in equation 3.14, it can be shown that

$$\left[\hat{c}_{i,\sigma}, \hat{H}\right] = \sum_{j=1}^{L} t_{ij} \hat{c}_{i,\overline{\sigma}} + U \hat{n}_{i,\overline{\sigma}} \hat{c}_{i,\sigma} \tag{B.9}$$

which implies that

$$\begin{aligned}
&E \left\langle\left\langle \hat{c}_{i,\sigma}; \hat{c}^{\dagger}_{j,\sigma} \right\rangle\right\rangle_E \\
&= \frac{1}{2\pi} \delta_{ij} + \sum_{k} t_{ik} \left\langle\left\langle \hat{c}_{k,\sigma}; \hat{c}^{\dagger}_{j,\sigma} \right\rangle\right\rangle_E + U \left\langle\left\langle \hat{n}_{i,\overline{\sigma}} \hat{c}_{i,\sigma}; \hat{c}^{\dagger}_{j,\sigma} \right\rangle\right\rangle_E
\end{aligned} \tag{B.10}$$

For the last expression in the equation, write

$$\begin{aligned}
&E \left\langle\left\langle \hat{n}_{i,\overline{\sigma}} \hat{c}_{i,\sigma}; \hat{c}^{\dagger}_{j,\sigma} \right\rangle\right\rangle_E \\
&= \frac{1}{2\pi} \delta_{ij} \left\langle \hat{n}_{i,\overline{\sigma}} \right\rangle + \left\langle\left\langle \left[\hat{n}_{i,\overline{\sigma}} \hat{c}_{i,\sigma}, \hat{H}\right]; \hat{c}^{\dagger}_{j,\sigma} \right\rangle\right\rangle_E
\end{aligned} \tag{B.11}$$

By noting that

$$\left[\hat{n}_{i,\overline{\sigma}}, \hat{H}\right] = \sum_{j} t_{ij} (\hat{c}^{\dagger}_{i,\overline{\sigma}} \hat{c}_{j,\overline{\sigma}} - \hat{c}^{\dagger}_{j,\overline{\sigma}} \hat{c}_{i,\overline{\sigma}}), \tag{B.12}$$

we may write

$$\begin{aligned}
&\left[\hat{n}_{i,\overline{\sigma}} \hat{c}_{i,\sigma}, \hat{H}\right] \\
&= \left[\hat{n}_{i,\overline{\sigma}}, \hat{H}\right] \hat{c}_{i,\sigma} + \hat{n}_{i,\overline{\sigma}} \left[\hat{c}_{i,\overline{\sigma}}, \hat{H}\right] \\
&= \sum_{j} t_{ij} (\hat{c}^{\dagger}_{i,\overline{\sigma}} \hat{c}_{j,\overline{\sigma}} \hat{c}_{i,\sigma} - \hat{c}^{\dagger}_{j,\overline{\sigma}} \hat{c}_{i,\overline{\sigma}} \hat{c}_{i,\sigma}) \\
&+ \sum_{j} t_{ij} \hat{n}_{i,\overline{\sigma}} \hat{c}_{j,\sigma} + U \hat{n}_{i,\overline{\sigma}} \hat{c}_{i,\sigma}
\end{aligned} \tag{B.13}$$

This implies that equation B.11 can be written as

$$\begin{aligned} & E\left\langle\left\langle \hat{n}_{i,\overline{\sigma}}\hat{c}_{i,\sigma};\hat{c}^{\dagger}_{j,\sigma}\right\rangle\right\rangle_E \\ & = \frac{1}{2\pi}\delta_{ij}\left\langle \hat{n}_{i,\overline{\sigma}}\right\rangle + \sum_k t_{ik}\left\langle\left\langle \hat{c}^{\dagger}_{i,\overline{\sigma}}\hat{c}_{k,\overline{\sigma}}\hat{c}_{i,\sigma};\hat{c}^{\dagger}_{j,\sigma}\right\rangle\right\rangle_E \\ & - \sum_k t_{ik}\left\langle\left\langle \hat{c}^{\dagger}_{k,\overline{\sigma}}\hat{c}_{i,\overline{\sigma}}\hat{c}_{i,\sigma};\hat{c}^{\dagger}_{j,\sigma}\right\rangle\right\rangle_E \\ & + \sum_k t_{ik}\left\langle\left\langle \hat{n}^{\dagger}_{i,\overline{\sigma}}\hat{c}_{k,\sigma};\hat{c}^{\dagger}_{j,\sigma}\right\rangle\right\rangle_E + U\left\langle\left\langle \hat{n}_{i,\overline{\sigma}}\hat{c}_{i,\sigma};\hat{c}^{\dagger}_{j,\sigma}\right\rangle\right\rangle_E \end{aligned} \tag{B.14}$$

Clearly, continuing this procedure will lead to a hierarchy of higher order Green's functions unless the expression above is truncated at some point. To that end, we adopt the approximation scheme from [33], and write

$$\begin{aligned} \left\langle\left\langle \hat{n}_{i,\overline{\sigma}}\hat{c}_{k,\sigma};\hat{c}^{\dagger}_{j,\sigma}\right\rangle\right\rangle_E &\approx \left\langle \hat{n}_{i,\overline{\sigma}}\right\rangle\left\langle\left\langle \hat{c}_{k,\sigma};\hat{c}^{\dagger}_{j,\sigma}\right\rangle\right\rangle_E \\ \left\langle\left\langle \hat{c}^{\dagger}_{i,\overline{\sigma}}\hat{c}_{k,\overline{\sigma}}\hat{c}_{i,\sigma};\hat{c}^{\dagger}_{j,\sigma}\right\rangle\right\rangle_E &\approx \left\langle \hat{c}^{\dagger}_{i,\overline{\sigma}}\hat{c}_{k,\overline{\sigma}}\right\rangle\left\langle\left\langle \hat{c}_{i,\sigma};\hat{c}^{\dagger}_{j,\sigma}\right\rangle\right\rangle_E \\ \left\langle\left\langle \hat{c}^{\dagger}_{k,\overline{\sigma}}\hat{c}_{i,\overline{\sigma}}\hat{c}_{i,\sigma};\hat{c}^{\dagger}_{j,\sigma}\right\rangle\right\rangle_E &\approx \left\langle \hat{c}^{\dagger}_{k,\overline{\sigma}}\hat{c}_{i,\overline{\sigma}}\right\rangle\left\langle\left\langle \hat{c}_{i,\sigma};\hat{c}^{\dagger}_{j,\sigma}\right\rangle\right\rangle_E \end{aligned} \tag{B.15}$$

Now, upon inserting the above approximations into equation B.14, the following is obtained

$$\begin{aligned} & E\left\langle\left\langle \hat{n}_{i,\overline{\sigma}}\hat{c}_{i,\sigma};\hat{c}^{\dagger}_{j,\sigma}\right\rangle\right\rangle_E \\ & \approx \frac{1}{2\pi}\delta_{ij}n_{i,\overline{\sigma}} + \sum_k t_k\left\langle \hat{c}^{\dagger}_{i,\overline{\sigma}}\hat{c}_{k,\overline{\sigma}}\right\rangle\left\langle\left\langle \hat{c}_{i,\sigma};\hat{c}_{j,\sigma}\right\rangle\right\rangle_E \\ & - \sum_k t_k\left\langle \hat{c}^{\dagger}_{k,\overline{\sigma}}\hat{c}_{i,\overline{\sigma}}\right\rangle\left\langle\left\langle \hat{c}_{i,\sigma};\hat{c}_{j,\sigma}\right\rangle\right\rangle_E \\ & + \sum_k t_{ik}n_{i,\overline{\sigma}}\left\langle\left\langle \hat{c}_{k,\sigma};\hat{c}_{j,\sigma}\right\rangle\right\rangle_E \\ & + Un_{i,\overline{\sigma}}\left\langle\left\langle \hat{c}_{i,\sigma};\hat{c}^{\dagger}_{j,\sigma}\right\rangle\right\rangle_E \end{aligned} \tag{B.16}$$

Due to the fact that some terms cancel, we may write the expression as

$$E\Xi^{\sigma}_{ij}(E) = \frac{1}{2\pi}\delta_{ij}n_{i,\overline{\sigma}} + T_0\Xi^{\sigma}_{ij}(E) + U\Xi^{\sigma}_{ij}(E) + \sum_{k\neq i} t_{ik}n_{i,\overline{\sigma}}G^{\sigma}_{kj}(E) \tag{B.17}$$

where we defined

$$\Xi^{\sigma}_{ij}(E) = \left\langle\left\langle \hat{n}_{i,\overline{\sigma}}\hat{c}_{i,\sigma};\hat{c}^{\dagger}_{j,\sigma}\right\rangle\right\rangle \approx \left\langle \hat{n}_{i,\overline{\sigma}}\right\rangle\left\langle\left\langle \hat{c}_{k,\sigma};\hat{c}^{\dagger}_{j,\sigma}\right\rangle\right\rangle_E \tag{B.18}$$

which can be isolated for $\Xi^{\sigma}_{ij}(E)$ to give

$$\Xi^{\sigma}_{ij}(E) = \frac{1}{E - T_0 - U}\{\frac{1}{2\pi}\delta_{ij}n_{i,\overline{\sigma}} + \sum_{k\neq i} t_{ik}n_{i,\overline{\sigma}}G^{\sigma}_{kj}(E)\} \tag{B.19}$$

One may approximate $\langle n_{i,\overline{\sigma}} \rangle := n_{i,\overline{\sigma}} \approx n_{\overline{\sigma}}$, i.e., set the expected value of finding an electron of spin $\overline{\sigma}$ at any site to the same value. At this point, simply insert the expression above into the expression of the Green's function in equation B.10 and rearrange to obtain

$$EG^{\sigma}_{ij}(E) = T_0 G^{\sigma}_{ij}(E) + (1 + \frac{Un_{\overline{\sigma}}}{E - T_0 - U})(\frac{\delta_{ij}}{2\pi} + \sum_{k \neq i} t_{ik} G^{\sigma}_{kj}(E)) \tag{B.20}$$

As a preliminary remark to what follows, it is easy to see that for a non-interacting second quantized Hamiltonian, i.e.,

$$\hat{H} = \sum_{k} \epsilon(k) \hat{c}^{\dagger}_{k,\sigma} \hat{c}_{k,\sigma} \tag{B.21}$$

the retarded Green's function is given as

$$G^{+}_{\sigma}(k, E) = \frac{1}{E - \epsilon(k) + i\eta} \tag{B.22}$$

where $\eta > 0$ is some small number required to ensure the convergence of the Fourier transform from time-domain to energy domain. Equation B.22 shows by example that the roots of the denominator in the retarded Green's function is merely the single particle energy of the Hamiltonian for the given value of k. Now, this knowledge will be used in finding the single particle resonances of the strongly correlated system. Translational invariance of the system justifies the expression of G in the terms of its momentum space representation

$$G^{\sigma}_{ij}(E) = L^{-1} \sum_{q} G^{\sigma}(q, E) e^{iq(R_i - R_j)} \tag{B.23}$$

whereupon insertion into equation B.20 we get

$$EG^{\sigma}(q, E) = T_0 G^{\sigma}(q, E) + (1 + \frac{Un_{\overline{\sigma}}}{E - T_0 - U})(\frac{1}{2\pi} + (\epsilon_q - T_0) G^{\sigma}(q, E) \tag{B.24}$$

where we made use of

$$\begin{aligned} \sum_{k \neq i} t_{ik} &= \sum_{k} t_{ik} G^{\sigma}_{kj}(E) - T_0 G^{\sigma}_{ij}(E) \\ &= L^{-1} \sum_{q} (\epsilon(q) - T_0) G^{\sigma}(q, E) e^{iq(R_i - R_j)} \end{aligned} \tag{B.25}$$

In going from B.20 to B.24, we also used the property

$$L^{-1} \sum_{q} e^{iq(R_i - R_j)} = \delta_{ij} \tag{B.26}$$

Isolating for $G^{\sigma}(q, E)$ in equation B.24, it is seen that

$$G^{\sigma}(q, E) = \frac{1}{2\pi} \frac{E - T_0 - U(1 - n_{\overline{\sigma}})}{(E - \epsilon(q))(E - T_0 - U) + n_{\overline{\sigma}} U(T_0 - \epsilon(q))} \tag{B.27}$$

whence it is seen that the energies are the roots of

$$(E - \epsilon(q))(E - T_0 - U) + n_{\overline{\sigma}} U(T_0 - \epsilon(q)) = 0 \tag{B.28}$$

which is what we wanted to show.

Bibliography

[1] R. E. F. Silva, I. V. Blinov, A. N. Rubtsov, O. Smirnova, and M. Ivanov, "High-harmonic spectroscopy of ultrafast many-body dynamics in strongly correlated systems," *Nature Photonics*, 2018. [Online]. Available: https://doi.org/10.1038/s41566-018-0129-0 (document), 1.3, 1.3, 1.3, 1.6, 1.3, 3, 4.1.2, 6, 6.1, 6.2, 6.2, 6.2, 6.4, 6.4, 6.5

[2] N. Bohr, "I. on the constitution of atoms and molecules," *The London, Edinburgh, and Dublin Philosophical Magazine and Journal of Science*, vol. 26, no. 151, pp. 1–25, 07 1913. [Online]. Available: https://doi.org/10.1080/14786441308634955 1.1

[3] F. Krausz and M. Ivanov, "Attosecond physics," *Reviews of Modern Physics*, vol. 81, no. 1, pp. 163–234, 02 2009. [Online]. Available: https://link.aps.org/doi/10.1103/RevModPhys.81.163 1.1

[4] P. H. Bucksbaum, "Ultrafast control," *Nature*, vol. 421, pp. 593 EP –, 02 2003. [Online]. Available: http://dx.doi.org/10.1038/421593a 1.1

[5] S. Koch, "High harmonics generated in semiconductor nanostructures by the coupled dynamics of optical inter- and intraband excitations," *Physical Review B*, 2008. 1.1, 1.3, 1.3, 3.2, 4.1, 4.1.1, 4.1.1, 6.5

[6] O. E. Alon, V. Averbukh, and N. Moiseyev, "Selection rules for the high harmonic generation spectra," *Physical Review Letters*, vol. 80, no. 17, pp. 3743–3746, 04 1998. [Online]. Available: https://link.aps.org/doi/10.1103/PhysRevLett.80.3743 1.1

[7] M. Lewenstein, P. Balcou, M. Y. Ivanov, A. L'huillier, and P. B. Corkum, "Theory of high-harmonic generation by low-frequency laser fields," *Physical Review A*, vol. 49, no. 3, p. 2117, 1994. 1.2, 1.2, 1.3, 4.2

[8] R. E. Ferreira Da Silva, "Study of diatomic molecules under short intense laser pulses," Ph.D. dissertation, 2016. 1, 1, 1.3, 4.1.2, 6, 6

[9] F. Calegari, G. Sansone, S. Stagira, C. Vozzi, and M. Nisoli, "Advances in attosecond science," *Journal of Physics B: Atomic, Molecular and Optical Physics*, vol. 49, no. 6, pp. 062 001 1.2

[10] T. Ikemachi, Y. Shinohara, T. Sato, J. Yumoto, M. Kuwata-Gonokami, and K. L. Ishikawa, "Trajectory analysis of high-order-harmonic generation from periodic crystals," *Physical Review A*, vol. 95, no. 4, pp. 043 416–, 04 2017. [Online]. Available: https://link.aps.org/doi/10.1103/PhysRevA.95.043416 1.2, 4.1

[11] G. Vampa, C. R. McDonald, G. Orlando, D. D. Klug, P. B. Corkum, and T. Brabec, "Theoretical analysis of high-harmonic generation in solids," *Physical Review Letters*, vol. 113, no. 7, pp. 073 901–, 08 2014. [Online]. Available: https://link.aps.org/doi/10.1103/PhysRevLett.113.073901 1.3, 3, 4.1, 4.2

[12] H. Haug and S. W. . . Koch, *Quantum Theory of the Optical and Electronic Properties of Semiconductors: Fifth Edition*. World Scientific Publishing Company, 2009. 1.3, 2, 2.4, 2.4, 2.4, 3.1, 7

[13] M. Glück, A. R. Kolovsky, and H. J. Korsch, "Wannier–stark resonances in optical and semiconductor superlattices," *Physics Reports*, vol. 366, no. 3, pp. 103–182, 2002. [Online]. Available: http://www.sciencedirect.com/science/article/pii/S0370157302001424 1.3, 4.1.2

[14] O. Schubert, M. Hohenleutner, F. Langer, B. Urbanek, C. Lange, U. Huttner, D. Golde, T. Meier, M. Kira, S. W. Koch, and R. Huber, "Sub-cycle control of terahertz high-harmonic generation by dynamical bloch oscillations," *Nature Photonics*, vol. 8, pp. 119 EP –, 01 2014. [Online]. Available: http://dx.doi.org/10.1038/nphoton.2013.349 1.3, 4.1.2

[15] P. Földi, M. G. Benedict, and V. S. Yakovlev, "The effect of dynamical bloch oscillations on optical-field-induced current in a wide-gap dielectric," *New Journal of Physics*, vol. 15, no. 6, p. 063019, 2013. [Online]. Available: http://stacks.iop.org/1367-2630/15/i=6/a=063019 1.3

[16] G. Vampa, C. McDonald, G. Orlando, P. Corkum, and T. Brabec, "Semiclassical analysis of high harmonic generation in bulk crystals," *Physical Review B*, vol. 91, no. 6, p. 064302, 2015. 1.3, 4.2

[17] T. Brabec and F. Krausz, "Intense few-cycle laser fields: Frontiers of nonlinear optics," *Reviews of Modern Physics*, vol. 72, no. 2, pp. 545–591, 04 2000. [Online]. Available: https://link.aps.org/doi/10.1103/RevModPhys.72.545 1.3

[18] N. Tancogne-Dejean, O. D. Mücke, F. X. Kärtner, and A. Rubio, "Impact of the electronic band structure in high-harmonic generation spectra of solids," *Physical Review Letters*, vol. 118, no. 8, pp. 087 403–, 02 2017. [Online]. Available: https://link.aps.org/doi/10.1103/PhysRevLett.118.087403 1.3

[19] M. Liu, H. Y. Hwang, H. Tao, A. C. Strikwerda, K. Fan, G. R. Keiser, A. J. Sternbach, K. G. West, S. Kittiwatanakul, J. Lu, S. A. Wolf, F. G. Omenetto, X. Zhang, K. A. Nelson, and R. D. Averitt, "Terahertz-field-induced insulator-to-metal transition in vanadium dioxide metamaterial," *Nature*, vol. 487, pp. 345 EP –, 07 2012. [Online]. Available: http://dx.doi.org/10.1038/nature11231 1.3

[20] B. Mayer, C. Schmidt, A. Grupp, J. Bühler, J. Oelmann, R. E. Marvel, R. F. Haglund, T. Oka, D. Brida, A. Leitenstorfer, and A. Pashkin, "Tunneling breakdown of a strongly correlated insulating state in $\mathrm{v}{\mathrm{o}}_{2}$ induced by intense multiterahertz excitation," *Physical Review B*, vol. 91, no. 23, pp. 235 113–, 06 2015. [Online]. Available: https://link.aps.org/doi/10.1103/PhysRevB.91.235113 1.3

[21] T. Oka, "Nonlinear doublon production in a mott insulator: Landau-dykhne method applied to an integrable model," *Physical Review B*, vol. 86, no. 7, pp. 075 148–, 08 2012. [Online]. Available: https://link.aps.org/doi/10.1103/PhysRevB.86.075148 1.3, 3, 6

[22] G. Vampa, T. J. Hammond, N. Thiré, B. E. Schmidt, F. Légaré, C. R. McDonald, T. Brabec, D. D. Klug, and P. B. Corkum, "All-optical reconstruction of crystal band structure," *Physical Review Letters*, vol. 115, no. 19, pp. 193 603–, 11 2015. [Online]. Available: https://link.aps.org/doi/10.1103/PhysRevLett.115.193603 1.3, 6.5

[23] F. Langer, M. Hohenleutner, C. P. Schmid, C. Pöllmann, P. Nagler, T. Korn, C. Schüller, M. Sherwin, U. Huttner, J. Steiner *et al.*, "Lightwave-driven quasiparticle collisions on a subcycle timescale," *Nature*, vol. 533, no. 7602, p. 225, 2016. 1.3, 4.1.2

[24] F. Mandl, *The Manchester physics series*. Chichester: Wiley, 1992. 2.1, 2.3, 3.2

[25] D. J. Griffiths, "Introduction to electrodynamics," San Francisco, Calif, 2008. 2.2, 4.1.2, 6

[26] R. A. Adams and C. Essex, *Calculus : a complete course*. Toronto: Pearson, 2013. 2.2

[27] E. Merzbacher, *Quantum mechanics*, 3rd ed. New York: Wiley, 1998. 2.3

[28] S. J. Malham, "An introduction to lagrangian and hamiltonian mechanics." 2.3

[29] F. H. L. Essler, H. Frahm, F. Gohmann, A. Klumper, and V. E. Korepin, *The one-dimensional Hubbard model*, 2003. 2.3, 3.1, 3.2, 3.4, 4.1

[30] C. Kittel, P. McEuen, and P. McEuen, *Introduction to solid state physics*. Wiley New York, 1996, vol. 8. 2.4, 4.1, 4.1.1

[31] A. Altland and B. D. . X. Simons, *Condensed matter field theory*. Cambridge University Press, 2010. 2.5, 6.3

[32] S. Ghimire, A. D. DiChiara, E. Sistrunk, P. Agostini, L. F. DiMauro, and D. A. Reis, "Observation of high-order harmonic generation in a bulk crystal," *Nature Physics*, vol. 7, pp. 138 EP –, 12 2010. [Online]. Available: http://dx.doi.org/10.1038/nphys1847 3, 4.1

[33] J. Hubbard, "Electron correlations in narrow energy bands," *Proc. R. Soc. Lond. A*, vol. 276, no. 1365, pp. 238–257 3, 3.1, 3.2, 3.2, B, B

[34] F. Patrik, *Lecture notes on electron correlation and magnetism*. World scientific, 1999, vol. 5. 3, 3.2, 3.2, 6.2, 6.3, 6.6

[35] E. Dagotto, F. Ortolani, and D. Scalapino, "Single-particle spectral weight of a two-dimensional hubbard model," *Physical Review B*, vol. 46, no. 5, p. 3183, 1992. 3

[36] T. Giamarchi, "Mott transition in one dimension," *Physica B: Condensed Matter*, vol. 230, pp. 975–980 3

[37] P. L. Taylor, P. L. Taylor, and O. . . Heinonen, *A quantum approach to condensed matter physics*. Cambridge university press, 2002. 3.1

[38] D. Golde, T. Meier, and S. W. Koch, "Microscopic analysis of high-harmonic generation in semiconductor nanostructures," *Physica Status Solidi C*, 2008. 4.1

[39] M. Wu, S. Ghimire, D. A. Reis, K. J. Schafer, and M. B. Gaarde, "High-harmonic generation from bloch electrons in solids," *Physical Review A*, vol. 91, no. 4, pp. 043 839–, 04 2015. [Online]. Available: https://link.aps.org/doi/10.1103/PhysRevA.91.043839 4.1

[40] A. F. Kemper, B. Moritz, J. K. Freericks, and T. P. Devereaux, "Theoretical description of high-order harmonic generation in solids," *New Journal of Physics*, February 2013. 4.1, 4.1.1, 6.3

[41] R. P. Feynman, R. B. Leighton, and M. Sands, "The feynman lectures on physics. 3: Quantum mechanics: Lectures on physics," 1965. 4.1.2

[42] M. Abramowitz and I. A. Stegun, *Handbook of mathematical functions: with formulas, graphs, and mathematical tables*. Courier Corporation, 1964, vol. 55 4.1.2

[43] H. Fehske, R. Schneider, and A. Weiße, "Lecture notes in physics," vol. 739, 2008. 5.1, 5.1.1, 5.2

[44] H. Lin, J. Gubernatis, H. Gould, and J. Tobochnik, "Exact diagonalization methods for quantum systems," *Computers in physics*, vol. 7, no. 4, pp. 400–407 5.1, 5.2

[45] A. Dolfen, "Massively parallel exact diagonalization of strongly correlated systems," 2006. 5.1, 5.2

[46] A. I. Kuleff, J. Breidbach, and L. S. Cederbaum, "Multielectron wave-packet propagation: General theory and application," *The Journal of Chemical Physics*, vol. 123, no. 4, p. 044111, 2018/04/22 2005. [Online]. Available: https://doi.org/10.1063/1.1961341 5.3

[47] M. Hohenleutner, F. Langer, O. Schubert, M. Knorr, U. Huttner, S. W. Koch, M. Kira, and R. Huber, "Real-time observation of interfering crystal electrons in high-harmonic generation," *Nature*, vol. 523, pp. 572 EP –, 07 2015. [Online]. Available: http://dx.doi.org/10.1038/nature14652 6.2

[48] B. J. Powell, "An introduction to effective low-energy hamiltonians in condensed matter physics and chemistry," *arXiv preprint arXiv:0906.1640*, 2009. 6.3

[49] S. Wall, D. Brida, S. R. Clark, H. P. Ehrke, D. Jaksch, A. Ardavan, S. Bonora, H. Uemura, Y. Takahashi, T. Hasegawa, H. Okamoto, G. Cerullo, and A. Cavalleri, "Quantum interference between charge excitation paths in a solid-state mott insulator," *Nature Physics*, vol. 7, pp. 114 EP –, 12 2010. [Online]. Available: http://dx.doi.org/10.1038/nphys1831 6.6, 6.6, 7